

**A Study of Solidification Structure Evolution  
during Investment Casting of Ni-based  
Superalloy for Aero-Engine Turbine Blades**

*A thesis submitted for the degree of  
Doctor of Philosophy  
in the University of Leicester*

*by*

**Huijuan Dai**

Department of Engineering  
University of Leicester

*December 2008*

# **A Study of Solidification Structure Evolution during Investment Casting of Ni-based Superalloy for Aero-Engine Turbine Blades**

Huijuan Dai

## **Abstract**

The need to achieve increased efficiency and performance in aerospace gas turbines requires advanced single crystal Ni-based superalloys to exhibit increased temperature capabilities. High temperature creep resistance of the turbine blades is one of the major limitations to meet increased performance goals of gas turbines. The ultimate creep resistance of the Ni-based superalloys is dependent on solidification structures formed during casting.

In this study, multi-scale modelling method was used to study the solidification structure evolution occurring at various scales during investment casting. Modelling of solidification on the macroscopic scale of the process was implemented using a macroscopic Finite Element casting model, ProCAST, to predict thermal and flow profiles. The predicted thermal and flow data were then used as input in a meso-scale model Cellular Automaton Finite Element (CAFE) to predict grain structure and grain orientations during solidification. At the micro-level, detailed dendritic morphology and solutal interaction were investigated using a  $\mu$ MatIC model. Using the multi-scale approach, grain selection in spiral grain selector, formation of new grains ahead of solidification interface and the effect of dendrite packing patterns on primary dendrite spacing were investigated.

The effect of spiral shape on grain selection in single crystal grain selector has been systematically studied. It was found that the efficiency of the spiral selector significantly depends on its geometry and dimensions. The spiral becomes more efficient with a smaller wax wire diameter, larger spiral diameter and smaller take-off angle.

Formation of new grains ahead of solid/liquid growth front was simulated. Stray grain formation in the platform region of turbine blades was investigated, indicating that the alloy with greater susceptibility to the formation of stray grains has lower critical nucleation undercooling. The columnar-to-equiaxed transition (CET) during solidification was predicted and the effect of material properties on the CET was analyzed. The analysis results revealed that the CET can be promoted by: (1) decreasing the critical nucleation undercooling; (2) increasing the nuclei density of the melt; and (3) extending the solidification range.

Dendrites with different packing patterns were used to simulate dendrite spacing adjustment during solidification. It was found that the branching of secondary and tertiary arms in the hexahedral packing is easier than that in the cuboidal packing, leading to a smaller average spacing.

**This thesis is dedicated to my parents**

**Jinming Dai and Jianying Gao**

## **Acknowledgements**

I would like to express my sincere gratitude to my supervisor Dr. Hongbiao Dong. Apart from his high standard supervision, he has given me painstaking guidance on my PhD study. He has also provided me with precious opportunities to collaborate with other institutions and to present my work in many conferences, which are very beneficial for me, not only for my PhD research, but also for my future career. His help and motivation has certainly provided a huge contribution towards the completion of a successful project.

I would like to give my appreciation to my co-supervisor Prof. Helen V. Atkinson for her invaluable advices on my research and help on my writing. I also want to thank my co-supervisor Prof. Peter D. Lee from Imperial College London to give me constructive suggestions and kind help especially offering me the opportunity to use the  $\mu$ MatIC code during my PhD study.

Special appreciation would like to be given to my industry supervisor Dr. Neil D' Souza from Rolls-Royce Plc for giving excellent guidance and offering invaluable help. Many thanks to Dr. Paul D. Brown from Rolls-Royce Plc for giving me precious advices on process modelling and Dr. Paul Withey from Rolls-Royce Plc for his meaningful support.

I would like to thank Prof. Roger Reed, director of the Partnership for Research in the Simulation of Manufacturing and Materials (PRISM2), University of Birmingham, where I worked as a visiting student during my PhD. His invaluable advices and support are meaningful for my PhD study. Also thank Dr. Jean-Christophe Gebelin for providing me a lot of help on the software learning and patiently giving me support when I had problems. I would like to express my appreciation to Prof. Nick Green to support me to do the experimental work in University of Birmingham, and his remarkable insights and suggestions are beneficial for my study. Also thank Dr. Yizhou Zhou and Matthew Newell for all their time and efforts on the help of the experimental

## *Acknowledgements*

---

work. And thank Dr. Nils Warnken for his precious discussions. Thanks to their help, I have benefited greatly from the collaboration with University of Birmingham.

I would like to express my gratitude to Drs. Robert C. Atwood, Dylan Ness and Junsheng Wang from Imperial College London for their help on the program training of  $\mu$ MatIC. Special appreciation would like to be expressed to Lang Yuan from Imperial College London to give me a lot of help on programming and priceless suggestions on my research.

I also thank those in the Mechanics of Materials (MOM) Group in University of Leicester who have given me all kinds of help, especially Guanyu Yi, Kenny Jolly, Ram Krishna, Guixiang Qin, Fan Li and Xiaoxiao Han.

All the technicians involving in this project are appreciated for their continued assistance.

Finally, I would like to express my deepest appreciation and warmest regards to my dear parents for their endless love. They have offered me continuous financial support and given me encouragement in all situations.

## **List of Publications**

### **Innovation Patent:**

**Dendritic Grain Pattern Selector for SX Casting** (N. D'Souza, H.B. Dong, **H.J. Dai**, P. Withey) Supported by Rolls-Royce Plc. (UK Patent Application Number: DY4113; US and European Patents Pending)

### **Publications:**

1. **H.J. Dai**, J-C. Gebelin, N.D' Souza, P.D. Brown, H.B. Dong, "*The Effect of Spiral Shape on Grain Selection during Casting of Single Crystal Turbine Blades*", International Journal of Cast Metals Research, 2009 (In Press)
2. **H.J. Dai**, H. B. Dong, H.V. Atkinson, P.D. Lee, "*Simulation of the Columnar-to-Equiaxed Transition in Alloy Solidification -- the Effect of Nucleation Undercooling, Density of Nuclei in Bulk Liquid and Alloy Solidification Range on the Transition*", Solid State Phenomena, Vol. 139 (2008), pp 129-134
3. **H.J. Dai**, J-C. Gebelin, M. Newell, R.C. Reed, N. D' Souza, P.D. Brown, H.B. Dong, "*Grain Selection during Solidification in Spiral Grain Selector*", Proceedings of Superalloys 2008, pp 367-374, Pennsylvania, USA, 14-18 September, 2008 (Paper published with oral presentation)
4. N. D' Souza,, M. Lekstrom, **H.J. Dai**, B.A. Shollock , H.B. Dong, "*Quantitative Characterisation of Last Stage Solidification in a Ni - Base Superalloy using an Enthalpy - Based Method*", Material Science and Technology, Vol. 23 (2007), pp 1085-1092
5. **H.J. Dai**, M. Sarwar, H.B. Dong, H.V. Atkinson, N. D' Souza, P.D. Lee, "*Measurement of Nucleation Undercooling during Casting of Ni-Based Superalloy IN792*", Proceedings of the 2007 International Symposium on Liquid

Metal Processing and Casting, pp 177-180, Nancy, France, 2-5 September, 2007  
(Paper published with oral presentation)

6. **H.J. Dai**, H.B. Dong, H.V. Atkinson, N. D' Souza, L. Thuinet and P.D. Lee, *"The influence of dendrite packing patterns on primary spacing adjustment during directional solidification"*, Proceedings of the 5th Decennial International Conference on Solidification Processing, pp 1-5, Solidification Processing 2007, Sheffield, UK, 23-25 July 2007 (Paper published with oral presentation)
7. **H.J. Dai**, H.B. Dong, *"Multiscale Modelling of Solidification Structure Evolution and Grain Selection in Aero-Engine Turbine Blades"*, 4<sup>th</sup> Chinese International Conference on Materials, Chongqing China, 12-16 Oct, 2007 (Oral presentation)

# Table of Contents

Abstract .....	I
Acknowledgements.....	III
List of Publications .....	V
Table of Contents.....	VII
List of Figures.....	IX
List of Tables .....	XVI
Chapter 1 Introduction.....	1
Chapter 2 Literature Review .....	3
2.1 Chemistry of Blade Alloys .....	3
2.1.1 Ni-based Superalloy for Turbine Blades .....	3
2.1.2 Chemistry Development of Blade Alloys.....	5
2.2 Processing .....	9
2.3 Microstructure Evolution during Casting .....	14
2.3.1 Dendritic Structure Evolution .....	14
2.3.2 Primary Spacing in Dendrites .....	17
2.3.3 Competitive Growth Mechanism.....	19
2.4 Theory of Solidification.....	21
2.4.1 Grain Nucleation.....	21
2.4.2 Growth Kinetics.....	24
2.5 Modelling of Solidification Structures .....	29
2.5.1 Dendrite Growth Models .....	30
2.5.2 Phase Field Models.....	32
2.5.3 Cellular Automaton Models.....	33
Chapter 3 Model Description .....	35
3.1 Macro-scale Model ProCAST .....	36
3.2 Meso-scale Model CAFE.....	39
3.2.1 Cellular Automaton.....	40
3.2.2 Coupling the FE and CA Models.....	43
3.3 Micro-scale Model $\mu$ MatIC .....	44
3.3.1 Model Assumptions .....	46
3.3.2 Nucleation.....	48
3.3.3 Growth Mechanism.....	49
3.4 Summary.....	51
Chapter 4 Grain Selection during Investment Casting of Single Crystal Turbine Blades .....	53
4.1 Simulation of Grain Selection in SX Grain Selector .....	53
4.1.1 Thermal Predictions in the Casting Process .....	54
4.1.2 Quantitative Description of Spiral Size and Geometry .....	59
4.1.3 The Effect of Spiral Geometry on Grain Selection.....	60
4.2 Sensitivity Study of Grain Selection in Full Size SX Grain Selector Combined with Designed Spiral.....	75
4.2.1 Sensitivity Study on Random Nucleation Generation .....	77

*Table of Contents*

---

4.2.2	The Influence of Spiral Designs on the Efficiency of Grain Selection for Full Size SX Grain Selector .....	79
4.3	Experimental Validation of Grain Selection in Spiral Selector .....	82
4.3.1	Details of Investment Casting Procedure Employed .....	83
4.3.2	Microstructure Analyses using Optical Microscopy .....	86
4.3.3	EBSD Analyses on Grain Selection in the Spiral Selector .....	88
4.4	Mechanism of Grain Selection in Spiral Selector .....	91
4.5	Summary .....	94
Chapter 5	Modelling the Formation of New Grains ahead of the Advancing Solidification Front .....	96
5.1	Stray Grain Formation in Single-crystal Turbine Blades .....	96
5.1.1	Simulation Parameters .....	97
5.1.2	Dendritic Structure Evolution .....	99
5.1.3	Solutal Interaction within the Advancing Dendritic Network .....	100
5.1.4	Undercooling ahead of the Advancing Dendritic Network .....	102
5.1.5	Formation of New Grains ahead of the Advancing Dendritic Network ..	105
5.1.6	Formation of Stray Grains in the Platform Region of Turbine Blades ....	108
5.2	Effects of Material Properties on Columnar-to-Equiaxed Transition.....	112
5.2.1	Simulation Parameters .....	114
5.2.2	Effect of Critical Nucleation Undercooling .....	114
5.2.3	Effect of Nuclei Density in Bulk Liquid.....	116
5.2.4	Effect of Alloy Solidification Range .....	117
Chapter 6	The Influence of Dendrite Packing Patterns on Primary Spacing Adjustment during Solidification.....	119
6.1	3D $\mu$ MatIC Model.....	119
6.2	Comparison between 2D and 3D Simulations .....	120
6.2.1	Simulated Structure Evolution using 2D and 3D $\mu$ MatIC Models .....	120
6.2.2	Solutal Interactions within the Advancing Dendritic Network in 2D and 3D Simulations .....	123
6.3	Effect of Packing Patterns on Primary Spacing Adjustment during Solidification.....	129
6.3.1	Branching.....	130
6.3.2	Effect of Packing Patterns on Primary Spacing.....	131
6.4	Summary .....	135
Chapter 7	Conclusions and Future Work .....	137
7.1	Conclusions.....	137
7.1.1	Grain Selection during Investment Casting of Single Crystal Turbine Blades .....	137
7.1.2	The Formation of New Grains ahead of the Advancing Solidification Front .....	138
7.1.3	The Influence of Dendrite Packing Patterns on Primary Spacing Adjustment during Solidification.....	138
7.2	Future Work .....	139
Appendix A:	Measurement of Nucleation Undercooling during Solidification of the Ni-based Superalloy, IN792 .....	141
References	.....	147

## List of Figures

<i>Figure 1.1 Rolls-Royce Trent 800 aero engine (a) and its turbine blade (b) (Image courtesy Rolls-Royce Plc.)</i> .....	1
<i>Figure 2.1 Al-Ni binary phase diagram (Calculated using Thermo-Calc)</i> .....	4
<i>Figure 2.2 Scanning electron micrograph of the <math>\gamma/\gamma'</math> microstructure of single-crystal Ni-based superalloy (Caron and Khan, 1999)</i> .....	4
<i>Figure 2.3 Crystal structures of <math>\gamma</math> (a) and <math>\gamma'</math> (b) phases in Ni-based superalloys (Bhadeshia, Cambridge)</i> .....	5
<i>Figure 2.4 Typical temperature advantages over CC superalloys obtained with DS and SX superalloys estimated from stress rupture tests performed at 982°C and 248 MPa (Erickson, 1995)</i> .....	7
<i>Figure 2.5 The microstructure development of casting turbine blades from equiaxed crystal structure to single crystal (Wong, 2003)</i> .....	9
<i>Figure 2.6 Illustration of the various stages of investment casting process</i> .....	11
<i>Figure 2.7 Schematic illustration of investment casting for single crystal turbine blades</i> .....	12
<i>Figure 2.8 Various designs of grain selector for single crystal turbine blades (Goulette, 1984)</i> .....	13
<i>Figure 2.9 A schematic drawing of the grain selector design used in a 2D analytical model (Esaka et al. 2005)</i> .....	14
<i>Figure 2.10 Columnar-to-equiaxed transition (CET) in casting process (Campbell, 2003)</i> .....	15
<i>Figure 2.11 Scanning electron image showing the 3D dendritic morphology of single crystal Ni-based superalloy for both (a) transverse and (b) longitudinal directions (Kearsey et al. 2004)</i> .....	16
<i>Figure 2.12 Length scales used in dendrite study</i> .....	17
<i>Figure 2.13 Illustration of micro-segregation in the transverse section of Ni-based single crystal superalloy (after Kearsey et al. 2004)</i> .....	18

## List of Figures

---

<i>Figure 2.14 A schematic diagram showing the primary spacing change mechanisms for dendrites: a) overgrowth; b) steady state; and c) branching (Hunt, 1979) .....</i>	<i>19</i>
<i>Figure 2.15 Schematic representation of dendrite growth illustrating the mechanism of competitive growth during directional solidification (Rappaz and Gandin, 1993).....</i>	<i>20</i>
<i>Figure 2.16 Gibbs free energy change associated with homogenous nucleation having a spherical shape (Kurz and Fisher, 1984) .....</i>	<i>23</i>
<i>Figure 2.17 Schematics of heterogeneous nucleation; the wetting angle is defined as the angle between the nucleus (crystal) and the foreign solid (Kurz and Fisher, 1984).....</i>	<i>24</i>
<i>Figure 2.18 Low concentration end of a phase diagram for a typical binary alloy (<math>k &lt; 1</math>). The solidus and liquidus are assumed to be approximately straight lines of gradients <math>m_S</math> and <math>m_L</math>, respectively (Chilton, 2002) .....</i>	<i>25</i>
<i>Figure 2.19 Solute redistribution during equilibrium solidification: (a) at the start of solidification, (b) at temperature <math>T^*</math>, (c) when solidification is complete, (d) the corresponding phase diagram (Flemings, 1974).....</i>	<i>27</i>
<i>Figure 2.20 Solute redistribution under the Scheil condition during solidification (Stanford et al. 2004).....</i>	<i>27</i>
<i>Figure 2.21 (a) Solute distribution at the S/L interface; (b) constitutional undercooling in front of the S/L interface; and (c) effects of different undercoolings during solidification in a linearized binary phase diagram (Kurz and Fisher, 1984).....</i>	<i>29</i>
<i>Figure 3.1 Schematic illustration of multi-scale modelling .....</i>	<i>35</i>
<i>Figure 3.2 Structure of macro-model ProCAST (ESI, 2006) .....</i>	<i>39</i>
<i>Figure 3.3 (a) Schematics for a small solidifying volume element of uniform temperature within which nucleation and growth can occur from the mould and in the bulk; (b) corresponding cell schematics for the cellular automaton used to predict microstructure formation in the small solidifying specimen shown in (a) (Rappaz and Gandin, 1993).....</i>	<i>41</i>
<i>Figure 3.4 Heterogeneous nucleation site distributions for nuclei formed at the mould wall and in the bulk of the melt (Rappaz and Gandin, 1993).....</i>	<i>42</i>
<i>Figure 3.5 Schematics of the solidification domain coupled with a FE mesh and a CA grid (Gandin et al. 1999).....</i>	<i>43</i>
<i>Figure 3.6 3D views of analytical (a) and numerical (b) predictions of a grain envelope without considering solute diffusion in meso-scale, and (c) simulated dendritic structure coupled with solute diffusion using <math>\mu</math>MatIC model in micro-scale (Wang et al. 2003) .</i>	<i>45</i>

## List of Figures

---

Figure 3.7 A schematic of 2D dendritic microstructure in solute diffusion model (Dong and Lee, 2005) .....	46
Figure 3.8 Schematic illustration of the temperature field (Yang, 2005).....	47
Figure 3.9 A schematic diagram showing solute partitioning and solute distribution during solidification.....	49
Figure 3.10 Schematic diagram of modified 2D decentred square CA growth algorithm (Wang et al. 2003) .....	51
Figure 4.1 Grain selector for the Trent 800 high-pressure turbine blade, showing the details of starter block and spiral grain selector (Reed, 2006).....	54
Figure 4.2 (a) Instrumented mould of VeriCAST blade process modelling test piece on furnace and (b) VeriCAST blade casting after removal of the investment shell (Courtesy of Rolls-Royce plc.) (After Jennings, 1996).....	55
Figure 4.3 Predicted three-dimensioned thermal fields during casting of turbine blade; (a) investment furnace, (b) enlarged view of the casting blade, (c) enlarged view of the grain selector .....	56
Figure 4.4 (a) Predicted grain structure in the grain selector; cross section views and corresponding $\langle 001 \rangle$ pole figures along vertical thermal gradient at the height from the chill of: (b) 2mm; (c) 5mm; (d) 10mm; (e) 29mm.....	57
Figure 4.5 (a) Average deviations of grain orientations at different heights from the chill; (b) grain selector illustrating the corresponding heights; (c) schematic definition of grain deviation.....	58
Figure 4.6 (a) Spiral geometry defined in this study and (b) 2D schematic showing the definition of spiral take-off angle.....	59
Figure 4.7 (a) Predicted grain structure in the spiral selector, the grain structures evolution (b1) – (f1), corresponding $\langle 001 \rangle$ pole figures along the direction of heat flux (b2) – (f2) and the grain deviation distributions (b3) – (f3) for the cross sections at the height of: (b) 0.1mm; (c) 1.1mm; (d) 6.25; (e) 11.5mm; (f) 16.75mm from the chill.....	62
Figure 4.8 Schematic diagram showing the required height for a SX structure to occur in the spiral.....	64
Figure 4.9 Grain structure in the spiral selector with wax wire diameter ( $d_w$ ) of : (a) 2mm; (b) 3mm; (c) 4mm; (d) 5mm; (e) 6mm; (f) 7mm; (g) 8mm .....	66
Figure 4.10 Effect of wax wire diameter ( $d_w$ ) on the required height for SX selection in the spiral grain selector (*5 trials, 4 of them failed in selecting one grain).....	66

*List of Figures*

---

*Figure 4.11 Effect of wax wire diameter ( $d_w$ ) on the required volume for SX selection in spiral grain selector..... 67*

*Figure 4.12 Effect of wax wire diameter ( $d_w$ ) on the final SX orientation in spiral grain selector..... 68*

*Figure 4.13 Grain structure in the spiral selector with the spiral diameter ( $d_s$ ) of: (a) 13mm; (b) 15mm; (c) 17mm ..... 69*

*Figure 4.14 Effect of spiral diameter ( $d_s$ ) on the required height for SX selection in spiral grain selector..... 70*

*Figure 4.15 Effect of spiral diameter ( $d_s$ ) on the required volume for SX selection in spiral grain selector..... 70*

*Figure 4.16 Effect of spiral diameter ( $d_s$ ) on the final SX orientation in spiral grain selector..... 71*

*Figure 4.17 Grain structure in the spiral selector with spiral take-off angle ( $\theta$ ) of: (a) 20°; (c) 50°; (d) 70° ..... 72*

*Figure 4.18 Effect of spiral take-off angle ( $\theta$ ) on the required height for SX selection in spiral grain selector..... 73*

*Figure 4.19 Effect of spiral take-off angle ( $\theta$ ) on the required volume for SX selection in spiral grain selector..... 74*

*Figure 4.20 Effect of spiral take-off angle ( $\theta$ ) on final SX orientation in spiral grain selector..... 75*

*Figure 4.21 (a) Longitudinal section view of investment casting furnace for Case 1; (b) detailed view of grain selector..... 77*

*Figure 4.22 Distribution of required heights for SX selection in grain selector (Case16) when population is: (a) 10; (b) 20; (c) 50 and (d) 100..... 78*

*Figure 4.23 Grain structure in designed grain selector with spiral take-off angle ( $\theta$ ) of: (a) 20°; (c) 35°; (d) 50° ..... 80*

*Figure 4.24 The influence of spiral take-off angle ( $\theta$ ) on the required height for SX selection in full size grain selectors ..... 81*

*Figure 4.25 Final SX grain orientations for full size grain selectors with spiral take-off angle ( $\theta$ ) of: (a) 28°; (b) 29°; (c) 35°; (d) 40°; (e) 50° ..... 82*

## List of Figures

---

Figure 4.26 Wax moulds with different spiral take-off angles ( $\theta$ ) of: (a) $28^\circ$ and (b) $50^\circ$ .....	84
Figure 4.27 Photograph of the directional casting furnace and instrumented mould prior to casting.....	85
Figure 4.28 Grain structures of the casting trials with spiral take-off angle ( $\theta$ ) of: (a) $28^\circ$ ; (b) $50^\circ$ ; (c) $70^\circ$ and (d) a cylindrical selector .....	87
Figure 4.29 Predicted and experimentally observed results of heights for SX selection vs. take-off angle ( $\theta$ ).....	87
Figure 4.30 (a) Schematic of EBSD system and (b) the experiment set up for EBSD (Coleman, 2006).....	89
Figure 4.31 (a) Optical photograph of the cast spiral (Case 17); EBSD analyses on the grain structure evolution ((b1)-(d1)) and the corresponding $\langle 001 \rangle$ pole figures at different heights of: (b) 0 mm; (c) 12mm; (d) 24 mm; (e) 36 mm from the bottom of the spiral. ....	90
Figure 4.32 Predicted and experimentally observed results of final SX orientation vs. take-off angle ( $\theta$ ).....	91
Figure 4.33 Competitive growth controlled by the thermal gradient during investment casting.....	92
Figure 4.34 2D schematic diagrams of a geometrical control mechanism for grain selection in the spiral: (a) grain structure at the beginning of the solidification; grain structure evolution during solidification for different spiral geometries: (b) same geometry as in (a); (c) shorten pitch length ( $L_p$ ); (d) increase spiral take-off angle ( $\theta$ )	94
Figure 5.1 Schematics of casting defects in Ni-based superalloy for turbine blade (Jennings, 1996) (Courtesy of Rolls-Royce Plc.).....	97
Figure 5.2 Predicted microstructure of columnar dendrites after (a) 1; (b) 7; (c) 10; (d) 18s of growth .....	100
Figure 5.3 (a) Contour map of simulated solute profiles at columnar front after 10s growth; solute concentration along line (b) I-I; and (c) II-II.....	101
Figure 5.4 (a) Undercooling iso-contour map of the dendrite tips after 10s growth for the structure shown in Figure 5.3(a); (b) Undercooling in liquid region along line A-A and B-B .....	104
Figure 5.5 Calculated tip undercooling as a function of growth rate using the $\mu$ MatIC model.....	105

List of Figures

---

Figure 5.6 Dendrite growth and stray grain formation during solidification after: (a) 8s; (b) 10s; (c) 14s..... 107

Figure 5.7 Sliver formed in turbine blade (Jennings, 1996) (Courtesy of Rolls-Royce Plc.)..... 108

Figure 5.8 Formation of stray grains at the platform region in IN792 turbine blades (Courtesy of Rolls-Royce Plc.)..... 109

Figure 5.9 (a) The general shape of the isotherms in turbine blades during investment casting; (b) a schematic representation of dendrite growth into the platform region at different times, illustrating the high undercooling area and the dendritic patterns due to the effect of the platform geometry and the through-thickness gradient (Napolitano and Schaefer, 2000)..... 109

Figure 5.10 Predicted columnar-to-equiaxed transition lines from prior models. The solid curves are the CET lines calculated using the Hunt model for Al-1.5 wt. % Cu, Al-3 wt. % Cu and Al-6 wt. % Cu alloys (Hunt, 1984). The dashed curves are the CET lines using the GTK model (Gaumann et al. 1986) and Dong and Lee's predictions (2005) for Al-3 wt. % Cu alloys. .... 113

Figure 5.11 Effect of critical nucleation undercooling on the CET, for a range of mean nucleation undercooling: (a) 3K; (b) 4K; (c) 5K; (d) 6K; (e) 7K; (f) 8K..... 115

Figure 5.12 Effect of nuclei density in bulk liquid on the CET, for the maximum nuclei density of: (a)  $6.5 \times 10^{10}$ ; (b)  $6.5 \times 10^{11}$ ; (c)  $6.5 \times 10^{12}$ ; (d)  $6.5 \times 10^{13}$ ; (e)  $6.5 \times 10^{14}$  (nuclei/m<sup>3</sup>) ..... 116

Figure 5.13 Solidification ranges for different alloy concentrations in Al-Cu phase diagram..... 117

Figure 5.14 Progress maps showing the effect of alloy solidification range on the CET: open and filled symbols indicate equiaxed and columnar grains for (a) Al-1wt%Cu; (b) Al-3wt%Cu; (c) Al-5wt%Cu; (d) Al-7wt%Cu. The solid lines are the approximate CET lines separating the equiaxed and columnar regions. .... 118

Figure 6.1 Simulated dendrite structures in 3D and 2D at: (a)  $t=2s$ ; (b)  $t=6s$ ; (c)  $t=8s$  ..... 121

Figure 6.2 Solute contour maps of: (a) 3D dendrite structure after 8s; (b-l): longitudinal sections (parallel to X-Y plane) between two adjacent dendrite cores in 3D simulation; (m) 2D dendrite structure ..... 122

Figure 6.3 A comparison of solute concentration ( $C_E$ ) at dendrite tips along isothermal line in 3D through dendrite centre and 2D..... 124

Figure 6.4 Solute concentration along dendrite growth direction in the interdendritic region for 3D ( $Z=300 \mu\text{m}$  to  $Z=450 \mu\text{m}$ ) and 2D simulations (2D simulations are superimposed in (c)) ..... 125

Figure 6.5 Quantitative comparison of calculated solute profile ahead of dendrite tip using 2D and 3D  $\mu\text{MatIC}$  models and Hunt's 2D model..... 126

Figure 6.6 A schematic illustration of the solute distribution profile ahead of advancing solidification interface and the solute concentration at the wall of a growing cell. .... 127

Figure 6.7 Prefixed seeds with the primary spacing of  $\lambda_1$  at the bottom of the simulation domain: (a) square and (b) hexagonal configuration ..... 129

Figure 6.8 (a) Prefixed seeds at the bottom of the simulation domain; (b) simulated 3D dendritic structure after 6 seconds of growth; (c) a longitudinal section view along the x-y plane as indicated in (b) ..... 130

Figure 6.9 Simulated 3D dendritic structures grown from seeds with (a) square configuration and (b) hexagonal configuration after 6 s of growth; cross section views at different heights for dendrites packed in a square pattern – A1-A1, B1-B1 ( $Y=1300 \mu\text{m}$ ), A2-A2, B2-B2 ( $Y =1150 \mu\text{m}$ ), A3-A3, B3-B3 ( $Y =1000 \mu\text{m}$ ) and A4-A4, B4-B4 ( $Y=50 \mu\text{m}$ )..... 132

Figure 6.10 Schematics of tertiary branches developed from secondary arms during solidification in (a) square and (b) hexagonal packing configuration..... 133

Figure 6.11 Enlarged cross section views at  $Y=1000 \mu\text{m}$  as indicated in Figure 6.9, showing solute interaction between dendrites in: (a) cuboidal packing and (b) hexahedral packing pattern. .... 134

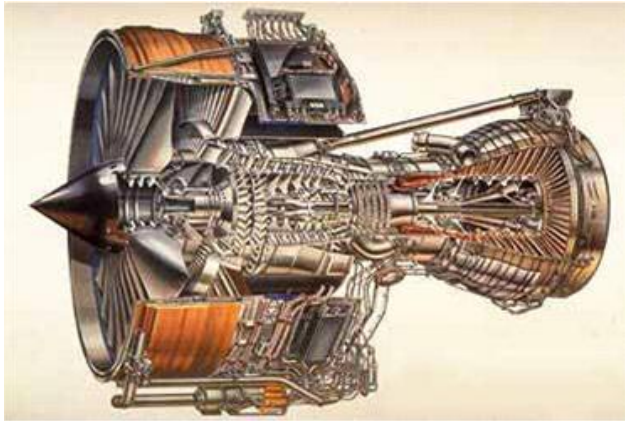
Figure 6.12 (a) Solute concentration at the S/L interface and the corresponding undercooling for square and hexagonal packing configuration; (b) effect of dendrite packing pattern on the solidus temperature in the schematic linearized binary phase diagram..... 136

## List of Tables

<i>Table 2-1 Chemical composition from conventional cast alloys to the 4<sup>th</sup> generation single crystal superalloys.....</i>	<i>6</i>
<i>Table 4-1 Spiral geometry used in this study.....</i>	<i>60</i>
<i>Table 4-2 Nominal composition (wt. %) of CMSX4 .....</i>	<i>85</i>
<i>Table 5-1 Nominal composition in wt. % of alloying elements in the Ni-based superalloys, IN792 (Courtesy of Rolls-Royce Plc.).....</i>	<i>98</i>
<i>Table 5-2 Material properties and model parameters used in the simulations.....</i>	<i>98</i>
<i>Table 5-3 The thickness of the diffusion layer ahead of the advancing solidification interface .....</i>	<i>102</i>
<i>Table 5-4 Nominal composition in wt. % of alloy BM and alloy GM .....</i>	<i>110</i>
<i>Table 5-5 Comparisons of liquidus temperature (<math>T_L</math>), carbide formation temperature (<math>T_C</math>), solidus temperature (<math>T_S</math>) and liquidus temperature difference (nucleation undercooling <math>\Delta T_L</math>).....</i>	<i>111</i>
<i>Table 5-6 Material properties and model parameters used in the simulations.....</i>	<i>114</i>
<i>Table 6-1 Comparison of solute concentration, grain density, average primary spacing and solidification range between cuboidal and hexahedral packing patterns .....</i>	<i>135</i>

## Chapter 1 Introduction

Aero-engine turbine blades sit in the severe environment behind the combustor and rotate at high speed in order to extract energy from the high temperature gas stream (Figure 1.1). The need to achieve increased efficiency and performance, while reducing cost and emissions, in aerospace propulsion and power generating gas turbines requires advanced single crystal Ni-based superalloys. In parallel with the alloy development, significant improvements in casting techniques have been achieved over the last 30 years by introducing the directionally solidified (DS) casting process followed by single crystal (SX) technique. However, newer generation single crystal alloys exhibit increased levels of solidification segregation which leads to the formation of casting defects.



(a)



(b)

**Figure 1.1** Rolls-Royce Trent 800 aero engine (a) and its turbine blade (b) (Image courtesy Rolls-Royce Plc.)

In collaboration with Rolls-Royce Plc., this project aims to use a multi-scale modelling method to simulate and optimize the solidification structure evolution and defect formation during the investment casting of turbine blades. Corresponding experiments have also been carried out to validate and compare with the simulation results.

In Chapter 2, a literature review is presented to describe the chemistry, processing and solidification structure of blade alloys. To facilitate a better understanding of the solidification phenomenon, the fundamental theory of solidification is reviewed.

Chapter 3 describes the models used in this study. The governing equations and assumptions for macro-scale ProCAST, meso-scale cellular automaton finite element (CAFE) and micro-scale  $\mu$ MatIC models are discussed.

In Chapter 4, a coupled macro-model ProCAST and meso-model CAFE is applied to simulate the grain selection during investment casting of single crystal turbine blades. Optimum dimensions and geometry of the spiral selector are investigated to improve the spiral efficiency. A sensitivity study is performed to validate the reliability of simulation results and experiments are carried out using a fully instrumented industrial directional casting furnace for validation. Based on the simulation and experimental results, the mechanism of grain selection in spiral selector is proposed to explain the competitive growth during solidification.

Chapter 5 quantitatively investigates the influence of casting conditions upon the formation of new grains ahead of advancing solidification front. Using a two-dimensional (2D) micro-scale  $\mu$ MatIC solidification model, solutal interaction and undercooling ahead of the growth front during solidification are examined. The columnar to equiaxed transition (CET) during the solidification are simulated and conditions leading the transition are quantified.

A three-dimensional (3D)  $\mu$ MatIC model is used in Chapter 6 to predict the complexity of cross section views of directionally solidified structures. The influence of dendrite packing pattern (cuboidal or regular hexahedral) on primary spacing adjustment during directional solidification is investigated. The importance of stereological effect on the modelling of the growth of solutal dendrites is discussed.

Conclusions of this study are drawn in Chapter 7, followed by recommendations for future work.

## Chapter 2 Literature Review

In this chapter, a brief review of the chemistry of blade alloys will be presented first. Gas turbine blades have complex geometries with intricate channels which allow gas flow during operation and are produced by investment casting. The development of investment casting techniques will be overviewed. This will be followed by a review of structure evolution and defect formation during casting. Finally, the fundamentals of solidification will be outlined to provide a background theory for understanding the solidification phenomenon during casting.

### 2.1 Chemistry of Blade Alloys

#### 2.1.1 Ni-based Superalloy for Turbine Blades

Aero-engine turbine blades are made of Ni-based superalloys. Superalloys are defined as a class of precipitate-strengthened alloys with superior mechanical strength, creep and oxidation resistance at elevated temperatures (Bradley, 1988). Compared with other alloys, Ni-based superalloys offer the best durability and specific strength over a much larger range of temperatures, especially when operating temperatures are beyond 800°C which is the case for gas turbines used for jet propulsion (Reed, 2006). These high temperature properties of Ni-based superalloys arise from: (1) Ni has a face centred cubic (FCC) crystal structure with high melting point which makes it ductile and tough; (2) Ni is stable in FCC crystal structure from room temperature to its melting point. Therefore, no phase transformation will occur to cause expansions and contractions which might complicate its use for high-temperature components; (3) diffusion rates in Ni are low which impart considerable microstructure stability at elevated temperatures and high creep resistance (Reed, 2006).

Most modern Ni-based superalloys are based on a Ni-6 wt. % Al system (Bradley, 1988). The Ni-Al binary phase diagram is shown in Figure 2.1 (Calculated by Henrik Larsson using Thermo-Calc<sup>TM</sup>) and the red dashed line indicates the alloy with 6 wt. % Al. At room temperature there are two phases,  $\gamma$  and  $\gamma'$ , in the system. The

microstructure of  $\gamma$  and  $\gamma'$  phases is illustrated in Figure 2.2 (Caron and Khan, 1999).  $\gamma$  phase is a solid solution with a face centred cubic (FCC) crystal structure and a random distribution of the different species of atoms (shown in Figure 2.3 (a)). While in  $\gamma'$  phase, Ni atoms locate at the face centre and Al atoms at the cubic corner points, which makes the chemical formula  $\text{Ni}_3\text{Al}$  (Figure 2.3 (b)) (Bhadeshia, Cambridge).

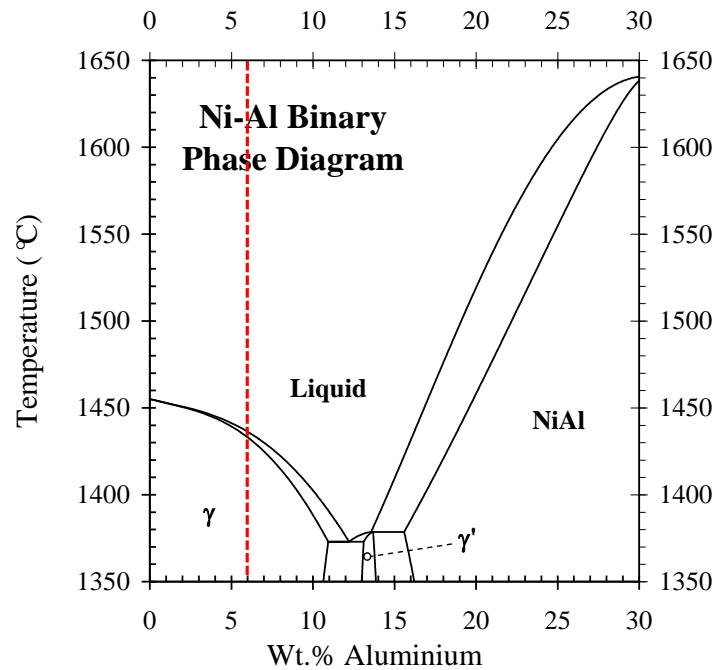


*Figure 2.1 Al-Ni binary phase diagram (Calculated using Thermo-Calc)*

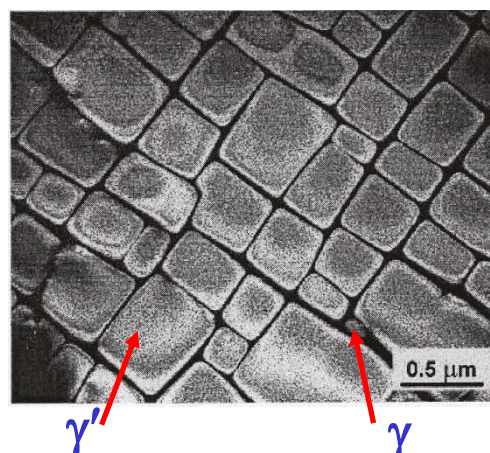


*Figure 2.2 Scanning electron micrograph of the  $\gamma/\gamma'$  microstructure of single-crystal Ni-based superalloy (Caron and Khan, 1999)*

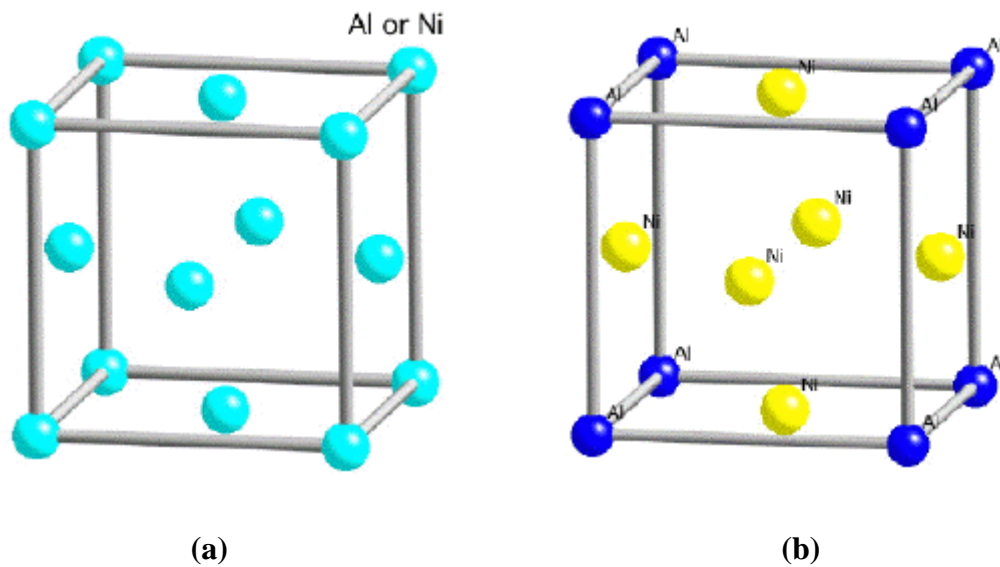


*Figure 2.3 Crystal structures of  $\gamma$  (a) and  $\gamma'$  (b) phases in Ni-based superalloys (Bhadeshia, Cambridge)*

The cube-cube relationship makes the cell edges of these two phases exactly parallel, and the similar lattice parameters make the  $\gamma'$  phase coherent with the  $\gamma$  phase when the precipitate size is small. The coherent  $\gamma'$  phase strengthens the alloy by interfering with dislocation motion. Furthermore, the small misfit between  $\gamma$  and  $\gamma'$  lattices contributes positively to the stability of microstructure and the magnitude of this misfit will affect the change of microstructure under the influence of the stress at elevated temperatures (Hillier *et al.* 1988).

The amount of  $\gamma'$  phase and the misfit between  $\gamma$  and  $\gamma'$  lattices can be controlled by altering chemical composition and the processing conditions, which will be discussed in the following section.

### 2.1.2 Chemistry Development of Blade Alloys

Modern Ni-based blade superalloys are complex alloy systems constituted of more than ten alloying elements. In the last 70 years, the chemistry of Ni-based superalloys has been refined to improve the performance of the blades. The chemical modification from

conventional cast alloys to the up-to-date single crystal superalloys of the fourth generation is listed in Table 2-1 (Reed, 2006; Nakagawa, 2004; Walston *et al.* 1996).

**Table 2-1 Chemical composition from conventional cast alloys to the 4<sup>th</sup> generation single crystal superalloys**

	Alloy	Cr	Co	Mo	W	Ta	Re	Nb	Al	Ti	Hf	C	B	Y	Zr	Ru
Conventional Cast Alloys	Mar-M246	8.3	10.0	0.7	10.0	3.0			5.5	1.0	1.50	0.14	0.02		0.05	
	IN 100	10.0	15.0	3.0					5.5	4.7		0.18	0.01		0.06	
	Rene 80	14.0	9.5	4.0	4.0				3.0	5.0		0.17	0.02		0.03	
Directionally Solidified Alloys	IN 792	12.6	9.0	1.9	4.3	4.3			3.4	4.0	1.00	0.09	0.02		0.06	
	GTD 111	14.0	9.5	1.5	3.8	2.8			3.0	4.9		0.10	0.01			
1 <sup>st</sup> Generation SX Alloys	PWA 1480	10.0	5.0		4.0	12.0			5.0	1.5						
	Rene N4	9.8	7.5	1.5	6.0	4.8		0.5	4.2	3.5	0.15	0.05				
	CMSX-3	8.0	5.0	0.6	8.0	6.0			5.6	1.0	0.10					
2 <sup>nd</sup> Generation SX Alloys	PWA1484	5.0	10.0	2.0	6.0	9.0	3.0		5.6		0.10					
	Rene N5	7.0	7.5	1.5	5.0	6.5	3.0		6.2		0.15	0.05		0.01		
	CMSX-4	6.5	9.0	0.6	6.0	6.5	3.0		5.6	1.0	0.10					
3 <sup>rd</sup> Generation SX Alloys	Rene N6	4.2	12.5	1.4	6.0	7.2	5.4		5.8		0.15	0.05		0.01		
	CMSX-10	2.0	3.0	0.4	5.0	8.0	6.0	0.1	5.7	0.2	0.03					
	TMS-75	3.0	12.0	2.0	5.0	6.0	5.0		6.0		0.1					
	RR2100	2.5	12		9.0	5.5	6.4		6.0		0.15					
4 <sup>th</sup> Generation SX Alloys	MC-NG	4.0	0.2	1.0	5.0	5.0	4.0		6.0	0.5	0.1					4.0
	RR2101	2.5	12		9.0	5.5	6.4		6.0		0.15					2.0

In conventionally cast (CC) and directionally solidified (DS) alloys, minor elements such as C, B, Zr, Hf are used to strengthen grain boundaries. In the 1<sup>st</sup> generation single crystal (SX) superalloys, these grain boundary strengthening elements are removed and a large amount of refractory elements such as W, Ta, Mo are introduced to increase the incipient melting temperature and optimize the mechanical properties for superalloys (Erickson, 1995). As shown in Figure 2.4, the overall performance of the 2<sup>nd</sup> and 3<sup>rd</sup> generations SX superalloys has been significantly improved by the addition of increasing amounts of Re (3 wt. % and 6 wt. % respectively). However, the increased difference in density and diffusivity leads to a requirement for the careful control of the level of the various alloying elements. In respond to demand, the 4<sup>th</sup> generation SX superalloys are developed by adding Ru to boost structural stability, resulting in the

development of MC-NG and RR2101 (Caron and Khan, 1999; Nakagawa, 2004; Reed, 2004; Yeh and Tin, 2005; Yeh and Tin, 2006; Hobbs *et al.* 2007).

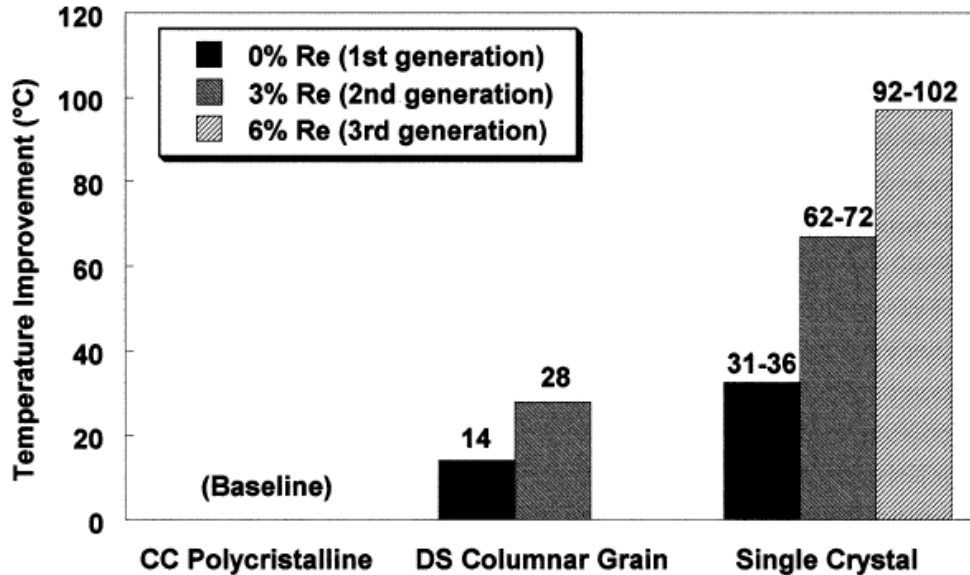


*Figure 2.4 Typical temperature advantages over CC superalloys obtained with DS and SX superalloys estimated from stress rupture tests performed at 982°C and 248 MPa (Erickson, 1995)*

The effects of individual elements on alloy performance are listed as follows (Meetham 1981; Bradley, 1988; Erickson, 1995; Walston *et al.* 1996; Caron and Khan, 1999; Wong, 2003; Zhang, 2003; Al-Jarba and Fuchs, 2004; Nakagawa, 2004; Yeh and Tin, 2005; Reed, 2006; Hobbs *et al.* 2007):

Al: promotes the creation of the  $\gamma'$  phase and plays a fundamental role in promoting the formation of a stable  $\text{Al}_2\text{O}_3$  alumina surface scale which protects the alloy against further oxidation.

Cr: acts as a solid solution strengthening element and plays an essential role in the hot corrosion and oxidation resistance. Cr also forms the topologically close-packed brittle phase (TCP), and the TCP phase is detrimental to high temperature properties of the turbine blades.

Co: contributes to the strength by ordering  $\gamma'$  phase particles homogeneously distributed in the  $\gamma$  matrix.

Mo: strengthens the  $\gamma/\gamma'$  phases but has a negative influence on the corrosion resistance of Ni-based superalloys.

W: improves high temperature capability, segregates strongly to the  $\gamma$  dendrites and increases the potential for nucleation and growth of grain defects at high levels of W.

Ta: strengthens the  $\gamma'$  precipitates by substituting for Al in  $\gamma'$ , particularly increasing high-temperature strength. Ta segregates to the interdendritic region so can decrease the density inversions which will cause the nucleation of spurious grains. Ta is also beneficial for environmental properties.

Re: improves high temperature capability, hot corrosion and oxidation resistance at the expense of density and microstructure stability. Re has played an key role in the evolution of single crystal superalloys.

Nb, Ti, Ta: strengthen the  $\gamma'$  precipitates by substituting for Al in  $\gamma'$ , particularly increasing high-temperature strength. However, an excessive amount of these elements makes alloys prone to TCP phase precipitation.

Hf: improves alloys coatability.

C: contributes positively to castability since it helps in reducing the oxides and is a grain boundary strengthening element.

B, Zr: strengthen the grain boundaries but lower the incipient melting point.

Y: improves the adherence of the  $\text{Al}_2\text{O}_3$  protective layer formed at high temperature.

Ru: boosts the stability of alloy structure and increases the strength but is expensive.

## 2.2 Processing

Development of new blade alloys to achieve high temperature performance has required parallel development in alloy processing. Before the 1940s, gas turbine engine blades were iron-based alloys through cold wrought. In the 1940s and 1950s, investment casting and vacuum melting were introduced to manufacture engine blades. In the 1970s, the directional solidification (DS) process was invented and made a great advance in the thermal capability of the blades. The grain boundaries were significantly decreased and the crystals were all aligned in the direction of centrifugal stress. Based on the DS casting process, single crystal (SX) blades were exploited, which are free from high angle grain boundaries and therefore dramatically increase the melting point of turbine blades (Reed 2006; Caron and Khan, 1999). To date, all the modern Trent family of engines incorporate single crystal materials. The microstructure development of casting turbine blades is shown in Figure 2.5 (Wong 2003).

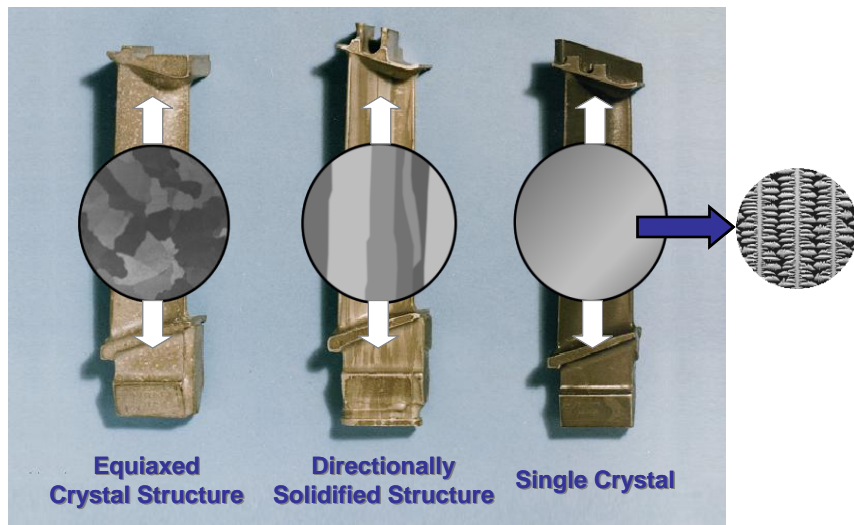
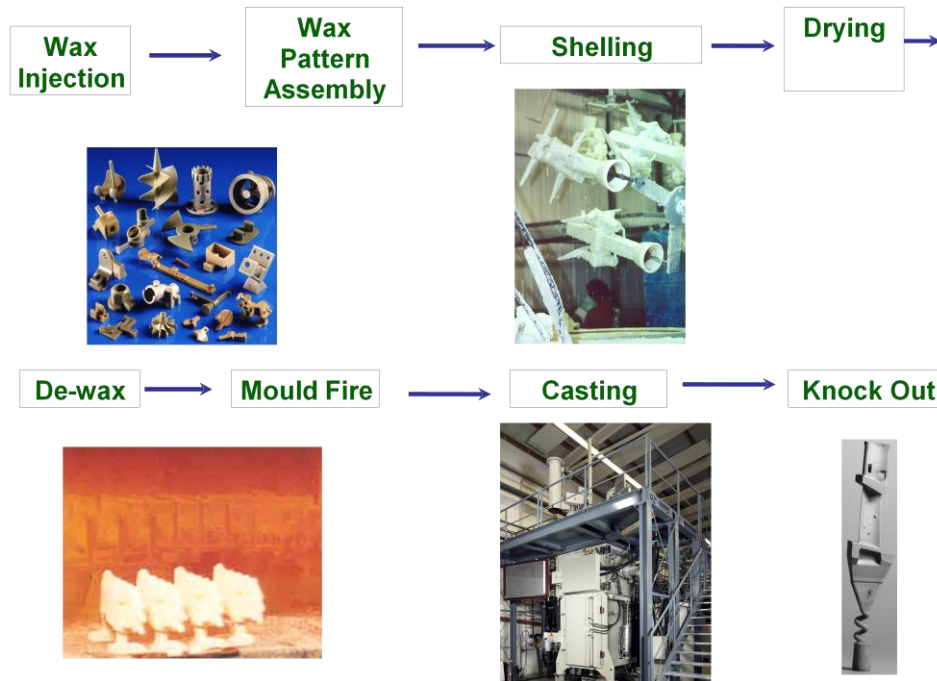


*Figure 2.5 The microstructure development of casting turbine blades from equiaxed crystal structure to single crystal (Wong, 2003)*

Nowadays, turbine blades are designed with complex geometries and intricate channels which allow cooler air flow within and along the blades during operation (Nakagawa, 2004). Therefore, turbine components are usually produced by investment casting. As

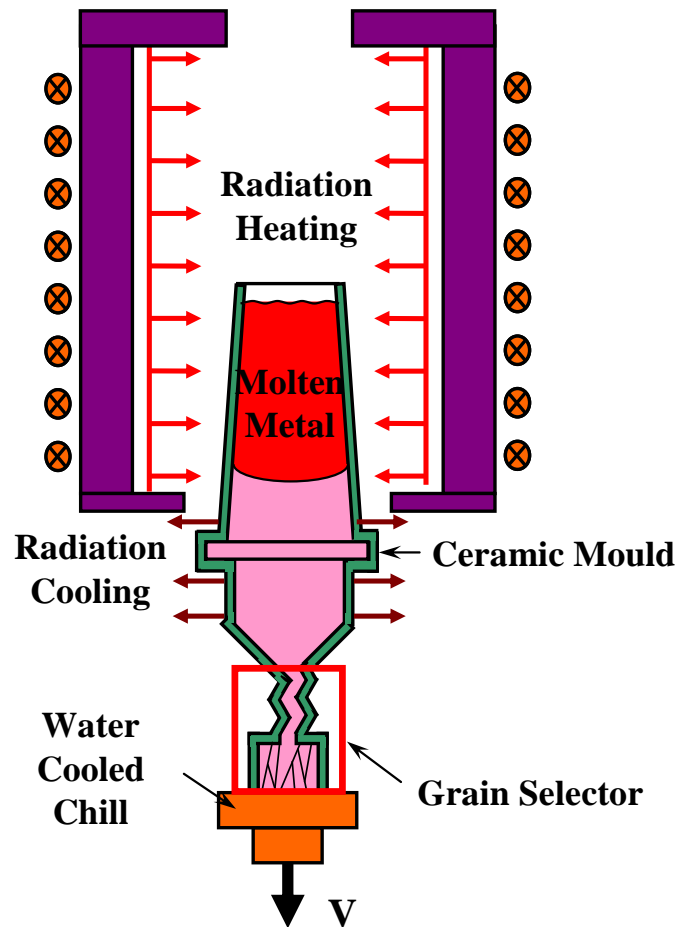
shown in Figure 2.6, the investment casting process (also called lost-wax casting) involves the following steps (Campbell, 2003):

1. A pattern of the component of the casting is prepared by injecting molten wax into a metal mould. If necessary (such as for cooling passages in turbine blades), ceramic cores can be prefixed into the mould to intricate hollows for the castings. Wax patterns can be assembled in clusters to enable several blades to be produced in a single casting.
2. The wax mould is then dipped into ceramic slurry consisting of binding agents and mixtures of zircon ( $ZrSiO_4$ ), alumina ( $Al_2O_3$ ) and silica ( $SiO_2$ ), followed by stuccoing with larger particles of the above materials. This process needs to be repeated several times until the shell thickness is thick enough to withstand the mechanical shock of receiving the molten metal.
3. After the shell is constructed, the wax is removed in an autoclave or furnace.
4. The ceramic mould is then fired to high temperature to build up its strength and make it ready to receive the molten superalloy.
5. When the casting is finished, the investment shells are knocked off and the ceramic cores are leached out using a high-pressure autoclave by chemical means.



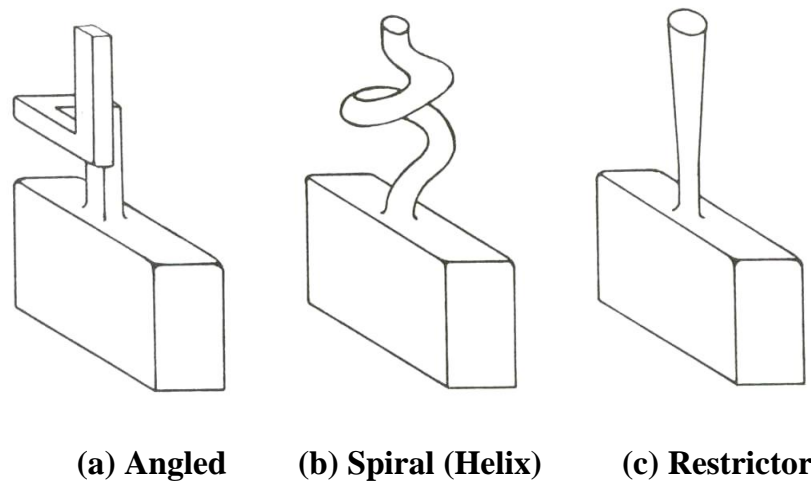
**Figure 2.6 Illustration of the various stages of investment casting process**

Figure 2.7 illustrates the investment casting furnace for single crystal turbine blades. Based on directional solidification (DS), the molten alloy is poured into a hot ceramic mould at a temperature of approximately  $1500^{\circ}\text{C}$ , which is maintained by radiant heating in the furnace. A water-cooled copper chill plate is located at the bottom to make the solidification start at the bottom. During solidification, the solid-liquid growth front can be controlled by heat flow in the mould. By slowly withdrawing the mould out of the furnace, metal solidifies directionally from bottom to top, producing large, columnar grains which are elongated in the direction of withdrawal, markedly improving the creep properties. In single crystal (SX) castings, to entirely remove the transverse grain boundaries, a grain selector is added at the base of the mould. As a result, only one grain with a preferred orientation can eventually survive at the top of the grain selector and grow into the main body of the turbine blades, which allows free of high angle boundaries (HABs) in SX superalloys. Since HABs are preferential sites for crack initiation, creep resistance of SX alloys can be dramatically improved. Depending on the size of the blade, the entire process takes 3-6 hours to complete.



*Figure 2.7 Schematic illustration of investment casting for single crystal turbine blades*

To further control the quality of the single crystal turbine blades, particular attention has been paid to grain selectors. Different designs of grain selector are employed as shown in Figure 2.8 (Goulette, 1984). The most common type is the spiral grain selector which is often known as the ‘pig-tail’ grain selector (Figure 2.8 (b)). It consists of two parts: a starter block unit referring to competitive growth for the grain orientation optimisation and a spiral grain selector facilitating dendrite branching to ensure that only one single grain eventually survives at the top of the seed. However, there is no standard practice for grain selector design and it is based on a trial-and-error optimisation in an Edisonian style. As a result, the grain selection sometimes fails, leading to non-conformance and unnecessary waste.



**Figure 2.8 Various designs of grain selector for single crystal turbine blades (Goulette, 1984)**

To improve the efficiency of the grain selector, several studies have been carried out recently. As shown in Figure 2.9, a 2D analytical model is used by Esaka *et al.* (2005) to investigate the effect of the shape of grain selector on the efficiency of grain selection during casting. Grain selection in the starter block has also been studied by Carter *et al.* (2000) using a 3D processing model based upon a thermal analysis of the heat transfer occurring in a commercial casting furnace and a cellular-automaton model for competitive dendrite growth. It is pointed out that the majority of the primary grain orientation selection occurs in the starter block. However, the issue of grain selection in the spiral has not been studied. In Chapter 4, a systematic study on the grain selection in the spiral will be performed using numerical simulation and experimental validation. Quantitative description of effects of spiral geometry and dimensions on the grain selection will be investigated to improve the efficiency of grain selectors and provide a better understanding of grain selection mechanisms in the spiral. Based on the research, more efficient grain selectors will be designed for newly developed alloys.

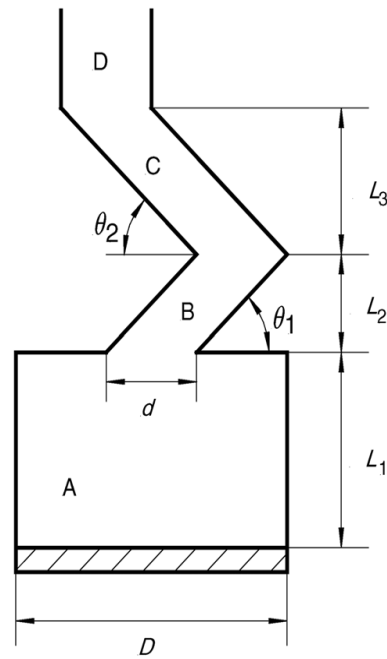


**Figure 2.9** A schematic drawing of the grain selector design used in a 2D analytical model (Esaka *et al.* 2005)

## 2.3 Microstructure Evolution during Casting

The microstructure of a casting is of great importance since many material properties, especially mechanical properties, depend on the grain shape and grain size. Furthermore, segregation resulting from solute partitioning during solidification can have significant effects. In this section, the fundamentals of dendrite study including, dendritic structures and dendrite primary spacing, will be reviewed to better understand the evolution of solidification structure. The competitive growth mechanism during solidification will also be discussed.

### 2.3.1 Dendritic Structure Evolution

Dendrites are the most prevalent structure in casting alloys, and the pattern of dendrites determines the final properties of castings (Hunt 1984; Pollock *et al.* 1992; Kurz and Fisher, 1984). Generally two distinct forms of dendritic structures, columnar and equiaxed dendrites, exist in castings. The structure is called columnar if the growth is

preferentially oriented in a direction close to the heat flux, whereas equiaxed grains are growing in all directions, leading to a material with more isotropic macroscopic mechanical properties and a more homogeneous composition field than those with columnar microstructure.

In casting of metallic alloys, a transition from columnar grain structure to equiaxed grain structure can be observed (Figure 2.10) (Campbell, 2003).

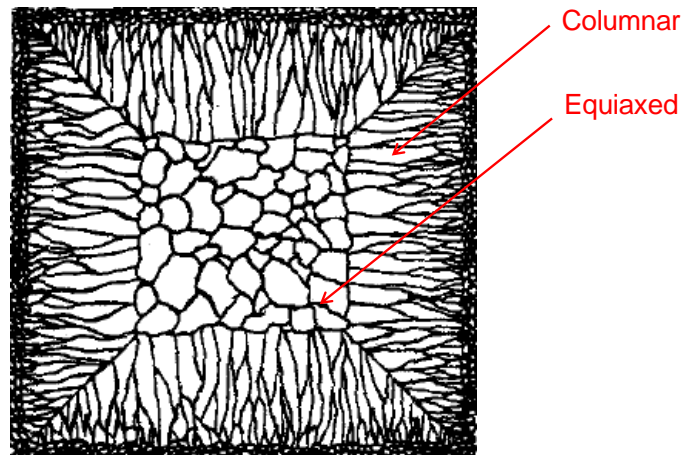


**Figure 2.10 Columnar-to-equiaxed transition (CET) in casting process (Campbell, 2003)**

This columnar-to-equiaxed transition (CET) is of high technological relevance both from the metallurgical point of view and for the understanding of the fundamentals related to physical phenomena, since the dendrite structures in cast alloys contribute significantly to the final properties of components manufactured from them (Pollock *et al.* 1992; Campbell, 2003; Dogan, 1996; Gaumann *et al.* 2001; Hua and Grugel, 1996; Hunt, 1984; Kurz *et al.* 2001; Kurz *et al.* 1986; Kurz and Fisher, 1984).

Figure 2.11 (Kearsey, *et al.* 2004) shows the 3D columnar dendritic morphology in single crystal (SX) superalloys used for turbine blades. All the primary dendrites are aligned with the same direction and free of high angle boundaries, resulting in a great improvement in the creep rupture life.

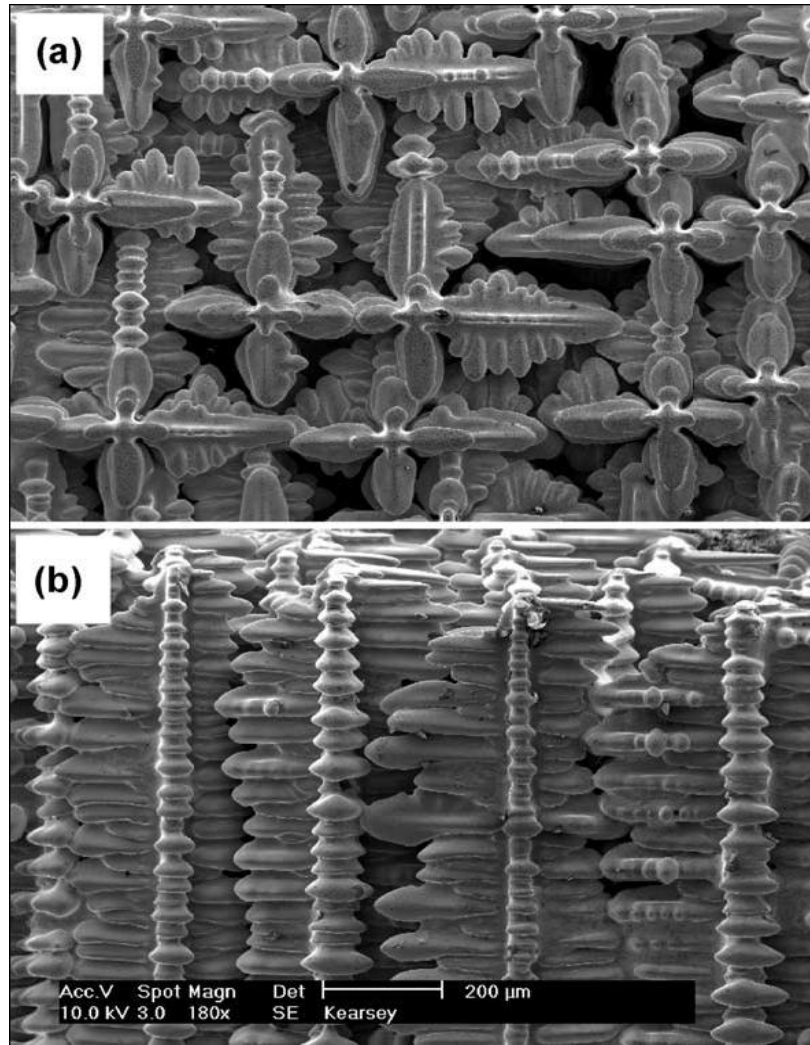


**Figure 2.11** Scanning electron image showing the 3D dendritic morphology of single crystal Ni-based superalloy for both (a) transverse and (b) longitudinal directions (Kearsey et al. 2004)

To achieve the columnar dendrite structure, high temperature gradients in front of the solid/liquid (S/L) interface and low solidification velocities are used to prevent the formation of equiaxed grains (Dong and Lee, 2005). Detailed investigations on the control of solidification structure and stray grain formation in Ni-based superalloys will be discussed in Chapter 5.

### 2.3.2 Primary Spacing in Dendrites

Dendrites have many characteristic structural length scales such as dendrite tip radius and primary and secondary dendrite spacing as illustrated in Figure 2.12.

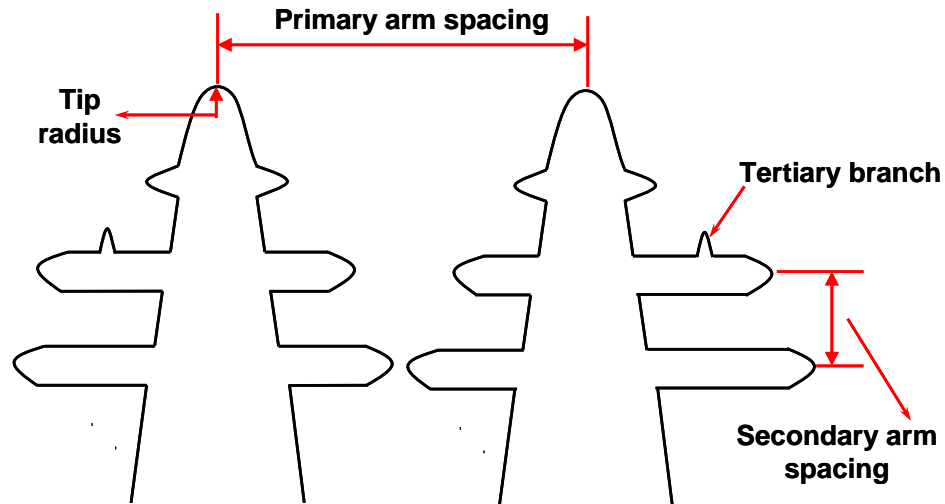


**Figure 2.12** Length scales used in dendrite study

For directional solidification applications where the structure is mainly columnar dendrites, the primary spacing ( $\lambda_1$ ) characterizes the maximum length scale for the segregation of alloying elements (Kurz and Fisher, 1984). As shown in Figure 2.13 (after Kearsey *et al.* 2004), the bright colour stands for the dendrites while the dark colour stands for the interdendritic regions. During solidification, some elements like Re and W prefer to accumulate to the dendrite core while the other elements like Al, Ti and Ta prefer to accumulate in the interdendritic (ID) region. The primary spacing ( $\lambda_1$ ) indicates the maximum length scale for the segregation and will affect solutioning time afterwards. Generally speaking, solutioning time is proportional to the square of primary spacing ( $\lambda_1$ ). This means if the dendrite primary spacing ( $\lambda_1$ ) can be decreased to half, the required solutioning time will be reduced to a quarter, which will significantly reduce the cost in heat treatment. It has also been found that the primary dendrite arm spacing affects both the processing of alloys and the final thermal mechanical properties of the component (McLean, 1983). Therefore, a fine spacing is

sought to reduce the propensity for casting defects, minimise heat treatment time, and improve mechanical properties.

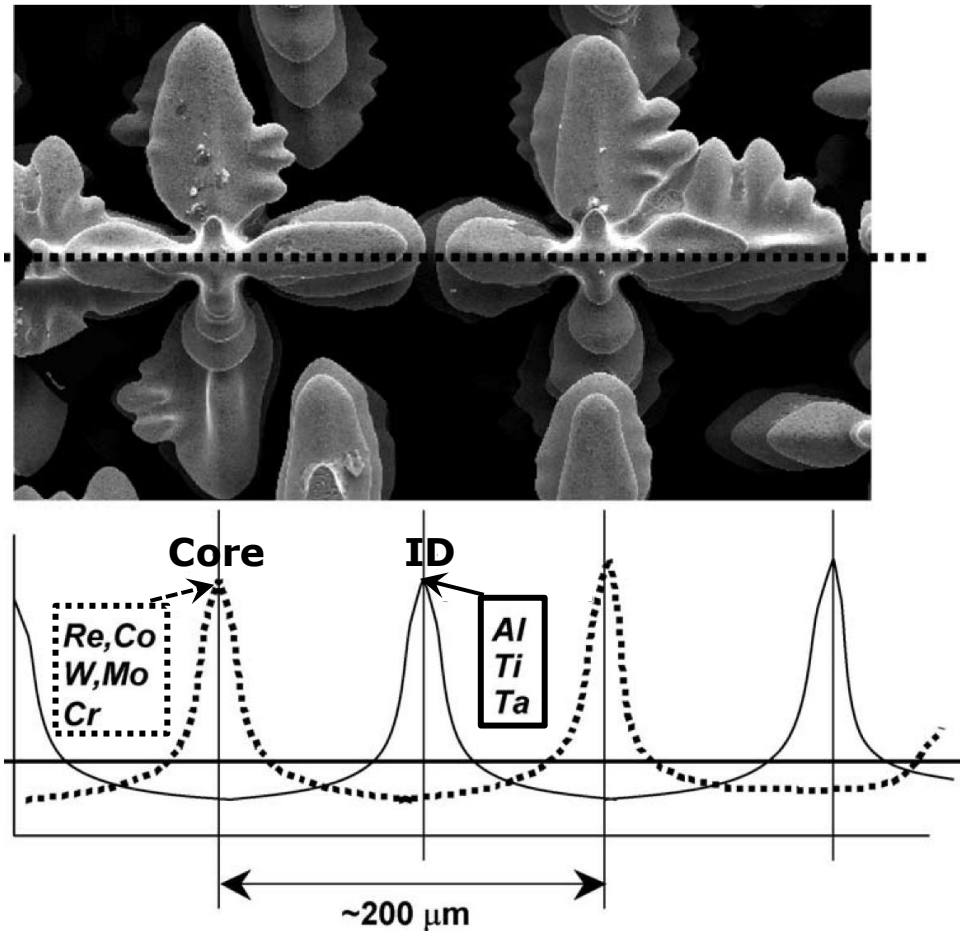


**Figure 2.13** Illustration of micro-segregation in the transverse section of Ni-based single crystal superalloy (after Kearsey *et al.* 2004)

Early studies characterized the spacing as a unique value for a given condition (Kurz and Fisher, 1984), but later studies have illustrated that a range of primary spacings are possible for any given set of growth conditions and a small range of dendrite primary spacings can be present in a directionally grown sample (Huang *et al.* 1993). Experimental observations suggested (Hunt, 1979) that the spacing range is governed by overgrowth at the minimum end and branching at the maximum end of the range. If a member of the dendrite array has a spacing which is too small, it will be overgrown by

its neighbours (Figure 2.14 (a)). If the spacing is too large a new primary dendrite will form by the growth of a tertiary arm (Figure 2.14 (c)).

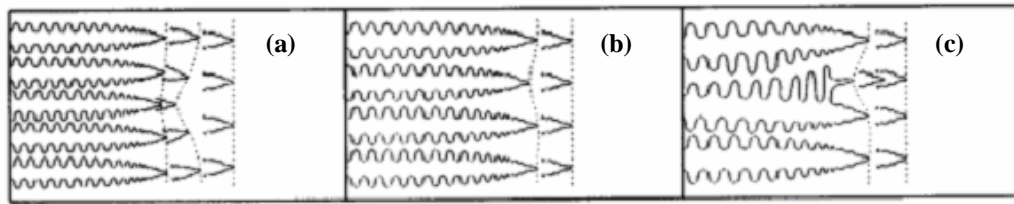


**Figure 2.14** A schematic diagram showing the primary spacing change mechanisms for dendrites: a) overgrowth; b) steady state; and c) branching (Hunt, 1979)

Stability analysis of the solid/liquid interface by perturbing the solidification front (Warren and Langer, 1990) predicted the lower bound in an allowable velocity range, but not the upper bound. Calculations from a numerical model developed by Hunt and Lu (1986) also suggested a solute interaction limit to determine the lower band of spacing. Again branching was not included in this model, and therefore the upper limit was estimated to be twice as the lower limit. To gain a better understanding of the primary spacing, a model which is capable of simulating branching is required. In chapter 6, a three-dimensional (3D) micro-model  $\mu$ MatIC will be developed to simulate dendrite growth with emphasis on branching during solidification. Based on the investigation of the complexity of cross section views of directionally solidified structures, the influence of dendrite packing patterns (cuboidal or regular hexahedral) on primary spacing adjustment will be investigated.

### 2.3.3 Competitive Growth Mechanism

Since structure control during single crystal investment casting depends strongly on the competitive growth of dendrites, understanding the underlying mechanism becomes vital. Figure 2.15 illustrates the schematics of the competitive growth during solidification (Rappaz and Gandin, 1993).

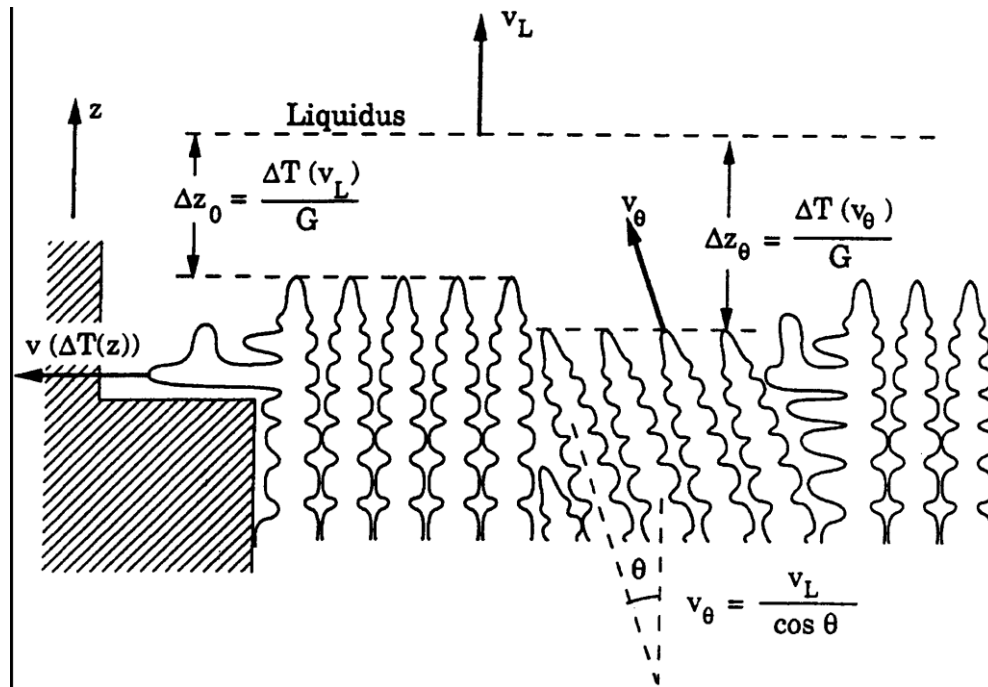


**Figure 2.15 Schematic representation of dendrite growth illustrating the mechanism of competitive growth during directional solidification (Rappaz and Gandin, 1993)**

As shown in Figure 2.15, grains on the left and right contain dendrites with preferred growth direction  $\langle 001 \rangle$  well-aligned with the thermal gradient and they grow with the same rate,  $v_L$ , as the velocity of the liquidus isotherm. The grain shown in the middle has a mis-aligned angle of  $\theta$  with respect to the direction of thermal gradient. To keep up with the better aligned neighbours, it must grow with a larger growth rate:  $v_\theta = v_L / \cos\theta$ . Since the growth rate during solidification is determined by the local tip undercooling (Kurz and Fisher, 1984), the mis-aligned grains in the middle then are characterized by a larger undercooling ( $\Delta z_\theta > \Delta z_0$ ). This difference in undercooling makes the mis-aligned grains fall behind and creates the competitive growth mechanism in two situations: converging and diverging.

In a converging case which is shown on the left in Figure 2.15, it is difficult for the secondary arms to develop from the primary dendrites because of the strong solutal interaction. Since the mis-aligned grains are behind the well-aligned grains due to the local undercooling, the dendrite tips of mis-aligned grains will hit the side of well-aligned grains and be blocked, generating a grain boundary which is always in the same

direction as the growth direction of the well-aligned grains (Rappaz and Gandin, 1993). However, recent experimental analysis on bi-crystal samples during directional solidification (Zhou *et al.* 2008) shows that the mis-aligned grain was able to overgrow the well-aligned grain by blocking its primary dendrite chunks by branching at different longitudinal planes.

In a diverging case shown on the right in Figure 2.15, the open space between the two grains offers the opportunity for the secondary arms of mis-aligned dendrites to develop, and then the tertiary arms will branch from the secondary arms to adjust the dendrite spacing and to compete with exist other primary dendrite arms during solidification. As a result, the well-aligned grain will eventually overgrow the mis-aligned grain and generate a grain boundary with an inclined angle which is equal to one third of the angle difference between these two touching grains (Zhou *et al.* 2008). Compared with the competitive growth mechanisms for converging and diverging situations, grain growth in a single crystal grain selector during solidification will be discussed in Chapter 4.

## **2.4 Theory of Solidification**

To facilitate a better understanding of the microstructure evolution and defect formation during solidification, it is important to grasp the fundamentals of physical principles associated with it.

Solidification is a phase transformation from liquid phase to one or several solid phases which involves the solute diffusion and latent heat (Kurz and Fisher, 1984). The solidification process starts with grain nucleation and continues with grain growth, the principles of which are briefly reviewed in this section.

### **2.4.1 Grain Nucleation**

From a thermodynamic point of view, nucleation is the onset of phase transformation. There are two forms of nucleation: homogeneous nucleation and heterogeneous nucleation.

Homogeneous nucleation occurs spontaneously and randomly when there are no preferential nucleation sites by the aid of foreign materials (Flemings, 1974). It involves creation of crystal clusters, each of which has an interface between liquid and solid phases and requires undercooling. Homogeneous nucleation is driven by the change in Gibbs free energy,  $\Delta G$ , including the interface term,  $\Delta G_I$ , and volume term,  $\Delta G_V$ . Assuming the nucleus has a spherical shape,  $\Delta G$  can be written as (Kurz and Fisher, 1984),

$$\Delta G = \Delta G_I + \Delta G_V = 4\pi r^2 \sigma - \frac{4\pi r^3}{3} \Delta g \quad (2.1)$$

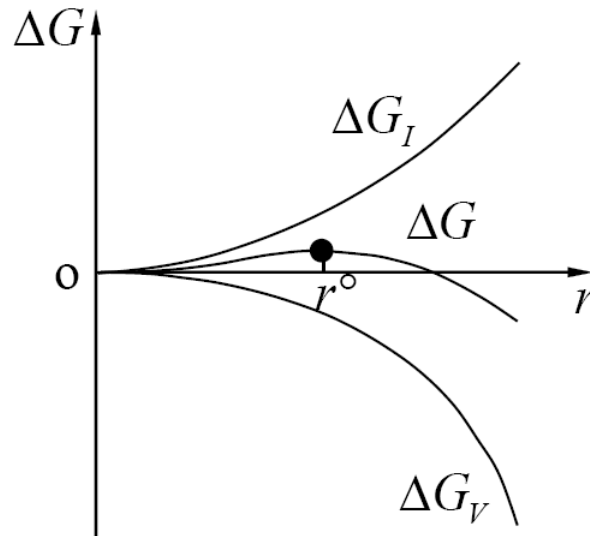
where  $\sigma$  is the solid/liquid interface energy,  $r$  is the nucleus radius and  $\Delta g$  is the Gibbs free energy difference between the liquid and solid per unit volume.

As shown in Figure 2.16, the nucleus has to exceed a critical radius to be stable. Setting

$\frac{d}{dr}(\Delta G) = 0$  in Equation 2.1, the critical radius  $r^\circ$  can be calculated,

$$r^\circ = -2\sigma/\Delta g \quad (2.2)$$

The occurrence of homogeneous nucleation is limited to very restricted situations and normally requires a high degree of undercooling. When the melt contains solid particles or is in contact with mould wall or oxide layer, nucleation may be facilitated because the activation energy required is decreased. This is known as heterogeneous nucleation (Kurz and Fisher, 1984).



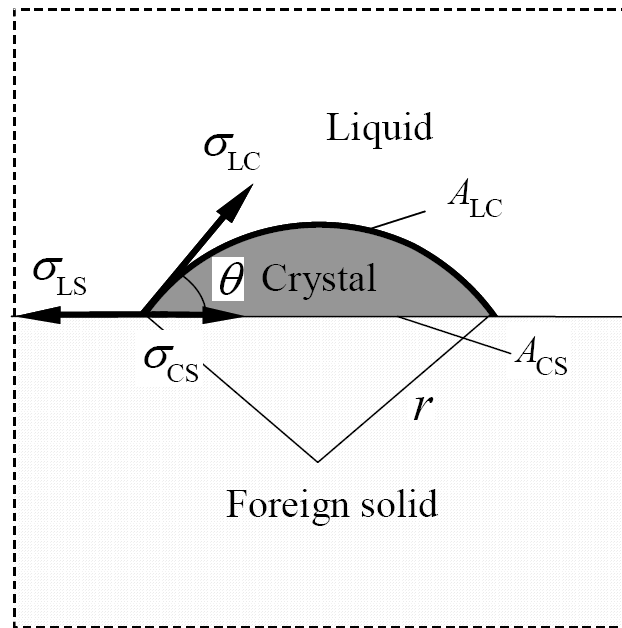
**Figure 2.16 Gibbs free energy change associated with homogenous nucleation having a spherical shape (Kurz and Fisher, 1984)**

Figure 2.17 illustrates the heterogeneous nucleation on the surface of a foreign solid. The wetting angle  $\theta$  is defined as the contact angle between the nucleus (crystal) and the foreign solid. The solid/liquid (S/L) interface is partly replaced by the crystal/solid (C/S) interface between the crystal and foreign solid which has low energy ( $A_{CS}$  in Figure 2.18). To grow a stable crystal, the energy required for heterogeneous nucleation  $\Delta G_{Het}$  is given by,

$$\Delta G_{Het} = \Delta G \cdot f(\theta) \quad (2.3)$$

$$f(\theta) = \frac{(2 + \cos\theta)(1 - \cos\theta)^2}{4} \leq 1 \quad (2.4)$$

Therefore, activation energy for heterogeneous nucleation is reduced which means heterogeneous nucleation occurs more easily than homogeneous nucleation. Moreover, control of the heterogeneous nucleation can be affected by control of the wetting angle ( $\theta$ ) via selecting appropriate crucible materials or adding appropriate nucleation agents which will be further discussed in Chapter 5.



**Figure 2.17** Schematics of heterogeneous nucleation; the wetting angle is defined as the angle between the nucleus (crystal) and the foreign solid (Kurz and Fisher, 1984)

## 2.4.2 Growth Kinetics

Once an embryo has exceeded the critical size and become a stable nucleus, growth kinetics start to dominate the solidification process. For pure materials, solid growth is determined by the heat of fusion. While for alloys, it is affected by both solute diffusion and heat transfer during solidification.

### 2.4.2.1 Diffusion

In the absence of convection, the transformation of liquid into solid is a diffusion-controlled process. The diffusion of both solute and heat need to be considered, which are given by the governing equations:

For solute:

$$\frac{\partial C}{\partial t} = \nabla \cdot (D \nabla C) \quad (2.5)$$

For heat:

$$\frac{\partial T}{\partial t} = \nabla \cdot (\alpha \nabla T) \quad (2.6)$$

$$\alpha = \frac{K}{\rho C_p} \quad (2.7)$$

Where  $D$  is the solute diffusion coefficient for composition  $C$ ,  $\alpha$  is thermal diffusivity which is defined by Equation 2.7,  $K$  is thermal conductivity,  $\rho$  is density and  $C_p$  is specific heat per unit volume.

For binary alloy ( $k < 1$ ), a typical linearized phase diagram is illustrated in Figure 2.18 (Chilton, 2002).

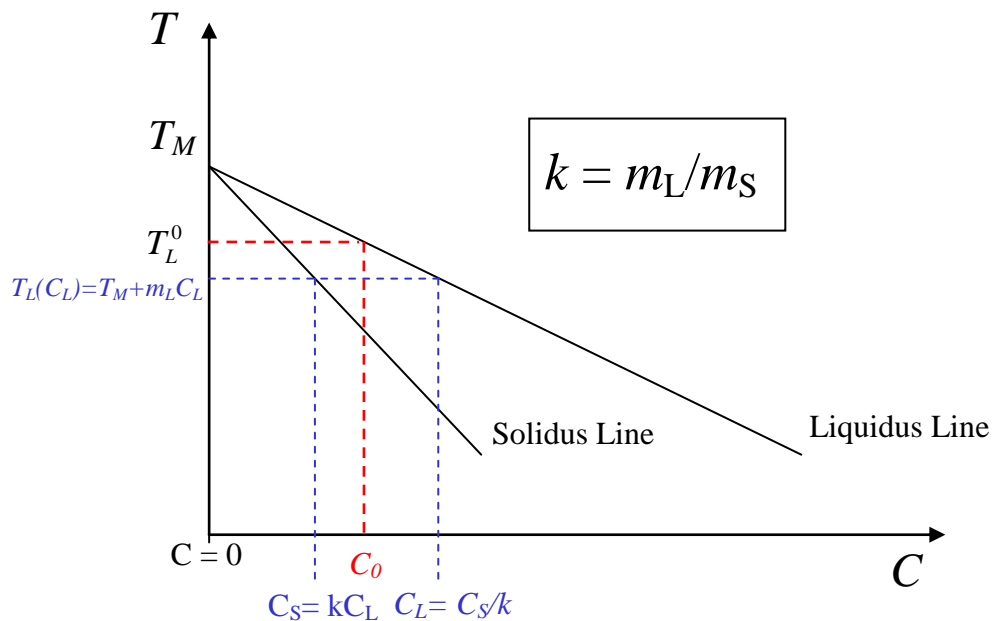


**Figure 2.18** Low concentration end of a phase diagram for a typical binary alloy ( $k < 1$ ). The solidus and liquidus are assumed to be approximately straight lines of gradients  $m_s$  and  $m_L$ , respectively (Chilton, 2002)

The slopes of liquidus and solidus are  $m_l$  and  $m_s$  respectively, the ratio of which is defined as the partition coefficient  $k$ ,

$$k = m_L / m_S \quad (2.8)$$

which is constant in this case. Therefore, the compositions in the liquid ( $C_L$ ) and solid ( $C_S$ ) phases are related by,

$$C_S = k C_L \quad (2.9)$$

During solidification, solute diffusion in the liquid and solid is governed by the following equations (Kurz and Fisher, 1984),

$$\frac{\partial C_L}{\partial t} = \nabla \cdot (D_L \nabla C_L) \quad (2.10)$$

$$\frac{\partial C_S}{\partial t} = \nabla \cdot (D_S \nabla C_S) \quad (2.11)$$

According to the solute redistribution during solidification, two extreme cases can be assumed, the equilibrium and the Scheil conditions. Figure 2.19 (Flemings, 1974) demonstrates the solute composition changes during solidification in the equilibrium condition, on the assumption of complete solute mixing and diffusion in both liquid and solid phases.

The Scheil condition assumes no diffusion of solute in the solid and complete mixing of solute in the liquid. Redistribution in the Scheil conditions is shown in Figure 2.20 (Stanford *et al.* 2004). It is noteworthy to understand the solute redistribution during the solidification process as this will indicate the growth rate and morphology for dendrite growth in further modelling techniques.

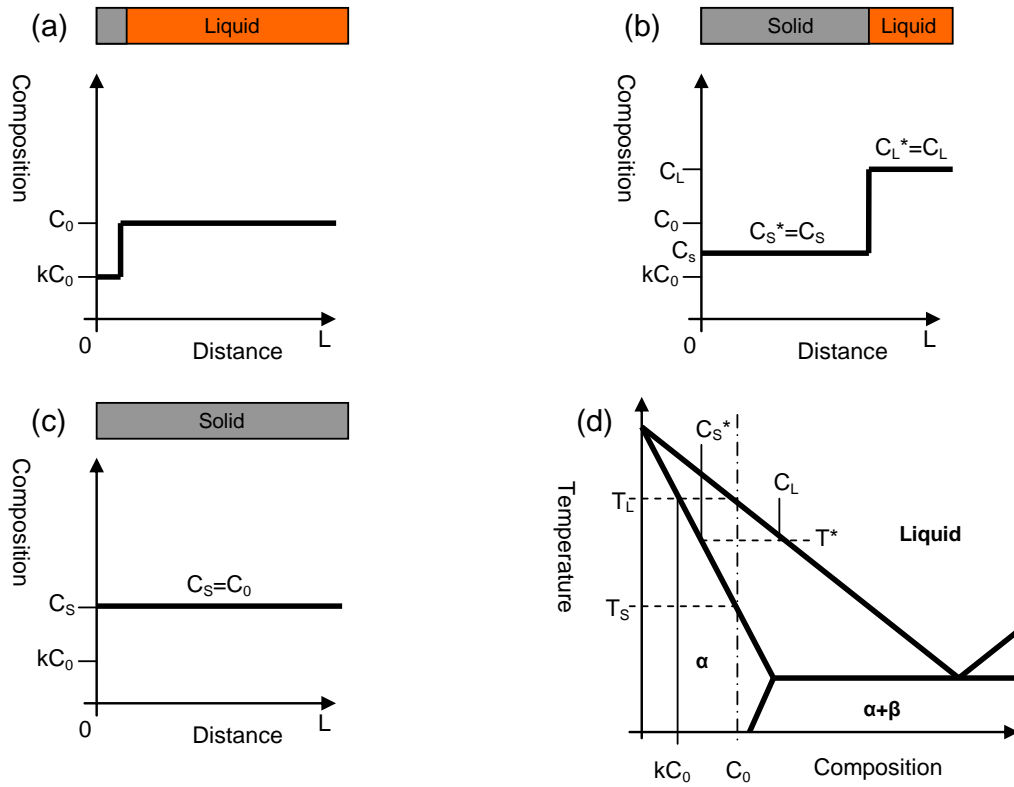


Figure 2.19 Solute redistribution during equilibrium solidification: (a) at the start of solidification, (b) at temperature  $T^*$ , (c) when solidification is complete, (d) the corresponding phase diagram (Flemings, 1974)

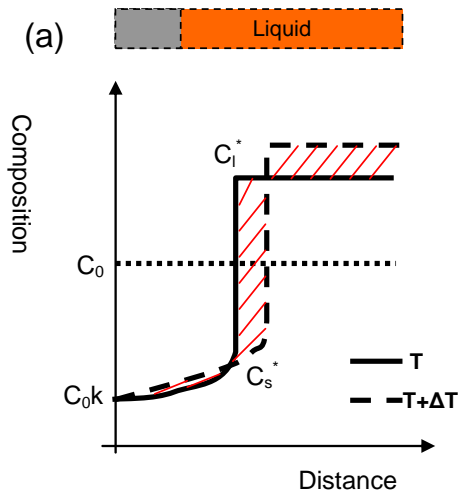


Figure 2.20 Solute redistribution under the Scheil condition during solidification (Stanford et al. 2004)

### 2.4.2.2 Undercooling

During solidification, local temperature at the solid/liquid (S/L) interface is different from the equilibrium melting temperature of the liquid and the difference is termed as the local undercooling,  $\Delta T$ . The growth rate and dendrite morphology during solidification highly depend on the local undercooling, which has contributions from constitutional undercooling  $\Delta T_C$ , curvature undercooling,  $\Delta T_r$ , thermal undercooling,  $\Delta T_t$  and kinetic undercooling,  $\Delta T_K$ ,

$$\Delta T = \Delta T_C + \Delta T_\gamma + \Delta T_t + \Delta T_K \quad (2.12)$$

Constitutional undercooling due to the solute partition and diffusion between solid and liquid is calculated according to:

$$\Delta T_S = m_l(C_\infty - C_L^*) \quad (2.13)$$

where  $C_\infty$  is bulk alloy composition and  $C_L^*$  is the alloy composition at the interface of the liquid and  $m_L$  is liquidus slope.

Curvature undercooling refers to the effect of excess energy of the formation of the S/L interface and is determined by:

$$\Delta T_r = K\Gamma \quad (2.14)$$

where  $\Gamma$  is Gibbs-Thomson coefficient and  $K$  is the average curvature at the S/L interface.  $K$  is expressed as follows for isotropic surface energies,

$$K = \frac{1}{r_1} + \frac{1}{r_2} \quad (2.15)$$

where  $r_1$  and  $r_2$  are the principal radii of curvature.

Thermal undercooling  $\Delta T_t$  is related to the release of latent heat and assumes particular significance in pure materials where constitutional undercooling is absent.

Kinetic undercooling  $\Delta T_K$  is associated with the driving force for atoms to transfer from solid to liquid. The effect of kinetic undercooling is always neglected for metals in terms of the roughness of the S/L interface on the microstructure scale (Chilton, 2002).

The constitutional, curvature and thermal undercoolings are illustrated in Figure 2.21 (Kurz and Fisher, 1984). The effect of solute distribution on undercooling will be investigated in Chapter 6 corresponding to different dendrite packing patterns.

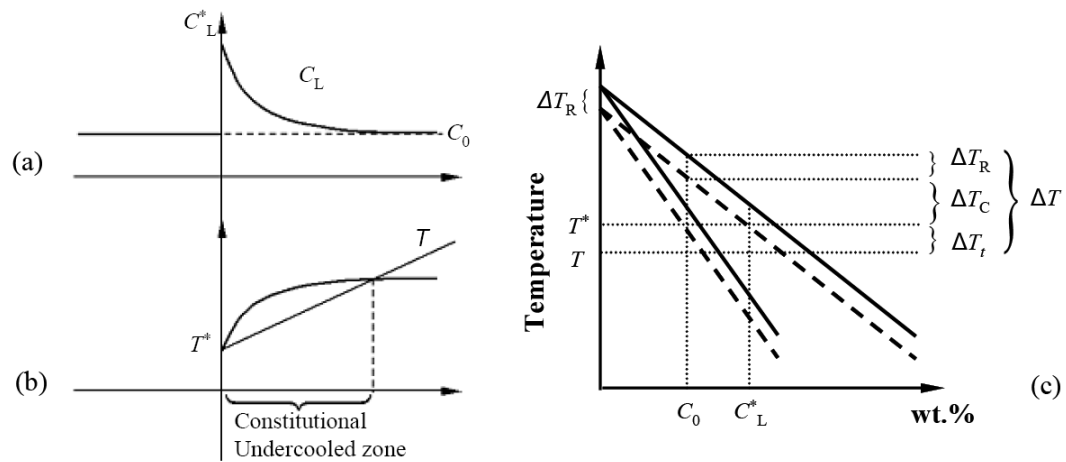


**Figure 2.21** (a) Solute distribution at the S/L interface; (b) constitutional undercooling in front of the S/L interface; and (c) effects of different undercoolings during solidification in a linearized binary phase diagram (Kurz and Fisher, 1984)

## 2.5 Modelling of Solidification Structures

With the advent of powerful computers, advanced numerical methods have been developed for the modelling of microstructure formation. This section starts with a review of analytical models of grain growth followed by numerical models including phase-field and cellular automaton methods.

### 2.5.1 Dendrite Growth Models

Modelling dendritic growth is made particularly difficult because the shape of the solid/liquid interface needs to be defined. In 1947, Ivantsov derived a mathematic solution to solve the solute transportation around the tip. Using Ivantsov's solution, Kurz, Giovanola and Trivedi (1986) proposed a theoretical model (the KGT model) to describe the growth of columnar dendrites. The dendrites are assumed to have an ideal parabolic shape and the supersaturation  $\Omega$  can be derived as a function of solutal Péclet number  $Pe$  following the equation:

$$\Omega = Iv(Pe) = Pe \cdot \exp(Pe) \int_{Pe}^{\infty} \frac{\exp(-u)}{u} du \quad (2.16)$$

where  $\Omega = (C_L - C_0) / [C_L(1 - k)]$  and  $Pe$  is defined as:

$$Pe = \frac{RV_{tip}}{2D_L} \quad (2.17)$$

where  $V_{tip}$  is tip velocity and  $R$  is tip radius. When thermal gradient  $G$  is assumed to be constant and its effect on the diffusion field around the tip is neglected,  $R$  can be given by:

$$R = 2\pi \sqrt{\frac{\Gamma}{mG_C \xi_C - G}} \quad (2.18)$$

where  $G_C$  is the solute gradient in the liquids at the tip and  $\xi_C$  is also a function of  $Pe$  which, at low growth rates, is close to unity.

In the KGT model, assuming kinetic undercooling is neglected, the total tip undercooling only takes account into constitutional undercooling and curvature undercooling, expressed as:

$$\Delta T_{\text{total}} = \Delta T_C + \Delta T_R = m_l(C_L - C_0) + \frac{2\Gamma}{R} = m_L C_0 \frac{(1-k)\Omega}{1-(1-k)\Omega} + \frac{2\Gamma}{R} \quad (2.19)$$

By substituting  $\Omega$  with  $R$  and  $V_{\text{tip}}$  according to Equations 2.16 and 2.17, an approximately polynomial function between total tip undercooling  $\Delta T_{\text{total}}$  and tip velocity  $V_{\text{tip}}$  is obtained:

$$V_{\text{tip}} = A_1 (\Delta T_{\text{total}})^2 + A_2 (\Delta T_{\text{total}})^3 \quad (2.20)$$

where  $A_1$  and  $A_2$  are constants related to material properties.

Hunt and co-workers developed an axisymmetric model of cellular and dendritic growth (Hunt and Lu, 1996). The Hunt model is capable of predicting cellular and primary dendrite spacings, tip undercoolings and the transition between cellular and dendritic structures.

In the Hunt model, the shape of cell/dendrite well behind the tip is given approximately following the Scheil condition because liquid in the cell/dendrite groove is nearly uniform perpendicular to the growth direction. The predicted dendrite tips have a parabolic shape, which validates the assumption made in the KGT model.

The total undercooling is contributed by constitutional undercooling and curvature undercooling with kinetic undercooling being neglected. The calculated constitutional undercooling can be fitted by a function of dimensionless variables:

$$\Delta T'_C = \left( \frac{G'}{V'_{\text{tip}}} \right)^c + a V'^b_{\text{tip}} + (1-a) V'^{1.2b}_{\text{tip}} \quad (2.21)$$

The dimensionless undercooling, dimensionless thermal gradient and dimensionless velocity are defined as,

$$\Delta T' = \Delta T k / [m C_0 (k-1)] \quad (2.22)$$

$$G' = G\Gamma / (m_l C_0)^2 \quad (2.23)$$

$$V' = V\Gamma / (D_L m_l C_0) \quad (2.24)$$

where a, b and c are coefficients related to partition efficient  $k$ .

When partition coefficient  $k$  is less than 1, Equation 2.21 approximates to:

$$\Delta T'_C = \frac{G'}{V'_{\text{tip}}} + V'_{\text{tip}}{}^{0.333} \quad (2.25)$$

And the numerical results of curvature undercooling can be expressed as:

$$\Delta T'_R = 0.41(V'_{\text{tip}} - G')^{0.51} \quad (2.26)$$

The above models have focused on defining the functional dependence of tip variables on the physical and transport properties of the material (*e.g.* radius and velocity). These models can only deal with dendrite tips but not the overall dendritic morphology. To overcome this limitation, more detailed numerical models have been developed. Among these models, Phase Field (PF) and cellular automaton (CA) models are widely used to simulate the dendrite growth which will be briefly summarized below.

## 2.5.2 Phase Field Models

Phase Field (PF) models have become popular in the field of structure evolution in solidification because of its capability of accurate and grid-independent simulations of alloy solidification on the scale of microstructure. Its chief advantage is to avoid the explicit interface tracking by the introduction of a phase field variable,  $\phi(x, y, t)$ , which takes on constant values in the bulk phases and varies smoothly but steeply in a diffuse interface region (Loginova *et al.* 2001). Warren and Boettinger (1995) were the first researchers to develop a Phase Field (PF) model to solve the solute diffusion equations during dendritic solidification of a binary alloy for isothermal solidification. More researches have been done to extend this model to account for coupled heat, solute

diffusion, and solidification with an applied temperature gradient and to study free dendritic growth (Boettinger et al. 2000; Boettinger *et al.* 2002; Ramirez and Beckermann, 2005). PF method has emerged as a powerful algorithm to simulate the evolution of S/L interface in both 2D and 3D. The technique is capable of reproducing most of the phenomena associated with microstructure formation (dendrite tip kinetics, preferred growth direction, coarsening). However, the major problem is that the interface width in phase field model has to be extremely small which limits the entire domain size and computation efficiency.

### 2.5.3 Cellular Automaton Models

Cellular Automata (CA) solidification models aim to produce complex physical phenomena with simple rules defined at a microstructure level (Rappaz *et al.* 2003). Every cell in CA model has the same rule for updating, based on the values in its neighbourhoods. Each time the rules are applied to the whole grid a new generation is created.

Combined with finite element solver for heat flow, Gandin and Rappaz (1997) developed a Cellular Automata Finite Element (CAFE) model to calculate the nucleation and growth of each individual grain during solidification. The envelop evolution of the growing grains is achieved using KGT model (Kurz *et al.* 1986) which connects growth velocity to tip undercooling. This model is used in this study to predict grain structure and orientations during solidification and more details about the model will be described in Chapter 3.

The CAFE model relates the grain growth rate with thermal uncooling using the KGT model and the microscopic solute interaction is not included. Therefore dendritic structure and solute segregation can not be solved in the CAFE model. To simulate the growth of dendrites controlled by diffusion, a model  $\mu$ MatIC was developed which combines a stochastic nucleation model and a modified decentred square/octahedron method to describe dendritic growth with a finite difference computation of solute diffusion. This model was first developed by Lee and co-workers

to predict porosity in shape cast aluminium alloys (Lee, 1994). To account for the crystallographic anisotropy of cubic metals, Wang *et al.* (2003) adopted the modified decentred squared/octahedron (in 2D/3D respectively) growth and cell ‘capture’ algorithm which was firstly developed by Gardin and Rappaz (1997). This model is used in this study to visualize the detailed dendrite structure, and to investigate the new grain formation and dendrite packing patterns on primary spacing during solidification. The details of the  $\mu$ MatIC model will be described in Chapter 3.

In summary, the need to achieve increased efficiency and performance, while reducing CO<sub>2</sub> emissions in aerospace propulsion and power generating gas turbines requires advanced single crystal Ni-based superalloys. Hence there is an impetus both for alloy development and for process optimisation for manufacturing turbines with increased efficiency and performance. However, the introduction of refractory elements in newer Ni-based superalloys has presented serious processing concerns due to solidification segregation. Therefore a better control of the solidification structure is required. Here a multiscale approach to numerical modelling will be used to study: (1) grain selection during investment casting of single-crystal turbine blades; (2) the formation of new grains ahead of advancing columnar dendrites; and (3) the influence of dendrite packing pattern (cuboidal or regular hexahedral) on primary spacing adjustment during directional solidification.

## Chapter 3 Model Description

Multi-scale modelling of solidification bridges length and time scales across many orders of magnitude and its use is growing at a rapid pace due to its power in predicting structures and properties of materials quantitatively. Figure 3.1 illustrates the multi-scale approach which spans 12 orders of magnitude of spatial scales and 19 orders of magnitude temporal scales.

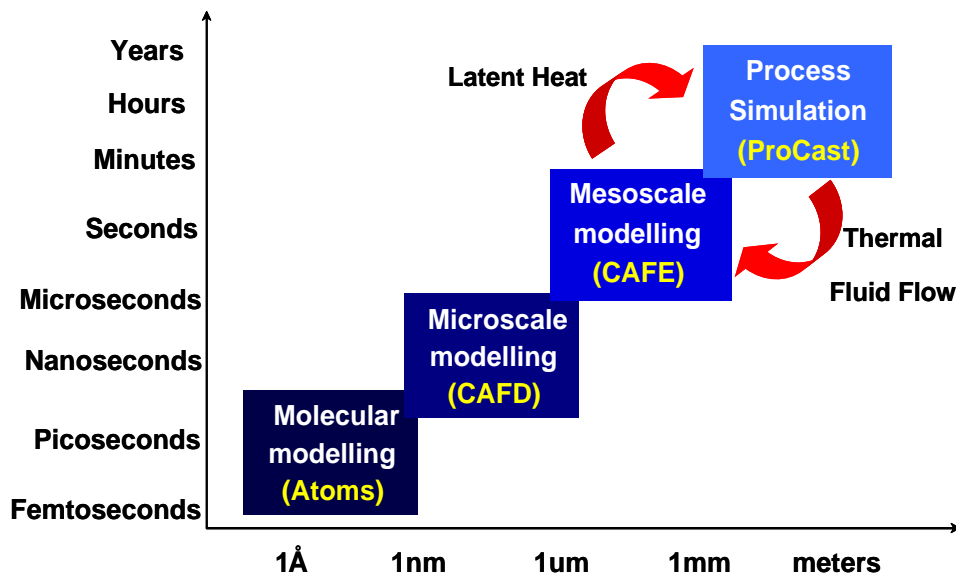


*Figure 3.1 Schematic illustration of multi-scale modelling*

On the molecular scale, quantum mechanics methods are required to describe the interactions between atoms and electrons. As one moves from the atomic scale towards the micro-scale, for example, phase field and cellular automaton techniques (CA) are used to simulate microstructure evolution and dendrite morphology in solidification processes. On the next larger scale, meso-scale, grain structure models, such as cellular automaton finite element (CAFE), become important to describe the effects of grain boundaries, orientations and ensembles of defects on materials performance. Finally, on the macro- or continuum- scale, the behaviour of materials can be predicted by environmental or loading factors such as applied stresses or temperature gradients (ProCAST).

In this study, a multi-scale approach spans from micro-scale where solidification structure can be described to macro-scale where processing conditions can be controlled. Modelling of solidification at the macroscopic scale will be implemented using a finite element (FE) casting model, ProCAST to obtain thermal and fluid flow profiles. The predicted thermal and flow data will then be used as input in the meso-scale model cellular automaton finite element (CAFE) to predict grain structures and orientations. On the micro-level, dendritic morphology and solutal distribution will be investigated using a micro-model  $\mu$ MatIC. The theories for these different models will be described in this chapter.

### 3.1 Macro-scale Model ProCAST

At the macroscopic level, attempts have been being made to study the mould filling, solidification, thermal balance of the mould and the development of stresses and strains. ProCAST\* has therefore been developed based upon the finite element method (FEM). It allows the modelling of heat transfer (*e.g.* heat flow), including radiation with view factors, fluid flow and stresses fully coupled with the thermal solution (Rappaz and Gardin, 1994; Rappaz and Gardin, 1999).

The macro-scale model ProCAST has several modules and the underlying physical equations associated with this study are summarized as follows:

Heat module:

$$\frac{\partial H}{\partial t} + \vec{u}_s \cdot \nabla H + \rho C_p (\vec{u} - \vec{u}_s) \cdot \nabla T - \nabla \cdot (K \nabla T) = S \quad (3.1)$$

---

\* ProCAST is registered by ESI Group, Paris.

The average heat conservation takes into account the phase change as well as the transport of the fluid and solid phase by assuming the transport velocity of the solid  $\bar{u}_s$  is divergence free. In Equation 3.1,  $\rho$  is the density,  $C_p$  is specific heat,  $K$  is the thermal conductivity,  $S$  is a given heat source term,  $T$  is the temperature,  $\bar{u}$  is the average velocity (a detailed definition will be given in the description of the Flow module) and  $H$  is volumetric enthalpy field which is assumed to be a function of  $T$  via the relationship:

$$H(T) = \int_0^T \rho C_p(\theta) d\theta + L(1 - f_s(T)) \quad (3.2)$$

where  $L$  is the latent heat of fusion and  $f_s$  is the volumetric fraction solid.

#### Radiation module:

During investment casting of high temperature alloys, radiation plays a important role in heat transfer and affects the solidification structure. Therefore, the radiation module is included in order to accurately treat radiant heat boundary conditions. In the ProCAST model, a set of  $N$  external faces belonging to a finite element mesh is considered. Assuming the environment between each surface is transparent and does not associate with the radiating change, the emitted flux  $q_i^{out}$  from each side  $i$  can be written as follows,

$$q_i^{out} = \varepsilon_i \sigma T_i^4 + (1 - \varepsilon_i) q_i^{in} \quad (3.3)$$

where the first term represents the radiant energy directly emitted by the side  $i$  and the second term characterises the reflected radiant energy from the side  $i$ . In Equation 3.3,  $\sigma = 5.67 \times 10^{-8} \text{ W}/(\text{m}^2 \text{K}^4)$  is the Stefan-Boltzmann constant,  $\varepsilon_i (<1)$  is the emissivity of the surface  $i$  and  $T_i$  is the corresponding temperature. The radiant energy received  $q_i^{in}$  can be calculated by,

$$q_i^{in} = \sum_{j=i}^N q_j^{out} F_{ij}, \quad i = 1 \dots N. \quad (3.4)$$

where  $F_{ij}$  is the view factor representing the fraction of the radiant energy leaving the surface  $j$ , which irradiates the surface  $i$ .

#### Flow module:

To calculate the fluid flow during solidification, a unit set of average equations are set to solve over the liquid, mushy and solid regions. Assuming density  $\rho$  is constant and uniform in the liquid and solid phases, the average velocity  $\vec{u}$  can be defined as:

$$\vec{u} = f_s \vec{u}_s + f_L \vec{u}_L \quad (3.5)$$

where  $\vec{u}_L$  and  $\vec{u}_s$  are the velocity fields of the liquid and solid respectively,  $f_L$  and  $f_s$  are the volumetric fractions of the liquid and solid respectively. Then the average velocity  $\vec{u}$  is given by:

$$\rho \left( \frac{\partial \vec{u}}{\partial t} + \frac{1}{f_L} (\nabla \vec{u}) \vec{u} \right) - 2\mu \nabla \cdot \dot{\varepsilon}(\vec{u}) + \frac{\mu}{K} f_L (\vec{u} - \vec{u}_s) + f_L \nabla p = f_L \vec{f} \quad (3.6)$$

$$\nabla \cdot \vec{u} = 0 \quad (3.7)$$

where  $\dot{\varepsilon}(\vec{u})$  is the strain rate tensor,  $p$  is the pressure field,  $\mu$  is the dynamic viscosity,  $K$  is the permeability of mushy zone and  $\vec{f}$  is the sum of any body force given by the user with the buoyancy term.

Based on the physical assumptions, the structure of the ProCAST model is illustrated in Figure 3.2 (ESI, 2006). During calculation, the geometry, in the form of a CAD model, is loaded into MeshCAST to generate a FEM mesh. Then the calculation is configured in the pre-processor which is linked to thermodynamic databases for the automatic determination of the material properties. Before the solvers are launched, a data

conditioner must run in advance. Finally, the results can be viewed and further analysed in the post-processor.

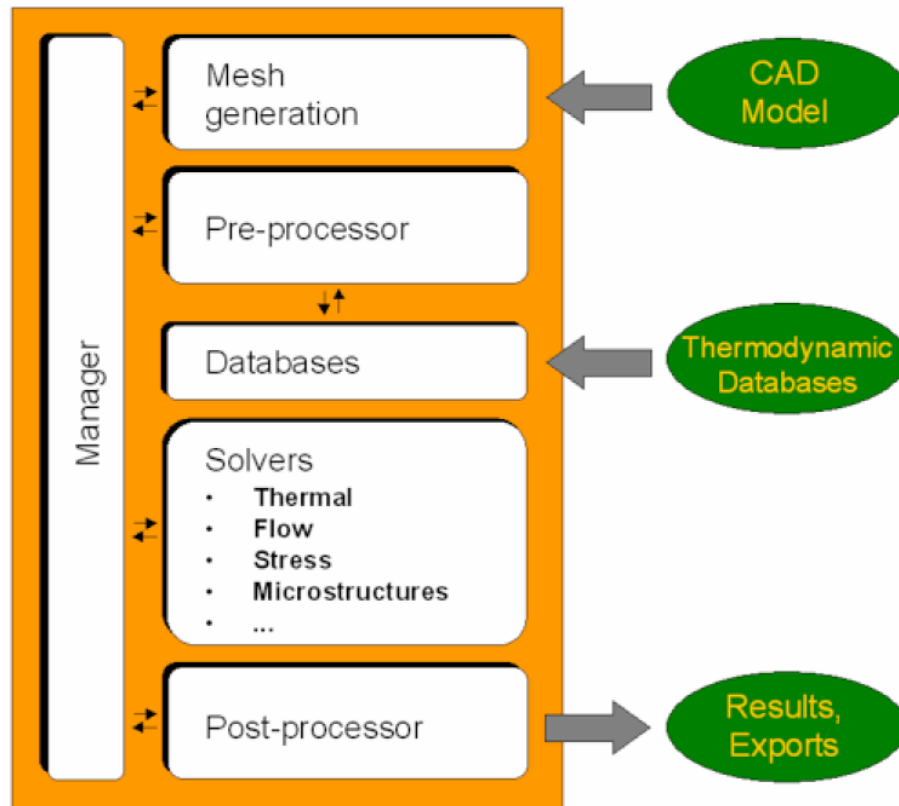


*Figure 3.2 Structure of macro-model ProCAST (ESI, 2006)*

### 3.2 Meso-scale Model CAFE

The finite element method (FEM) in the macro-scale model ProCAST allows one to calculate heat and mass transfer in complex geometries during solidification. However, the mushy region within which alloy solidification occurs is oversimplified when using the macro-scale model and hence details of microstructure formation are obscured (Rappaz and Gandin, 1993). Based upon a cellular automaton (CA) technique coupled with a finite element (FE) heat flow calculation (Rappaz and Gandin, 1994), the meso-scale model CAFE was developed to predict the grain structure with special consideration of the crystallographic anisotropy of grains and the growth kinetics of dendrite tips.

### 3.2.1 Cellular Automaton

Cellular Automaton (CA) solidification models aim to produce complex physical phenomena with simple rules defined at a microstructure level (Rappaz *et al.* 2003): (1) the simulated domain is divided into a grid of cells and each cell works as a small independent automaton; (2) each cell is characterized by different variables (*e.g.* temperature, crystallographic orientation) and state indices (*e.g.* liquid, solid); (3) the neighbourhood configuration is defined (*e.g.* 4-cell, 8-cell neighbourhood); (4) Time is divided into finite steps and the evolution of the given cell during one time step is defined by the transition rules according to the variables and/or states of the cell itself and its neighbouring cells.

Figure 3.3 (a) shows schematics for grain nucleation and growth from the mould wall and in the bulk liquid during solidification. In order to simulate grain formation for this situation, a time-stepping cellular automaton model was developed (Rappaz and Gandin, 1993). As illustrated in Figure 3.3 (b), a network of cells is laid out in terms of a regular lattice arrangement. Periodic boundary conditions are set for the left and right sides. Therefore, the cells on the right boundary have their right neighbours located on the left boundary and vice versa. At the beginning of solidification, each cell is assigned the same temperature which is above the liquidus of the alloy and a liquid status by setting a state index of zero. For the cells connected with the mould wall, a reference number is added for clarification. During simulation, the temperature at each time step is obtained from a heat-flow computation in a macro-scale finite element model. When the temperature becomes lower than the liquidus, solidification starts and the status of cells will be changed to growing cells, which is governed by two mechanisms: heterogeneous nucleation and solid growth.

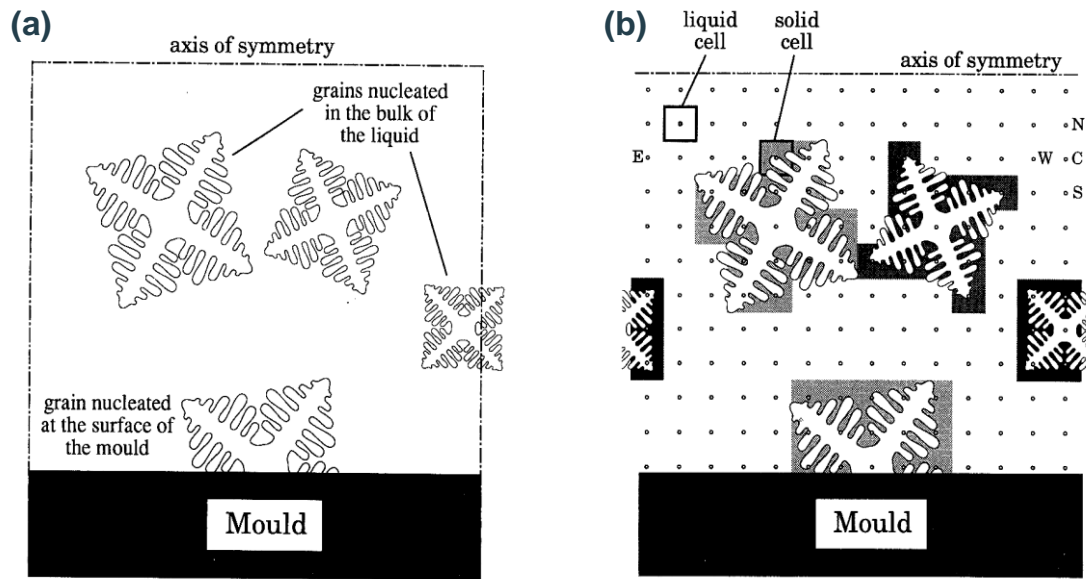


**Figure 3.3** (a) Schematics for a small solidifying volume element of uniform temperature within which nucleation and growth can occur from the mould and in the bulk; (b) corresponding cell schematics for the cellular automaton used to predict microstructure formation in the small solidifying specimen shown in (a) (Rappaz and Gandin, 1993)

To describe the heterogeneous nucleation, a continuous Gaussian nucleation distribution is used to relate the increase of grain density with the increase of the undercooling (Rappaz and Gandin, 1994),

$$n(\Delta T) = \frac{N_{max}}{\sqrt{2\pi}\Delta T_{\sigma}} \int_0^{\Delta T} \exp\left[-\frac{(\Delta T - \Delta T_{max})^2}{2(\Delta T_{\sigma})^2}\right] d(\Delta T) \quad (3.8)$$

where  $n(\Delta T)$  is the total number of nuclei in the bulk liquid at the undercooling  $\Delta T$ ,  $\Delta T_{max}$  is the mean nucleation undercooling;  $\Delta T_{\sigma}$  is the standard deviation of the distribution and  $N_{max}$  is the maximum nuclei density. Two such functions for heterogeneous nucleation at both the mould surface (unit of  $m^{-2}$ ) and in the bulk of the melt (unit of  $m^{-3}$ ) are shown in Figure 3.4. The characteristics of these two distributions (mean nucleation undercooling  $\Delta T_{max}$ , standard deviation  $\Delta T_{\sigma}$  and maximum nuclei density  $N_{max}$ ) can only be determined via experimental observations.

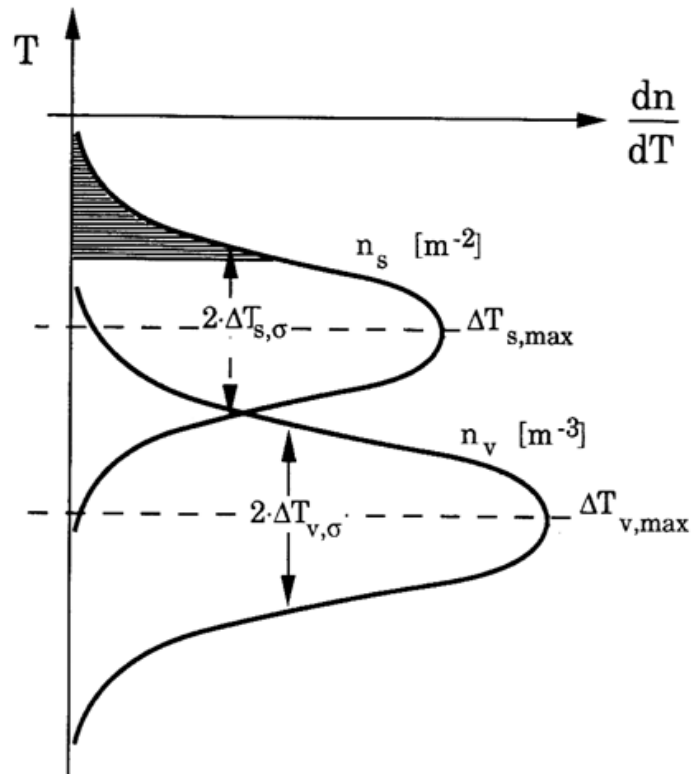


**Figure 3.4 Heterogeneous nucleation site distributions for nuclei formed at the mould wall and in the bulk of the melt (Rappaz and Gandin, 1993)**

As discussed in Chapter 2, solid growth is controlled by the dendrite tip undercooling which has contributions from constitutional undercooling  $\Delta T_C$ , curvature undercooling  $\Delta T_r$ , thermal undercooling  $\Delta T_t$  and kinetic undercooling  $\Delta T_K$ . The possibility of a kinetic undercooling for atom attachment is neglected, as metallic alloys exhibit low entropy of melting under normal solidification. In addition, the curvature undercooling is small compared with the thermal and solute contributions, especially when studying solidification on the meso-scale. Therefore, these two types of undercooling are neglected in this model. The solid growth rate  $v$  can be calculated using KGT model (Kurz *et al.* 1986),

$$v = a_0 + a_1 \Delta T_{ip} + a_2 \Delta T_{ip}^2 + a_3 \Delta T_{ip}^3 \quad (3.9)$$

where  $a_0, a_1, a_2$  and  $a_3$  are constants and  $\Delta T_{ip}$  is the tip undercooling.

To eliminate the microstructure dependence of the CA network and to incorporate the crystallographic anisotropy during solidification, a decentred square algorithm has been adapted (Gandin and Rappaz, 1997). This algorithm is capable of predicting the maximum growth envelope while accounting for the original mis-orientations of grains.

### 3.2.2 Coupling the FE and CA Models

The CAFE model couples the finite element method (FEM) on the macro-scale of the casting and a cellular automaton (CA) method on the meso-scale of the grain structure. Using an implicit enthalpy scheme (Rappaz and Gandin, 1994), temperature and enthalpy at each node of the FEM mesh are calculated. Then the calculated results are incorporated into the fine CA grid to predict the nucleation and growth of grains. Latent heat release during solidification can also be fed back to the macro-scale thermal calculation.

Figure 3.5 shows the solidification domain with a FE mesh and a CA grid.

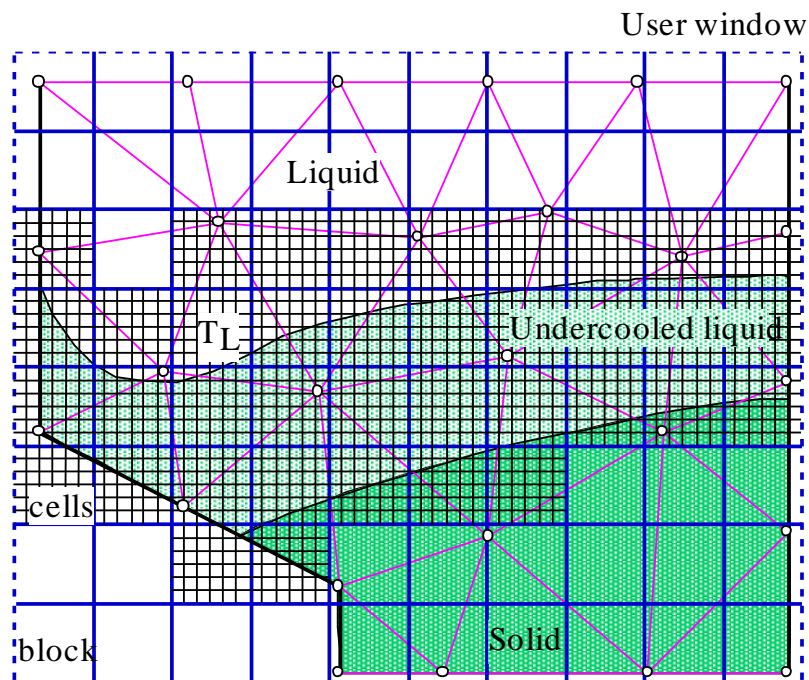


**Figure 3.5 Schematics of the solidification domain coupled with a FE mesh and a CA grid (Gandin et al. 1999)**

In order to improve the computational efficiency, two intermediate subdivisions are introduced: blocks (shown in solid blue grids) and user window (shown in dashed blue grids). The CA cells are defined dynamically only in the zones of interest, *i.e.* in the undercooled region near the liquidus. Therefore, the memory size necessary for the CA calculations is reduced to enable calculations with larger 3D geometries and save the computational time.

### 3.3 Micro-scale Model $\mu$ MatIC

ProCAST and CAFE are coupled to calculate the nucleation and growth of each individual grain during solidification and hence to predict the evolution of grain envelopes and orientations. However, the coupled model lacks consideration of solute diffusion and hence is not able to simulate the detailed dendritic structure and solute interactions within the dendritic network on the micro-scale.

In this study, a model  $\mu$ MatIC was used to simulate micro-scale features of solidification.  $\mu$ MatIC was developed by Lee and co-workers (Lee 1994; Wang *et al.* 2003), and combines a stochastic nucleation model and a modified decentred square/octahedron method to describe dendritic growth with a finite difference computation of solute diffusion. Compared with the prior analytical and numerical predictions, The  $\mu$ MatIC model is capable of reproducing the micro-scale dendritic structure such as primary and secondary dendrites, and in turn allows the interaction of solute fields both in front of and between the dendrites to be investigated (shown in Figure 3.6).

In the  $\mu$ MatIC model, both the nucleation model and solute diffusion model run on the same regular square grid and with the same time step. A schematic of the dendrite microstructure in 2D is shown in Figure 3.7 (Dong and Lee, 2005).

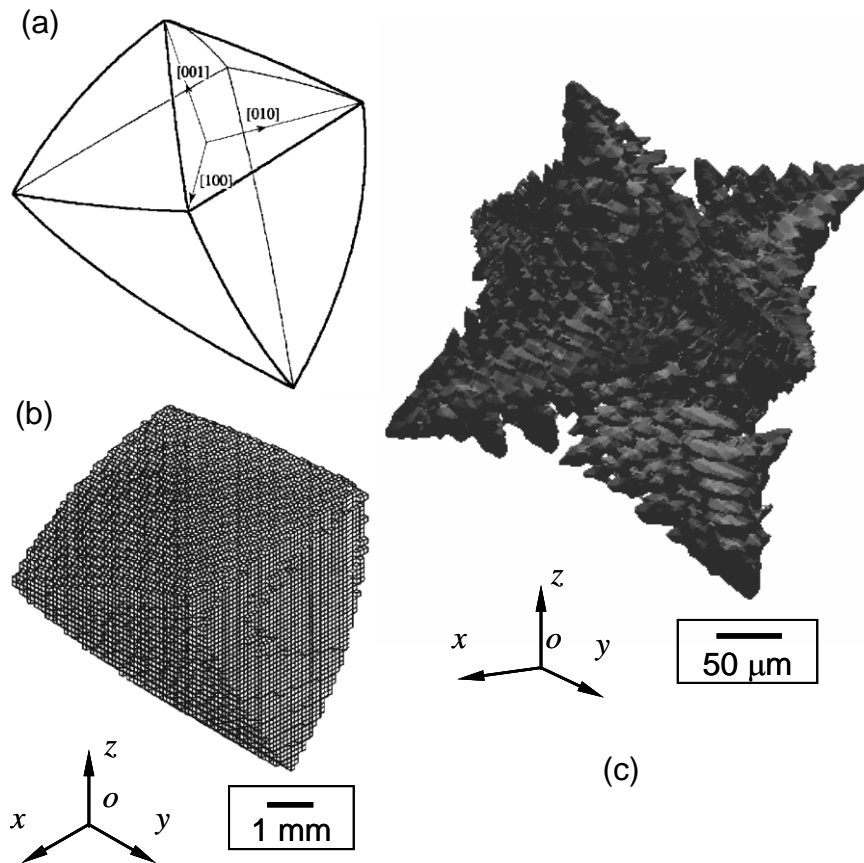


**Figure 3.6** 3D views of analytical (a) and numerical (b) predictions of a grain envelope without considering solute diffusion in meso-scale, and (c) simulated dendritic structure coupled with solute diffusion using  $\mu$ MatIC model in micro-scale (Wang et al. 2003)

Each spatial cell represents a small amount of material and can have three different states: (i) liquid; (ii) solid; and (iii) growing (i.e. a mixture of liquid and solid). The model begins with all cells in a liquid state, which may transform to a growing state by either nucleation or growth from its neighbouring cells. Meanwhile, a growing cell may also ‘melt’ back to the liquid state if the thermal condition is unfavourable for its growth. Solute is partitioned between liquid and solid phase in a growing cell. The extra solute will be pushed from solid to liquid and will accumulate in front of the solid/liquid interface if the partition coefficient is less than 1. At each time step, the solute diffusion through the liquid and solid will be calculated which will affect the level of undercooling due to the change of local liquidus temperature, and then in turn affect the

nucleation and growth processes. The assumptions, major equations, nucleation and growth mechanisms in the micro-scale  $\mu\text{MatIC}$  model are described below.

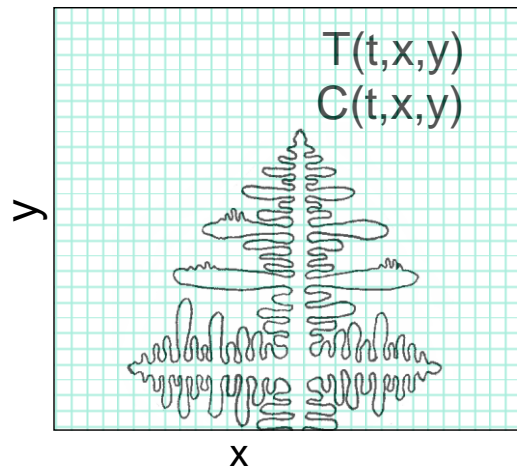


**Figure 3.7** A schematic of 2D dendritic microstructure in solute diffusion model (Dong and Lee, 2005)

### 3.3.1 Model Assumptions

Since the diffusivity of the heat is normally several orders higher than that of the solute, it is reasonable to assume that the heat diffusion has reached an equilibrium state in the thermal field at the dendritic tips. Instead of considering the heat diffusion equation and the release of latent heat, well-defined thermal conditions are applied to simulate directional solidification in this model, illustrated in Figure 3.8 (Yang, 2005).

The thermal field is determined by an initial temperature,  $T_{init}$ , thermal gradient,  $G$ , which is moving up at a constant velocity,  $V$ , giving a uniform cooling rate,  $V_C = G \cdot V$ . An initial temperature,  $T_{init}$ , is assigned to the cell with coordinates of  $(0, 0)$  in the domain prior to calculation (highlighted in grey at the bottom left hand side corner of the domain in Figure 3.8).

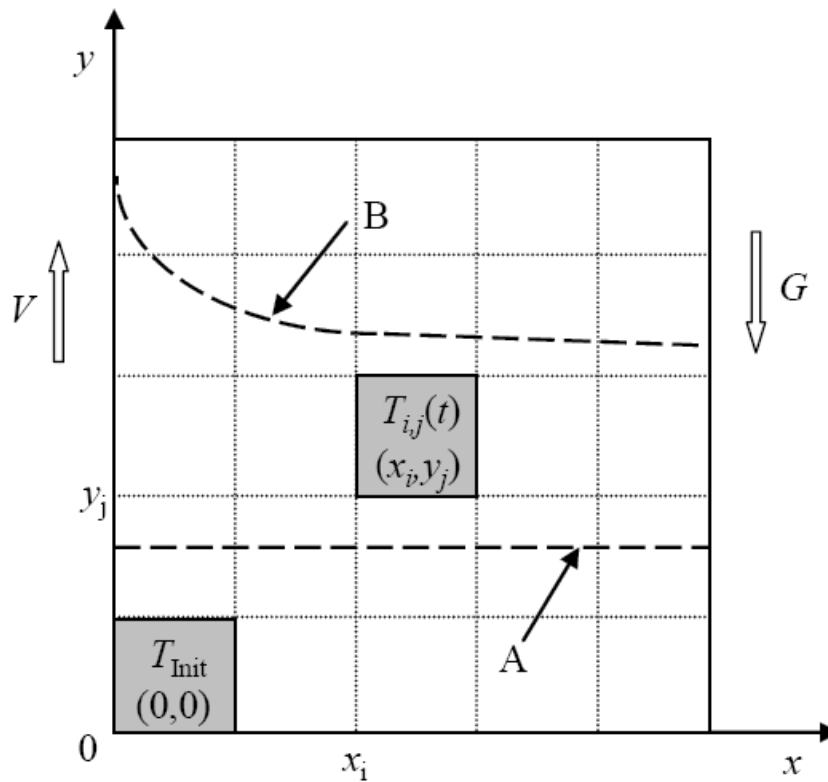


**Figure 3.8 Schematic illustration of the temperature field (Yang, 2005)**

In the case of flat isotherms (*e.g.* that marked with ‘A’ in Figure 3.8), the temperature in a cell  $(x_i, y_i)$  at time  $t$  is given by

$$T_{ij}(t) = T_{liq}^0 + G \cdot (y_j - V \cdot t) \quad (3.10)$$

Under certain circumstances, curved isotherms (*e.g.* that marked with ‘B’ in Figure 3.8) occur due to higher undercooling rates near the mould wall. This effect is taken into account by defining a function  $s(x)$ :

$$s(x) = a_1 x + a_2 x^2 \quad (3.11)$$

where  $a_1$  and  $a_2$  are constant coefficients, which can be defined as a function of time. Then the temperature of a cell  $(x_i, y_i)$  at time  $t$  is given as

$$T_{ij}(t) = T_{liq}^0 + G \cdot (y_j - V \cdot t - (a_1 x_i + a_2 x_i^2)) \quad (3.12)$$

The thermodynamic assumption in  $\mu$ MatIC model is based on a linearised binary phase diagram which has been discussed in Section 2.4.2.

Another simplification is made to improve the computational efficiency by assuming that diffusion coefficients in the liquid and solid phases,  $D_L$  and  $D_S$ , are constant and independent of both temperature and solute concentration. As mentioned before, the effect of kinetic undercooling on the equilibrium temperature and composition is assumed to be negligible which makes the model not applicable to rapid solidification processes or faceted phases.

### 3.3.2 Nucleation

There are two types of nucleation incorporated into the model: pre-fixed nucleation at specific sites and stochastic nucleation.

Pre-fixed nucleation is usually used for the simulation starting with special initial conditions, *e.g.* the nucleation at the bottom of the domain (mould surface), seeds packed in different patterns. Certain seeds are put into special cells with a certain level of undercooling before the simulation, and the states of these cells will be turned into ‘growing’ with a small amount of fraction solid in advance.

Different to the pre-fixed nucleation, stochastic nucleation is incorporated to set up nuclei randomly with specific threshold undercooling, representing the stochastic nature of the process. Similar to heterogeneous nucleation discussed in the meso-scale CAFE model, a continuous Gaussian nucleation distribution is used to relate the total number of nuclei in the bulk liquid with undercooling (Equation 3.8). Nucleation will occur in a cell only if the cell has a randomly distributed nucleus and the undercooling in the cell exceeds the predetermined critical nucleation undercooling. Meanwhile, a random crystallographic orientation  $\theta$  will be assigned to the nucleus.

Through either pre-determined or random nucleation, if a cell effectively transforms from the liquid to the ‘growing’ state, a grain number will then be associated with it and the fraction solid in it will be changed from zero to a small positive value. The nucleated grain could either melt back into liquid if the temperature in that cell increases well beyond liquidus later, or start to grow if the thermal condition is in favour of its growth.

### 3.3.3 Growth Mechanism

Growth of the nucleated grains in the micro-scale model  $\mu\text{MatIC}$  is controlled by solute diffusion and a modified decentred-square growth technique to capture the grain orientations during solidification. Diffusion controlled grain growth during solidification is illustrated in Figure 3.9 (Wang, 2003) where blue sections stand for the solid cells, orange ones stand for liquid cells and the one between is the growing cell.

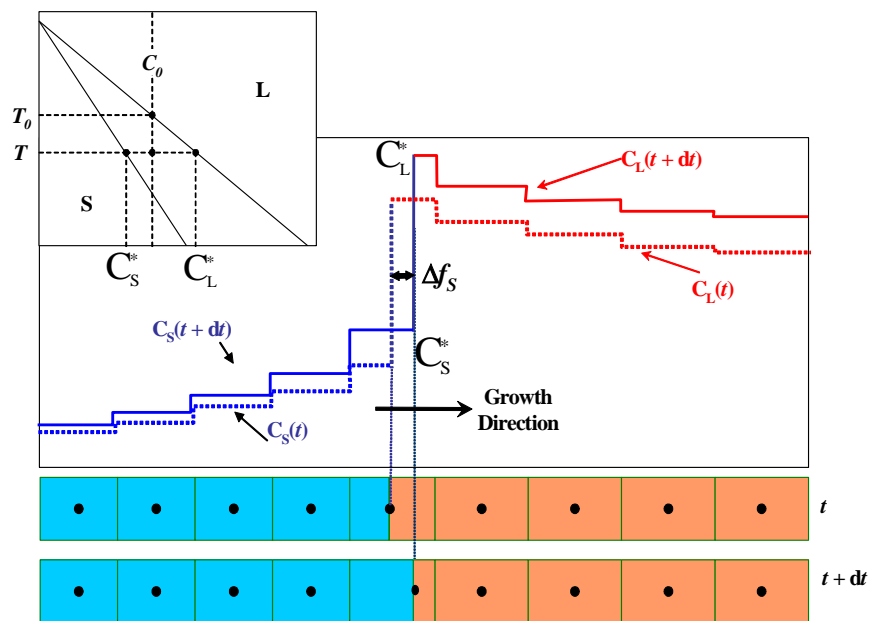


*Figure 3.9 A schematic diagram showing solute partitioning and solute distribution during solidification*

In a growing cell, equilibrium is assumed at the S/L interface, and solute partitioning is determined by:

$$C_S^* = kC_L^* \quad (3.13)$$

where  $C_S^*$  and  $C_L^*$  are the solute concentration in solid and liquid phases at the S/L interface respectively.

An equivalent concentration,  $C_E$ , in a growing cell, is defined as:

$$C_E = C_L(1-f_s) + C_S f_s = C_L[1-(1-k)f_s] \quad (3.14)$$

where  $f_s$  is the solid fraction,  $C_L$  and  $C_S$  are the average solute concentrations of the solid and liquid respectively. At time  $t$ , the diffusion of solute in the liquid and solid is given by the Fick's second law, and can be expressed in a general form:

$$\frac{\partial C_E}{\partial t} = \nabla \cdot (D_E \nabla C_L) \quad (3.15)$$

$D_E$  is an equivalent diffusion coefficient in a growing cell identified as

$$D_E = (1-f_s)D_L + f_s k D_S \quad (3.16)$$

where  $D_L$  and  $D_S$  are diffusion coefficients in liquid and solid respectively.

The solid fraction change  $df_s$  between the present time  $t$  (dashed line) and the next time step  $t+dt$  (solid line) in the growing cell is determined by the solute flux between neighbouring cells and the variation of concentration within that cell. It can be calculated using an explicit finite different (FD) scheme shown below,

$$\frac{\partial f_s}{\partial t} = \frac{1}{C_L(1-k)} \{-\nabla \cdot (D_E \nabla C_L) + [1-(1-k)f_s] \frac{\partial C_L}{\partial t}\} \quad (3.17)$$

The calculated fraction solid is then used to correlate growth of solid according to a modified 2D decentred square growth algorithm (Wang *et al.* 2003) with the consideration of solute diffusion during solidification (Figure 3.10). As shown in Figure

3.10 (a), a grain with orientation of  $\theta$  is nucleated in the central cell and growing in a square shape following the equation,

$$\Delta L = \Delta x \cdot \Delta f_s \quad (3.18)$$

where  $\Delta L$  is the increment of the half width of the square and  $\Delta f_s$  is the fraction solid change. When the growing solid in the central cell touches its four neighbouring cells, a new square is created with the same orientation as the original nucleus and overlaps the original square as shown in Figure 3.10 (b). The growth rate of the new squares is determined by the solute diffusion and local temperature. Using this algorithm, these misoriented solid squares progressively encroach on more cells and maintain the solid growth direction shown in Figure 3.10 (c).

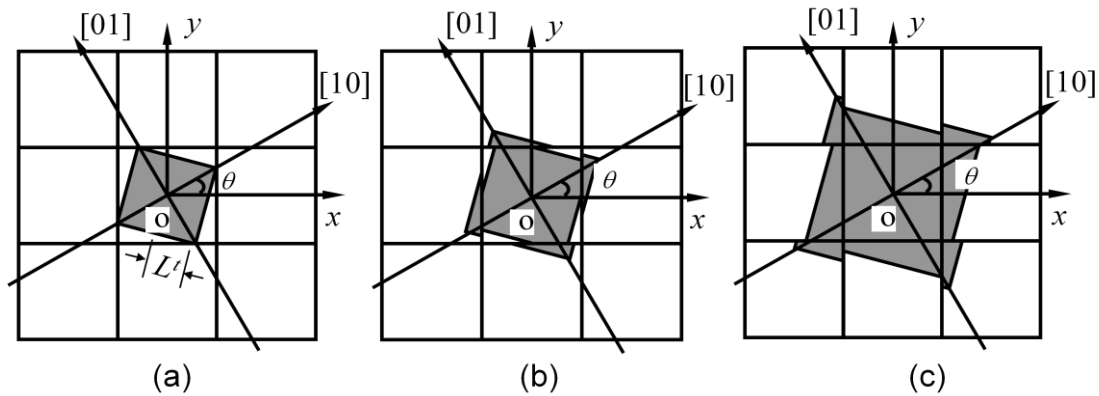


*Figure 3.10 Schematic diagram of modified 2D decentred square CA growth algorithm (Wang et al. 2003)*

### 3.4 Summary

The basic theories for macro-, meso- and micro-scale solidification models have been described. The multi-scale modelling approach is a useful tool for studying solidification phenomena across different orders of magnitude of scales. On the macroscopic scale of the process, a Finite Element casting model, ProCAST is implemented to obtain thermal and flow profiles. The predicted thermal and flow data

are then used as input in the meso-scale and micro-scale models to predict grain and dendrite structures during solidification.

## Chapter 4 Grain Selection during Investment Casting of Single Crystal Turbine Blades

A model involving coupling ProCAST at the macro-level and Cellular Automaton Finite Element (CAFE) at the meso-level is applied to simulate grain selection during investment casting of single crystal turbine blades. The macro-scale ProCAST model calculates the macroscopic heat transfer and fluid flow using a finite element solution for energy and momentum equations to determine the heat and momentum flow. Calculated thermal profiles are then input into the meso-scale CAFE model to predict grain structures and grain orientations in the grain selector. The effects of geometry and dimensions of the spiral selector on grain selection are investigated to improve the spiral efficiency. Experiments corresponding to different spiral geometries are carried out using a fully instrumented industrial directional casting furnace. Based on the simulation and experimental results, the mechanism of grain selection in the spiral selector is proposed to describe the grain selection during solidification.

### 4.1 Simulation of Grain Selection in SX Grain Selector

In the development of turbine blades, solidification structures have progressed from equiaxed to directionally solidified (DS) and then to single crystal (SX) through the introduction of novel processing techniques to increase the temperature capability of turbine blades (see Chapter 2). The DS process aligns crystals along the direction of constrained heat flow and therefore significantly decreases the number of grain boundaries in the direction perpendicular to the combined stress in use. As an extension to the DS casting process, a grain selector is incorporated to make a single crystal (SX) component, which can significantly improve the creep life. As illustrated in Figure 4.1, a grain selector consists of two parts: a starter block referring to competitive growth for the grain orientation optimization and a spiral selector facilitating dendrite branching to ensure that only one preferred grain eventually survives as the final seed for the SX component. The grain selection at the starter block was studied by Carter *et al.* (2000) to

predict the resultant grain size and grain texture. The purpose of this study is therefore to simulate and analyse the competitive growth and the grain selection in grain selector with emphasis on the shape of the spiral. In this section, thermal profiles predicted by macro-scale model ProCAST will be validated first. Then structure evolution in the grain selector during investment casting will be studied using the coupled ProCAST and CAFE model. To investigate the role of the spiral selector on grain selection, different spirals will be designed with quantitative description of the spiral geometry and dimensions and their effects on the efficiency of grain selection during casting will be discussed.

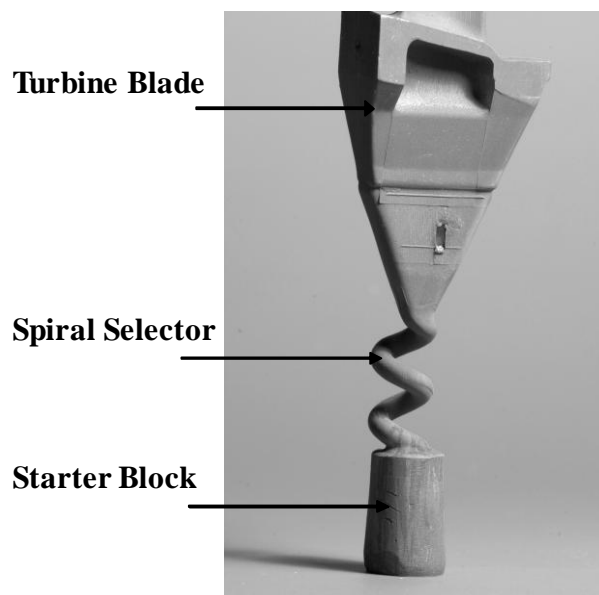


*Figure 4.1 Grain selector for the Trent 800 high-pressure turbine blade, showing the details of starter block and spiral grain selector (Reed, 2006)*

#### **4.1.1 Thermal Predictions in the Casting Process**

The thermal field plays a key role in casting. During directional solidification, the thermal profile in the grain selector was calculated using a VeriCAST model (Jennings 1996). The VeriCAST model was developed by Rolls-Royce Plc to represent a simple blade geometry containing a root, an airfoil and a platform without cores inside (shown in Figure 4.2) and has been validated using a fully instrumented industrial directional

casting furnace at Rolls-Royce Plc (Jennings, 1996). The VeriCAST model is now widely used to study the heat transfer during investment casting.

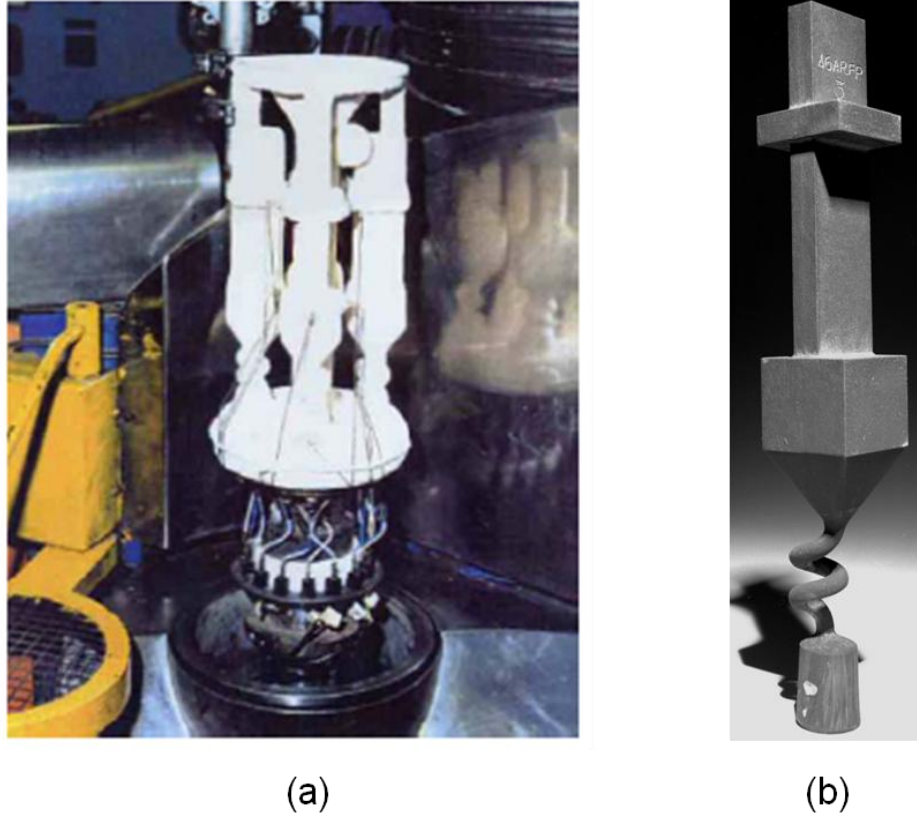


**Figure 4.2 (a) Instrumented mould of VeriCAST blade process modelling test piece on furnace and (b) VeriCAST blade casting after removal of the investment shell (Courtesy of Rolls-Royce plc.) (After Jennings, 1996)**

In this study, experimentally measured temperature / time boundary conditions and the 2<sup>nd</sup> generation single crystal superalloy CMSX4 with temperature dependent material properties were used. The initial temperature was set to 1500 °C. The shell was mounted on a water-cooled copper chill base and surface nucleation density of  $1 \times 10^8$  (nuclei/m<sup>2</sup>) was applied to generate random nucleation at the bottom of the starter block. After soaking the mould, the model assembly was withdrawn from the furnace at a pre-determined rate and grains grew from the generated seeds at the bottom of the starter block. In this study, a withdrawal velocity of  $0.06 \text{ mms}^{-1}$  is applied during solidification.

As an example, the calculated thermal profiles after 6s solidification for the investment casting furnace assembly and the blade are shown in Figure 4.3(a) and (b). An enlarged view of the calculated thermal profile at the grain selector is shown in Figure 4.3(c).

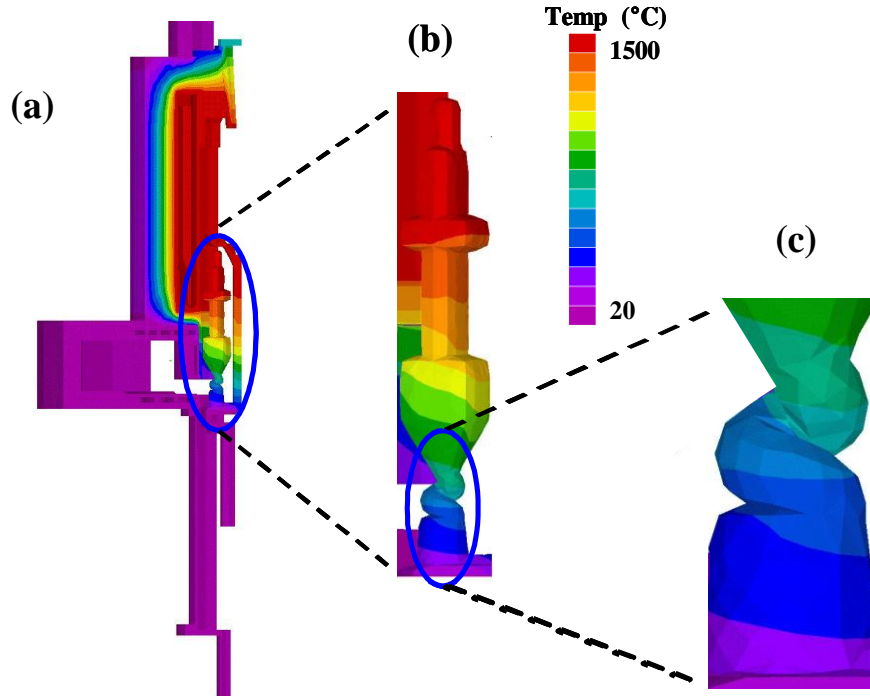


**Figure 4.3** Predicted three-dimensional thermal fields during casting of turbine blade; (a) investment furnace, (b) enlarged view of the casting blade, (c) enlarged view of the grain selector

Using the calculated thermal profiles as input, a meso-scale model, cellular automaton finite element (CAFE) is coupled with the VeriCAST model to predict the grain structure and orientations in the grain selector.

Figure 4.4 illustrates the predicted structure evolution and orientation selection in the grain selector. The left picture (Figure 4.4 (a)) is the predicted 3D grain structures in the grain selector including the starter block and the spiral selector. Different grains are characterized by different orientations shown in mixed colours for better separation.

Figure 4.4 (b1) - (e1) are the longitudinal sections at different heights from the chill to illustrate the grain structure evolution during solidification.

At the bottom, a large number of grains were nucleated with random orientations (Figure 4.4 (b1)). During competitive growth, the grains with orientations well aligned with the thermal gradient grew faster than their unfavourably oriented neighbours and unfavourably oriented grains were overgrown by well aligned grains, leading to a decrease in total grain number (Figure 4.4 (c1) - (d1)). At the height of 29 mm (Figure 4.4 (e1)), a couple of grains were primarily selected after the grain selection in the starter block and grew into the spiral, and then a single grain would eventually survive at a height corresponding to about a half of the pitch in the spiral.

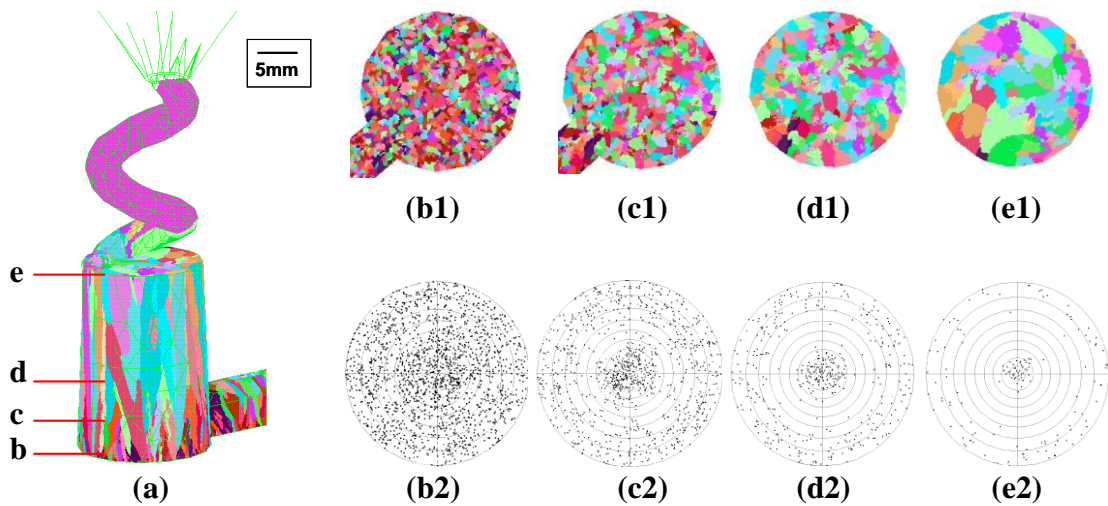


**Figure 4.4 (a) Predicted grain structure in the grain selector; cross section views and corresponding  $\langle 001 \rangle$  pole figures along vertical thermal gradient at the height from the chill of: (b) 2mm; (c) 5mm; (d) 10mm; (e) 29mm.**

Corresponding  $\langle 001 \rangle$  pole figures along the vertical thermal gradient at different heights from the chill plate are illustrated in Figure 4.4 (b2) - (e2). It is found that, at the bottom of the starter block, grains are randomly oriented and an  $\langle 001 \rangle$  texture develops within 10 mm from the chill (Figure 4.4 (d2)), which agrees with the experimental observations and predictions by Carter *et al.* (2000).

The selection of grain orientations is studied by investigating the average grain deviation in the selector during investment casting. Figure 4.5 (a) shows the average deviations of grain orientations at different heights from the chill. The dashed red line separates the starter block from the spiral selector as indicated in Figure 4.5 (b). Grain deviation is defined as the angle between the primary  $\langle 001 \rangle$  crystallographic direction of the grain and the vertical axis of thermal gradient shown in Figure 4.5 (c).

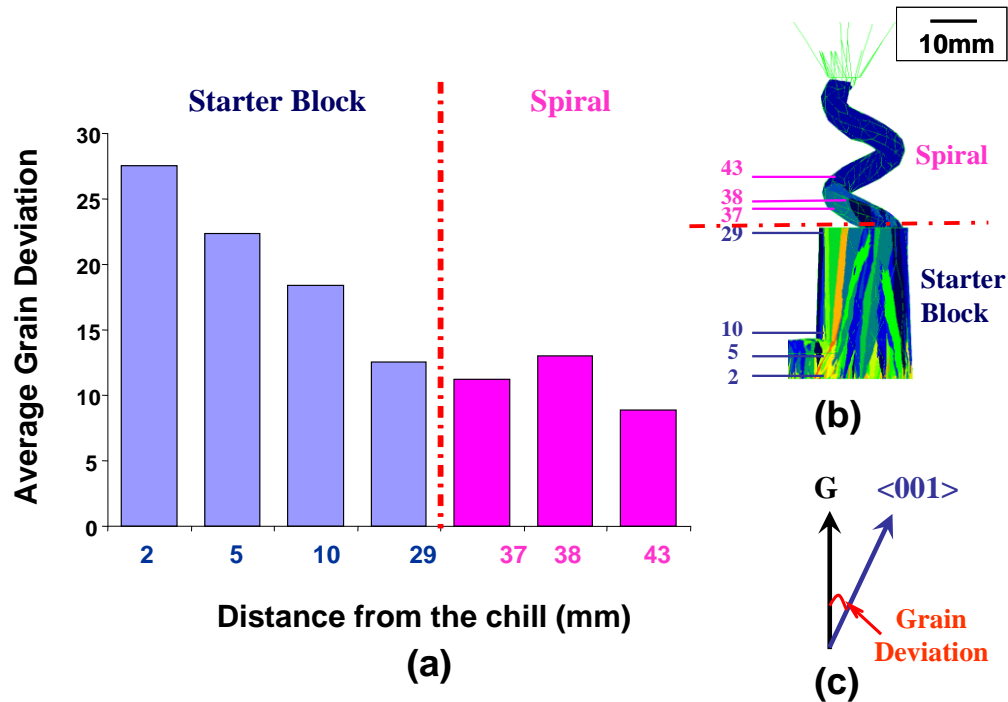


**Figure 4.5 (a) Average deviations of grain orientations at different heights from the chill; (b) grain selector illustrating the corresponding heights; (c) schematic definition of grain deviation**

It is worthy of note that, in the starter block, the average grain deviation is decreased with the rise of the distance from the chill and the grain orientation is controlled to within  $15^\circ$  by the top of the starter block. It is clear that the starter block is effective in the selection of grain orientations and the average grain orientation is determined by the height of the starter block. However, in the spiral selector, the average grain deviation is not optimized because some large angle grains may overgrow the small angle grains leading to an increase in the average grain deviation. Therefore, to find the physical

processes occurring in the spiral selector and to investigate the optimum dimensions and geometry of the spiral selector on the grain selection, spirals with different geometries are designed in the following section.

#### 4.1.2 Quantitative Description of Spiral Size and Geometry

With emphasis on the role of spiral selector in the grain selection, the height of the starter block was decreased to 1 mm to enable more grains to grow into the spiral. As shown in Figure 4.6, four key parameters are required to describe the geometry of the spiral: wax wire diameter ( $d_w$ ), spiral diameter ( $d_s$ ), take-off angle ( $\theta$ ) and pitch length ( $L_P$ ). The spiral take-off angle ( $\theta$ ) is defined as the angle between the spiral centre line and the horizontal direction, as schematically shown in Figure 4.6 (b).

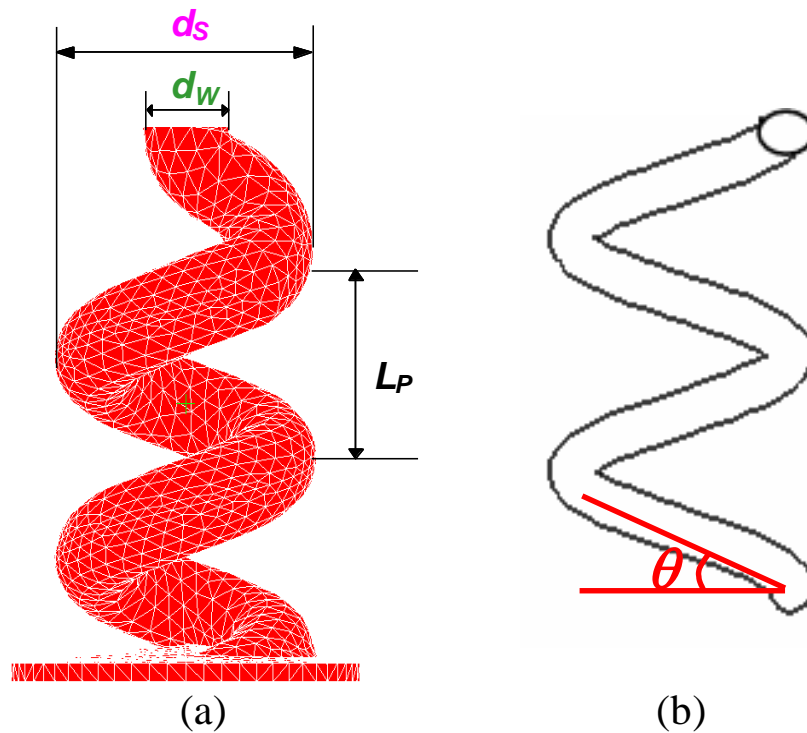


**Figure 4.6 (a) Spiral geometry defined in this study and (b) 2D schematic showing the definition of spiral take-off angle**

Only three of these parameters are independent, and the fourth can be deduced from the other three, for example, the pitch length is equal to:

$$L_p = 2(d_s - d_w) \tan \theta \quad (4.1)$$

Therefore, in this study, three parameters are verified: wax wire diameter ( $d_w$ ), spiral diameter ( $d_s$ ) and take-off angle ( $\theta$ ) to systematically investigate the effect of spiral shape on the grain selection. The different designs of the spiral used in this study are summarised in Table 4-1, which includes 18 cases divided into 3 groups.

**Table 4-1 Spiral geometry used in this study**

Group I: Wax Wire Diameter ( $d_w$ )

case	1	2	3	4	5	6	7
$d_w$ (mm)	2	3	4	5	6	7	8
$d_s$ (mm)	12	13	14	15	16	17	18
$\theta$ ( $^\circ$ )	28						

Group II: Spiral Diameter ( $d_s$ )

case	8	9	10
$d_w$ (mm)	5		
$d_s$ (mm)	13	15	17
$\theta$ ( $^\circ$ )	33	28	24

Group III: Take-off Angle ( $\theta$ )

case	11	12	13	15	15	16	17	18
$d_w$ (mm)	5							
$d_s$ (mm)	15							
$\theta$ ( $^\circ$ )	20	25	28	29	35	40	50	70

### 4.1.3 The Effect of Spiral Geometry on Grain Selection

It is of interest to investigate the efficiency of the spiral selector on the grain selection process with respect to different spiral geometries. To achieve this, the same thermal history was applied for all the cases shown in Table 4-1. Every single case in the spiral design was simulated 5 times to take into account the effect of the random nature of the

nucleation. In this section, the grain structure evolution and competitive growth in a spiral selector with the designed geometry will be visualised first to investigate the role of the spiral in grain selection for SX turbine blade. Then the measures for determining spiral efficiency will be described. Finally, the effects of wax wire diameter ( $d_w$ ), spiral diameter ( $d_s$ ) and take-off angle ( $\theta$ ) on the grain selection will be discussed respectively.

#### 4.1.3.1 Grain Selection in Spiral Selector

As an example, Figure 4.7 shows the grain selection in the spiral representing Case 4 in Table 4-1. The predicted 3D grain structure of the spiral is shown in Figure 4.7 (a). Grains with different orientations are shown using a linear colour map to indicate their orientations, from  $0^\circ$  in black to  $54^\circ$  in red. To better illustrate the grain selection inside of the spiral, cross sections at different heights are analysed. Figures 4.8 (b1)-(f1) present the grain structure evolution at different heights. The corresponding  $\langle 001 \rangle$  pole figures in Figures 4.8 (b2)-(f2) along the direction of heat flux and the grain deviation distributions in Figures 4.8 (b3)-(f3) clearly illustrate how the grain orientations are selected in the spiral during directional solidification. Average grain deviation is also plotted in Figures 4.8 (b3)-(f3) indicated by the dashed red line to investigate the effect of spiral on grain orientation selection.

At the bottom of the starter block (b), there were a large number of grains (Figure 4.8 (b1)) generated from the seeds with random orientations (Figure 4.8 (b2), (b3)). At the bottom of the spiral (c), grains were firstly selected within 1mm starter block, so the grain size became large and grain number was decreased (Figure 4.8 (c1)). Although the 1 mm length of starter block was too short to produce the  $\langle 001 \rangle$  texture, the grain orientations had been slightly optimized (Figure 4.8 (c2)) and the average grain deviation was decreased from  $31.9^\circ$  at the bottom of the starter block to  $19.8^\circ$  at the bottom of the spiral (Figure 4.8 (c3)). This agrees with the discussion above that the starter block is effective in selecting grain orientations and the height of the starter block is critical for the average grain deviation.

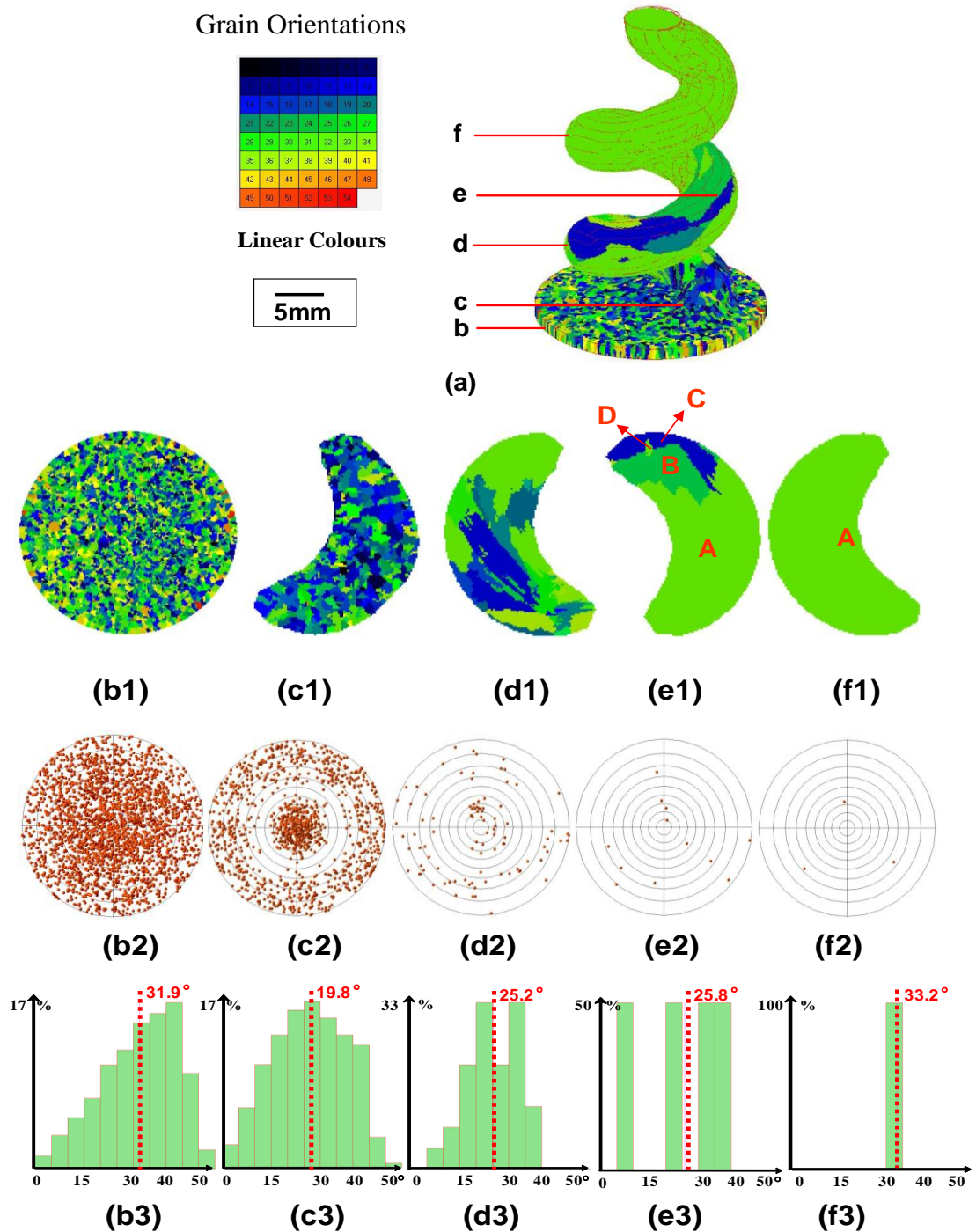


*Figure 4.7 (a) Predicted grain structure in the spiral selector, the grain structures evolution (b1) – (f1), corresponding  $\langle 001 \rangle$  pole figures along the direction of heat flux (b2) – (f2) and the grain deviation distributions (b3) – (f3) for the cross sections at the height of: (b) 0.1mm; (c) 1.1mm; (d) 6.25; (e) 11.5mm; (f) 16.75mm from the chill*

When grains grew into the spiral, the grain selection became more severe because of the smaller space in the cross section and twisted shape in the spiral. As shown in Figure 4.8 (d1), at the height of half pitch, the grain number was dramatically decreased. However, the points in the pole figure (Figure 4.8 (d2)) were still randomly distributed based on the orientations selected from the base and the grain orientation was not optimised in the spiral. It is found that some high angle grains (shown in green colour) can overgrow the smaller angle grains (shown in blue colour) during the grain selection, leading to an increase in the average grain deviation ( $25.2^\circ$  compared with  $19.8^\circ$  at the bottom of the spiral). As shown in Figure 4.8 (d3), grains with the grain deviation below  $5^\circ$  were overgrown by the other grains with larger grain deviations. This indicates that the spiral can offer an opportunity for the mis-orientated grains to overgrow the well-oriented grains due to the geometrical limitation (blocking), which is not likely to happen in a thermal controlled situation such as in a starter block. At the height of one pitch (e), there were only four grains that survived after severe competition in the spiral. From the distribution of the grain deviations (Figure 4.8 (e3)), the number of grains with deviations of  $10^\circ$ - $20^\circ$  and  $25^\circ$ - $30^\circ$  had appreciably decreased rather than the grains with high deviations and the average deviation of the grain orientation becomes  $25.8^\circ$ , slightly higher than the previous stage. This proves that the overgrowth mechanism due to the constrained thermal profile in the spiral has no direct effect on the selection of the grain orientations. Therefore, the spiral does not play a role in the selection of grain orientations. At the height of one and a half pitch (position f in Figure 4.8 (a)), the final SX grain was selected as shown in Figure 4.8 (f1). The grain deviation for the final SX grain is  $33.2^\circ$ , which overgrew the grains with either smaller or bigger grain deviations during solidification.

The above observation and analysis reveal that the spiral grain selector can quickly but randomly select one grain with no optimisation on the grain orientations. To further prove this and also to optimise dimensions and geometry of the spiral selector, the effects of spiral geometry on spiral efficiency will be discussed in the following sections.

### 4.1.3.2 Measures of Spiral Efficiency

To quantitatively investigate the effect of spiral sizes and geometry on the spiral efficiency, several measures are defined in this study. The first one is the required height for the SX structure to occur as shown in Figure 4.8. This height can affect the defect formation during solidification and the corresponding casting time. Also, with a larger required height, the ability in selecting single crystal will be reduced which will lead to an increase in the confidence limit (error bar) during application.

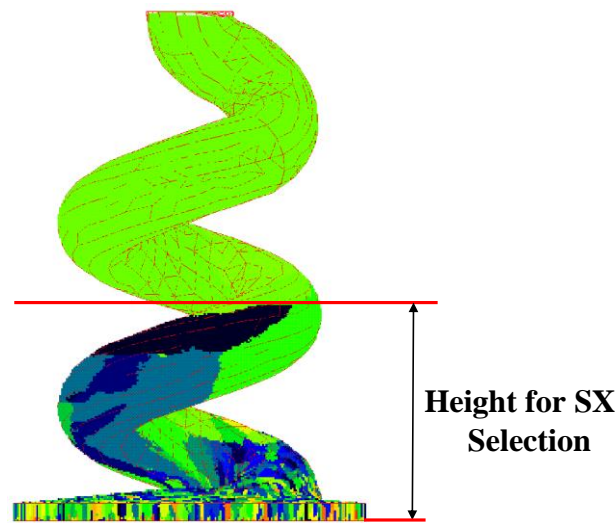


**Figure 4.8** Schematic diagram showing the required height for a SX structure to occur in the spiral

Corresponding to the required height, the required volume for the SX structure to occur is the second measure of the spiral efficiency. The required volume for the SX structure to occur can be used as a measure for the required alloy and therefore can affect the alloy cost. The required spiral volume for SX structure to occur can be calculated using the equation:

$$V = \frac{1}{4} \pi d_w^2 L_s = \frac{1}{4} \pi d_w^2 N \sqrt{\pi^2 d_c^2 + L_p^2} = \frac{1}{4} \pi d_w^2 N \sqrt{\pi^2 (d_s - d_w)^2 + L_p^2} \quad (4.2)$$

where  $L_S$  is the length of the spiral for the SX structure to occur,  $d_C$  is the diameter of the spiral centre which is equal to spiral diameter ( $d_S$ ) minus the wax wire diameter ( $d_W$ ),  $N$  is the number of turns for the SX selection.

The third measure for spiral efficiency is SX orientation, the grain orientation of the final single grain which will grow into the SX turbine blade. SX turbine blades are often employed in a condition that requires a particular angle between the  $\langle 001 \rangle$  grain orientation and the axis of the blade to maintain best performance along the direction of applied stresses in terms of various applications. Therefore, control of the final SX orientation becomes decisive for the final properties of the SX turbine blade. In this study, these three measures will be used to evaluate the spiral efficiency in terms of different spiral designs.

#### 4.1.3.3 Effect of Wax Wire Diameter

According to the defined measures for spiral efficiency above, the effect of wax wire diameter ( $d_W$ ) on the grain selection in spiral selector is investigated. In this study, the wax wire diameter ( $d_W$ ) is varied from 2 mm to 8 mm and the corresponding grain structures in the spiral selector are shown in Figure 4.9.

Figure 4.10 illustrate the effect of wax wire diameter ( $d_W$ ) on the required height for SX selection in spiral grain selector. Due to the stochastic nature of the nucleation event, every single case is repeated for five times shown in black points and the red curve shows the average value. However, the number of points shown in the figure is less than the total number of simulations. This is because: (1) some simulations failed to select SX structure after the designed length and hence there were no points shown for these simulations; (2) Some predicted results were of the same value which made the points overlap.

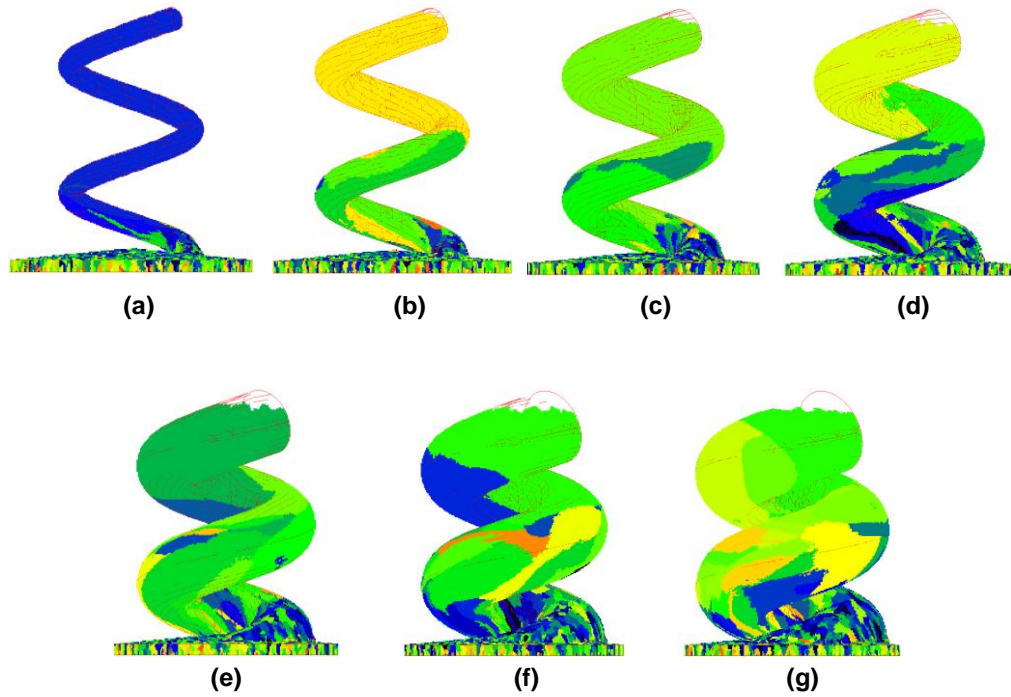


Figure 4.9 Grain structure in the spiral selector with wax wire diameter ( $d_w$ ) of : (a) 2mm; (b) 3mm; (c) 4mm; (d) 5mm; (e) 6mm; (f) 7mm; (g) 8mm

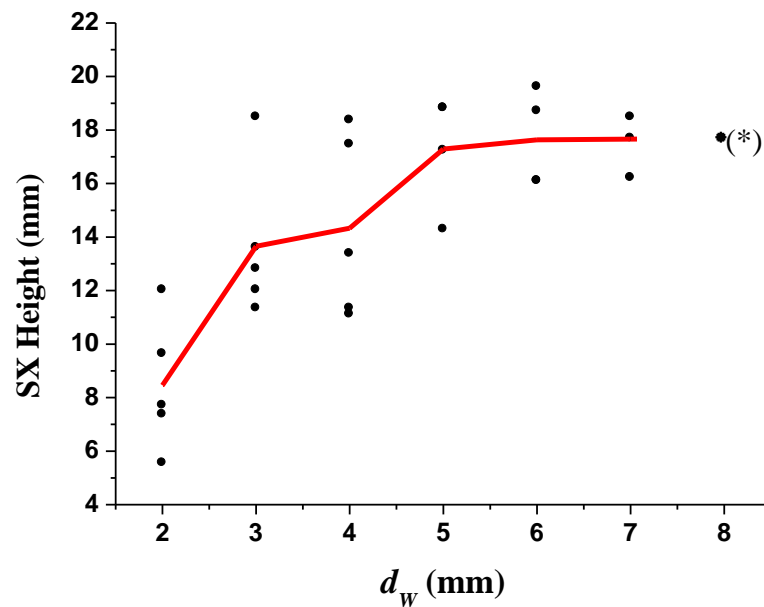
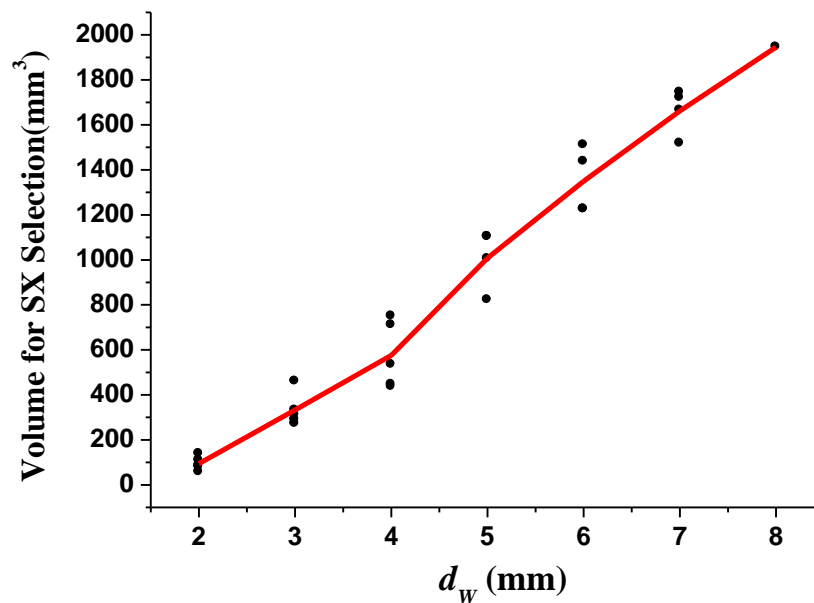


Figure 4.10 Effect of wax wire diameter ( $d_w$ ) on the required height for SX selection in the spiral grain selector (\*5 trials, 4 of them failed in selecting one grain)

As shown in Figure 4.10, the required height for SX selection increases with the rise of wax wire diameter ( $d_w$ ). This may be because with a smaller wax wire diameter ( $d_w$ ), the space in the spiral is small (shown in Figure 4.9) which makes the grain selection more severe and enables fewer grains to survive. When the wax wire diameter ( $d_w$ ) is larger than 5 mm, 20% of the simulations failed to successfully select SX after the length of two pitches in the spiral. When the wax wire diameter ( $d_w$ ) is increased to 8 mm, 80% of the simulations failed. Since the increase of the spiral height will directly prolong the casting time and promote defect formation, wax wire diameter larger than 5 mm will lead to a reduction of the yield rate in SX casting.

The required volumes for SX selection in the spiral for different wax wire diameters ( $d_w$ ) are shown in Figure 4.11.



**Figure 4.11** Effect of wax wire diameter ( $d_w$ ) on the required volume for SX selection in spiral grain selector

As illustrated in the figure, the required volume is increased by 20 times when the spiral thickness is increased from 2 mm to 8 mm, which means that smaller wax wire diameter can dramatically improve the spiral efficiency. This is because as described in Equation

4.2, the required volume is proportional to the square of the wax wire diameter ( $d_w$ ) since the diameter of the spiral centre ( $d_c$ ) is fixed. This implies that the wax wire diameter ( $d_w$ ) needs to be reduced to a small value in order to save alloy cost. However, if the wax wire diameter ( $d_w$ ) is too small, the spiral wax pattern might not have enough strength to support the whole weight of the blade wax during ceramic coating, and in turn cause fracture of the wax pattern and reduce the yield rate for the industrial application. Meanwhile, a wax wire diameter ( $d_w$ ) which is too small will be difficult to control during production. Considering both the spiral efficiency and the yield rate for application, wax wire diameters of 3 to 5 mm are often used in casting foundaries.

Figure 4.12 shows the final SX orientations for different wax wire diameters ( $d_w$ ) in spiral grain selectors.

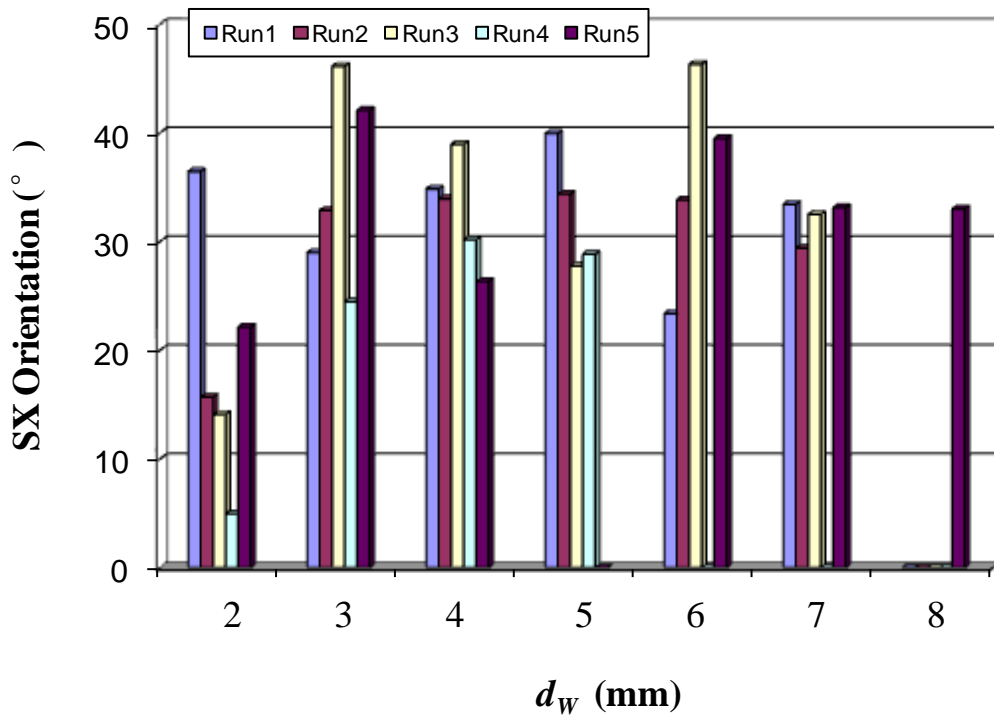


**Figure 4.12** Effect of wax wire diameter ( $d_w$ ) on the final SX orientation in spiral grain selector

Each individual case is repeated 5 times, indicated by different colours. For the simulations which the single crystal have not been successfully selected after the length

of two pitches in the spiral, no results will be displayed. As shown in Figure 4.12, the predicted results are randomly distributed in the figure. There is no consistent range for each case and no apparent correlation is found between the final SX orientation and wax wire diameter ( $d_w$ ), which confirms our speculation that the spiral plays no role in optimisation of the grain orientation selection.

#### 4.1.3.4 Effect of Spiral Diameter

To investigate the effect of spiral diameter ( $d_s$ ) on spiral efficiency, spiral selectors with spiral diameter ( $d_s$ ) from 13 mm to 17 mm are compared. In this study, the pitch length of the spiral ( $L_p$ ) is fixed and spiral take-off angle ( $\theta$ ) is calculated using Equation 4.1 as listed in Table 4-1. Figure 4.13 shows the grain structure in the spiral selector according to different spiral diameters. There are only three designs in this section because the range of spiral diameter ( $d_s$ ) is limited by the spiral geometry. The difficulty in making the spiral selector limits the increase of spiral diameter ( $d_s$ ). Therefore, 17 mm is chosen as the maximum diameter.

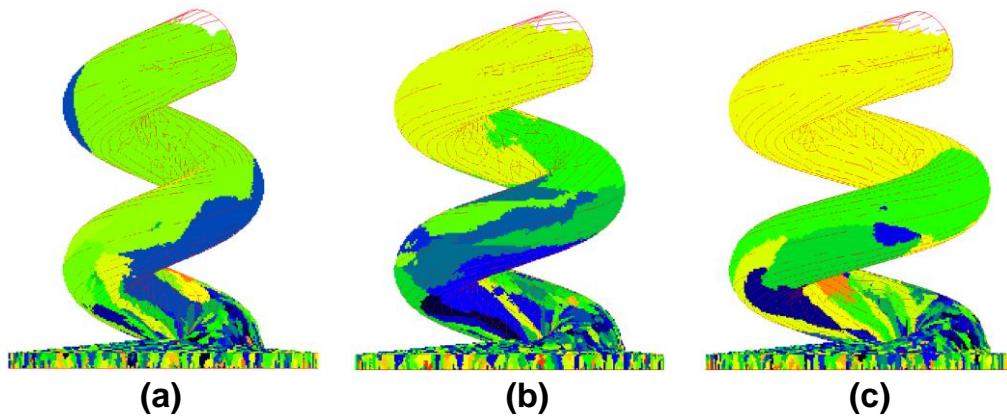


**Figure 4.13** Grain structure in the spiral selector with the spiral diameter ( $d_s$ ) of: (a) 13mm; (b) 15mm; (c) 17mm

Effect of spiral diameter ( $d_s$ ) on the required height for SX selection in spiral grain selector is shown in Figure 4.14. As shown in Figure 4.14, the required height decreases with larger spiral diameter ( $d_s$ ). The reason is that for the same spiral design, rising

spiral diameter ( $d_s$ ) will increase the spiral length ( $L_s$ ) and hence offers more chances for grain selection at the same height.

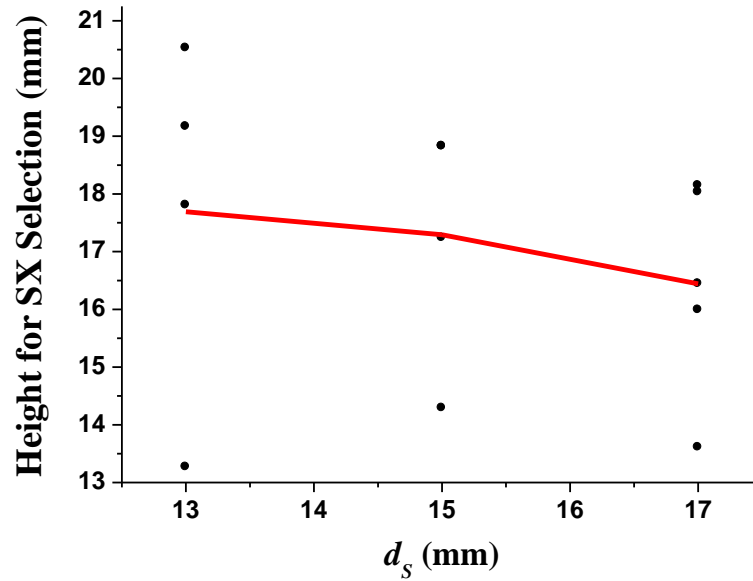


*Figure 4.14 Effect of spiral diameter ( $d_s$ ) on the required height for SX selection in spiral grain selector*

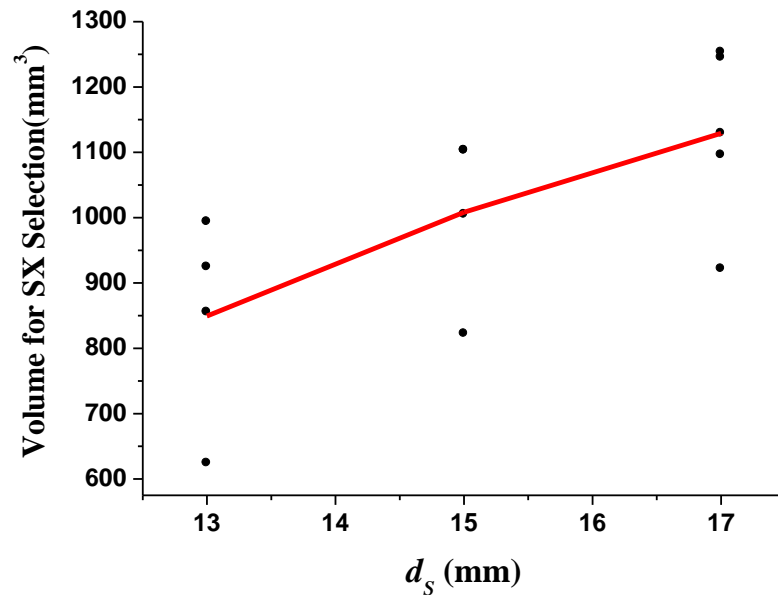


*Figure 4.15 Effect of spiral diameter ( $d_s$ ) on the required volume for SX selection in spiral grain selector*

However, when spiral diameter ( $d_s$ ) increases, the corresponding volume for the same height increases according to Equation 4.2. As a result, the required volume for SX selection is not optimised by varying spiral diameter ( $d_s$ ) (shown in Figure 4.15).

The predicted results of the final SX orientation for different spiral diameters ( $d_s$ ) are illustrated in Figure 4.16. Similar to the effect of wax wire diameter ( $d_w$ ), the final SX orientations are randomly distributed from  $20^\circ$  to  $45^\circ$ , with no obvious correlation between the final SX orientation and spiral diameter ( $d_s$ ).

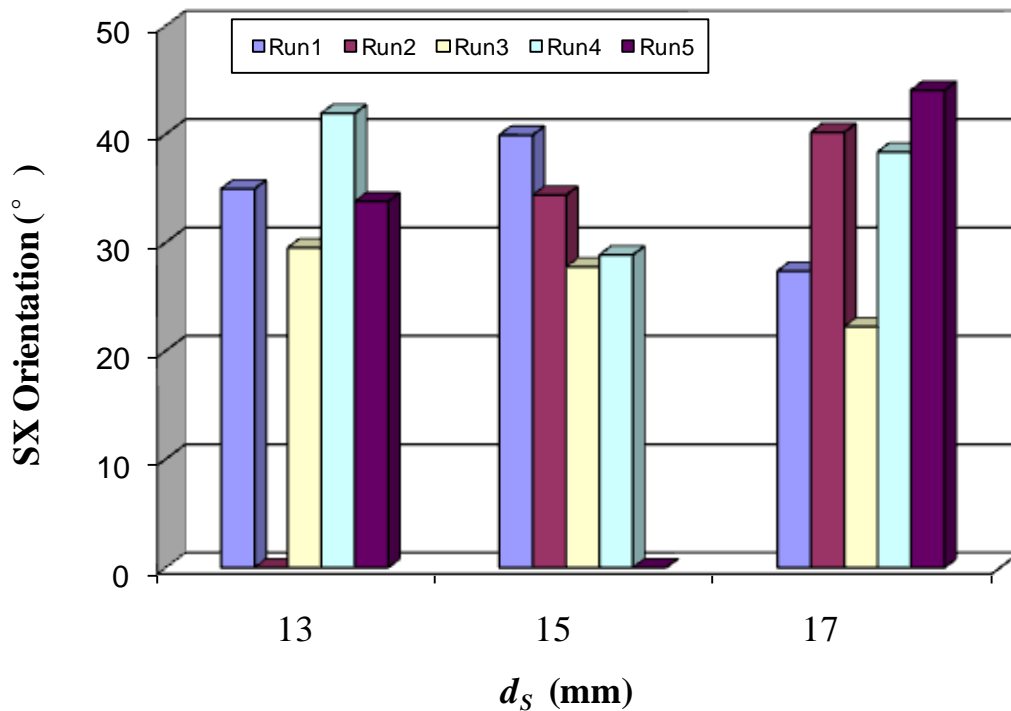


*Figure 4.16 Effect of spiral diameter ( $d_s$ ) on the final SX orientation in spiral grain selector*

#### 4.1.3.5 Effect of Spiral Take-off Angle

To investigate the effect of spiral take-off angle ( $\theta$ ) on the spiral efficiency, spirals with different take-off angles from  $20^\circ$  to  $70^\circ$  are simulated. Figure 4.17 shows an example of the grain structure in the spirals with different take-off angles  $\theta$ . According to Equation 4.1, the corresponding pitch length ( $L_p$ ) is increased with the rise of spiral

take-off angle  $\theta$  as shown in Figure 4.17. The pitch length ( $L_P$ ) of a spiral with  $70^\circ$  take-off angle (shown in Figure 4.17 (c)) is six times longer than that of a spiral with  $20^\circ$  take-off angle (shown in Figure 4.17 (a)).

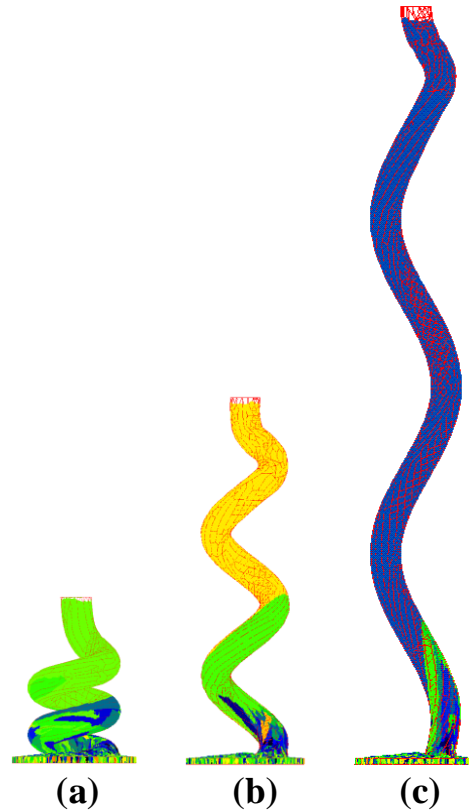


**Figure 4.17** Grain structure in the spiral selector with spiral take-off angle ( $\theta$ ) of: (a)  $20^\circ$ ; (b)  $50^\circ$ ; (c)  $70^\circ$

Corresponding to different spiral take-off angles ( $\theta$ ), the simulated results of required height for SX selection are shown in Figure 4.18. This reveals that a single grain is selected at a higher location in the spiral with a larger spiral take-off angle ( $\theta$ ) and in turn reduces the efficiency of the spiral in SX grain selection. This can be explained by the following possible reasons: firstly, with a smaller spiral take-off angle ( $\theta$ ), the grains in the spiral have less height to grow and have more chance to be blocked by the spiral wall during solidification. Hence, the grain number will be decreased more quickly with a smaller spiral take-off angle ( $\theta$ ). Secondly, as indicated by Equation 4.1, smaller take-off angle corresponds to smaller pitch size, which means the cycle time for the spiral

selection is shorter and hence can improve the spiral efficiency. Thirdly, smaller spiral take-off angles ( $\theta$ ) offer more opportunity for the growth of secondary arms and dendrite branching, which can also reduce the chance for grain survival and thereby makes grain selection more rapid than spirals designed with larger take-off angles.

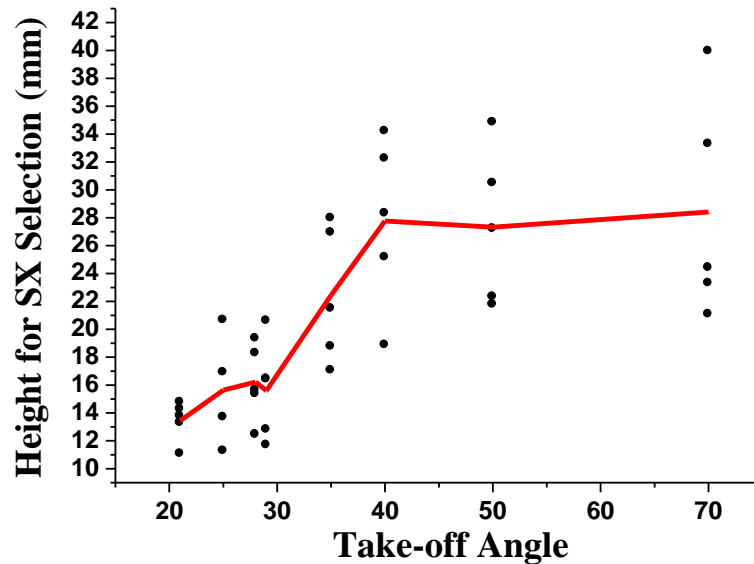


**Figure 4.18** Effect of spiral take-off angle ( $\theta$ ) on the required height for SX selection in spiral grain selector

To conclude, grain selection in the spiral during investment casting significantly depends on the spiral geometry. Increasing the spiral take-off angle ( $\theta$ ) will reduce the spiral efficiency in SX grain selection. However, this reduction in spiral efficiency becomes less obvious when spiral take-off angle ( $\theta$ ) is above 40°. This indicates that the spiral geometry control in the grain selection is vital when spiral take-off angle ( $\theta$ ) is small. When the spiral take-off angle ( $\theta$ ) is increased to 70°, the geometry control is not efficient and thermal control begins to play a role in the grain selection. As a result, the height for SX selection becomes larger and final SX orientation becomes smaller (shown in Figure 4.18). However, considering the diameter of the spiral itself, too small a take-off angle ( $\theta$ ) is not practical for spiral production. This probably explains why the

take-off angle in the spiral selector is normally chosen to be between  $25^\circ$  to  $30^\circ$  in the single crystal casting process in industrial practice.

Effect of spiral take-off angle ( $\theta$ ) on the required volume for SX selection in spiral grain selector is illustrated in Figure 4.19.

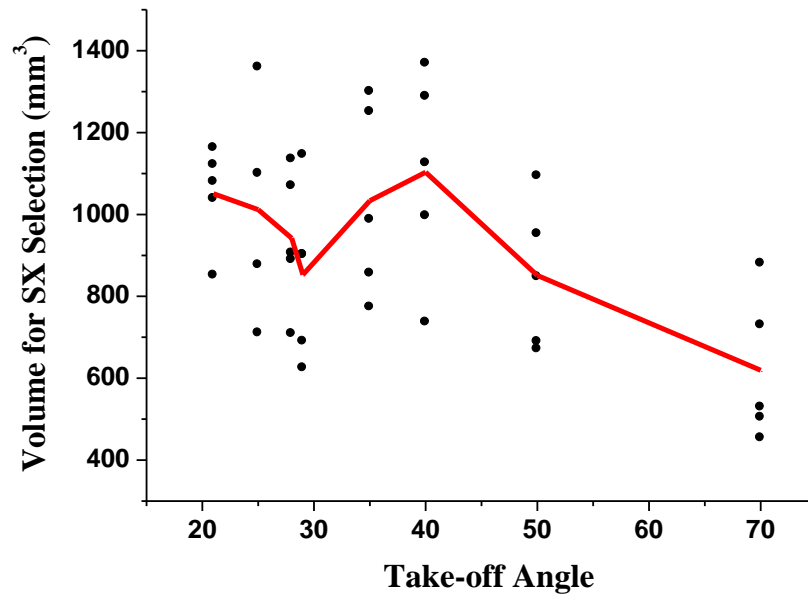


**Figure 4.19** Effect of spiral take-off angle ( $\theta$ ) on the required volume for SX selection in spiral grain selector

Although the height for SX selection is reduced with a smaller spiral take-off angle ( $\theta$ ), the corresponding pitch length ( $L_p$ ) is increased. As indicated by Equation 4.2, the spiral volume for the same height is hence increased. As a result, no consistent trend is found on the required volume for SX selection in terms of different take-off angles ( $\theta$ ). But when spiral take-off angle ( $\theta$ ) is larger than  $40^\circ$ , the volume for SX selection can be reduced with the rising of spiral take-off angle ( $\theta$ ) due to the increased pitch length ( $L_p$ ). So it can be concluded the largest volume for SX selection is required when take-off angle ( $\theta$ ) is  $40^\circ$ .

Figure 4.20 shows the predicted results of the final SX orientation for different spiral take-off angles ( $\theta$ ). No apparent correlation between SX orientation and spiral take-off angle ( $\theta$ ) is found which proves the random selection of grain orientation in the spiral. However, as discussed earlier, when the spiral take-off angle ( $\theta$ ) is increased to  $70^\circ$ , the final SX grain orientation is reduced. This is because thermal control starts to play a role in the grain selection due to the spiral geometry, and hence enables the well-aligned grains to grow quicker and overgrow the mis-oriented grains, leading to a reduction in the final SX orientation.

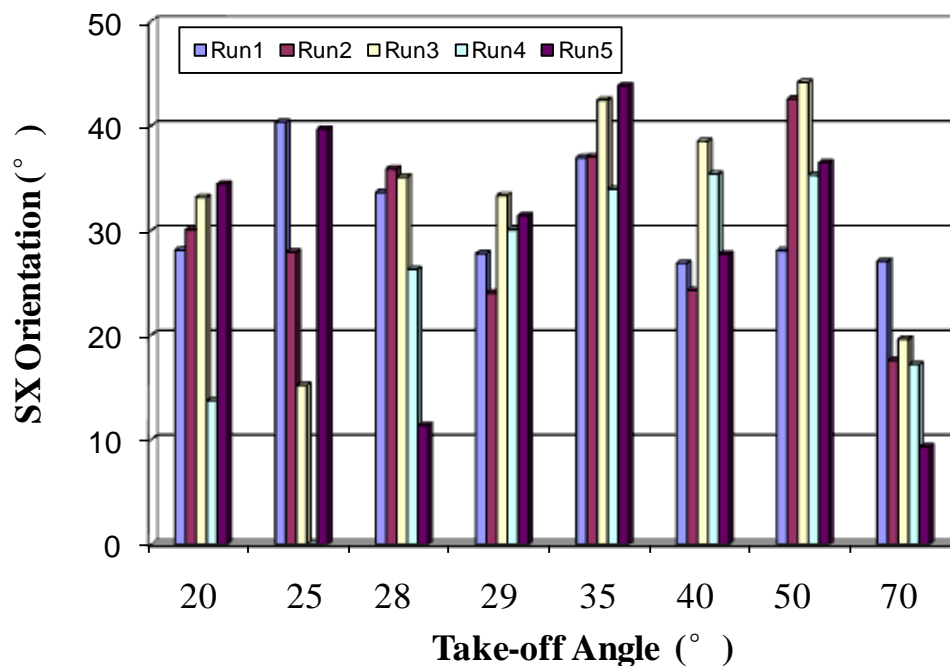


*Figure 4.20 Effect of spiral take-off angle ( $\theta$ ) on final SX orientation in spiral grain selector*

## 4.2 Sensitivity Study of Grain Selection in Full Size SX Grain Selector Combined with Designed Spiral

The role of starter block and spiral selector in grain selection has been discussed individually in the previous sections. The starter block is normally used to obtain grain orientations well-aligned with the thermal gradient and the height of the starter block is

critical for the grain orientation control. The spiral selector is more effective in the control of grain number, making sure that only one grain will be quickly selected for the turbine blade. The effects of spiral geometry and dimensions on the efficiency of grain selection have been systematically studied with the consideration of wax wire diameter ( $d_w$ ), spiral diameter ( $d_s$ ) and take-off angle ( $\theta$ ). However, the grain orientations cannot be controlled by spiral selector. So a full size starter block is required to combine with the spiral selector to control both the efficiency and the quality of the grain selection. Therefore, in this section, full size SX grain selectors are designed based on the previous spiral selector study and the efficiency of these full size grain selectors will be discussed.

Corresponding to the spiral designs in Table 4-1, 18 cases are used with a starter block of 30 mm located at the bottom according to the common industrial practice.

Figure 4.22 shows an example of the longitudinal section views of the casting furnace and a full size grain selector corresponding to Case 1. To save computational time, only this grain selector together with a charge bar at the top is simulated. The boundary conditions and simulation parameters used in the thermal calculation are obtained from the measured experimental results (Jennings, 1996).

In this section, a sensitivity study will firstly be performed to validate the reliability of the simulation results to examine the random nature of nucleation generation. Then the influence of spiral geometries on the efficiency of full size grain selectors will be investigated. Finally, SX orientation according to different spiral geometries will be discussed.

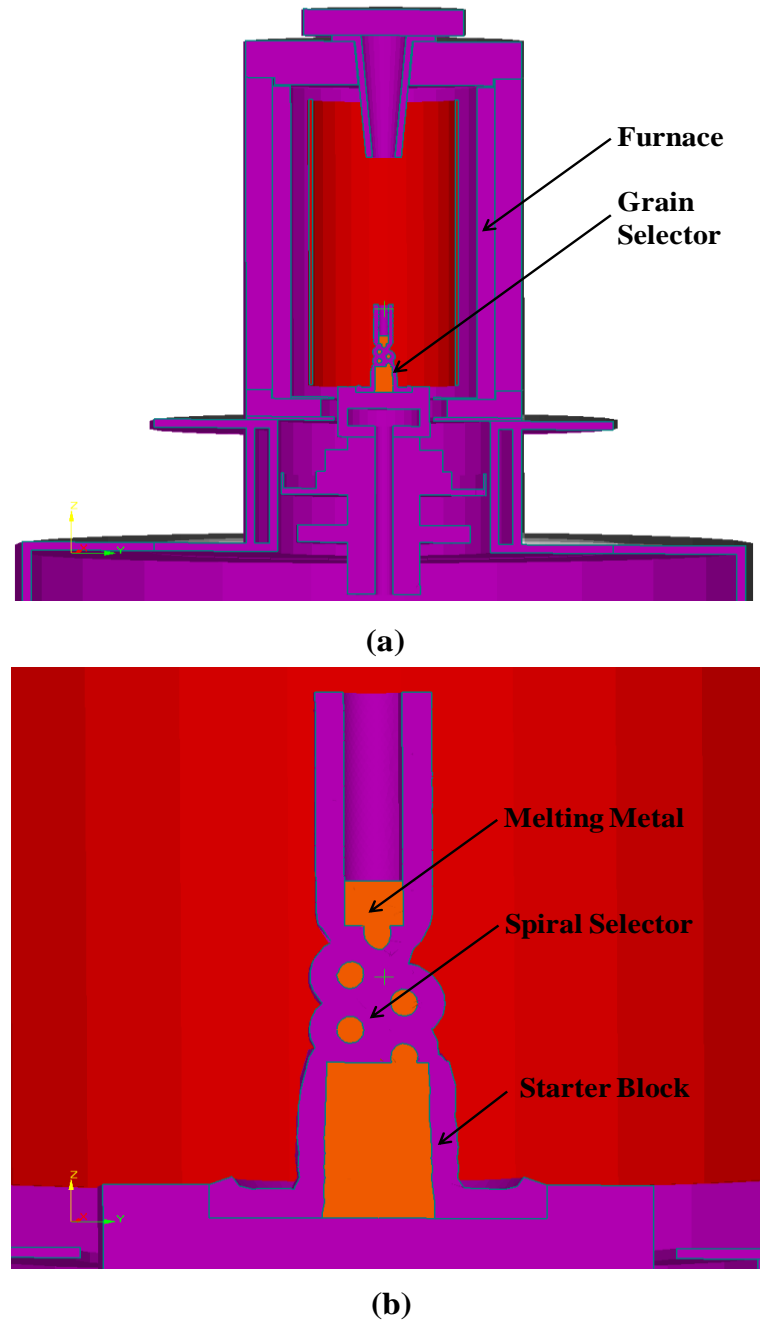


*Figure 4.21 (a) Longitudinal section view of investment casting furnace for Case 1; (b) detailed view of grain selector*

#### 4.2.1 Sensitivity Study on Random Nucleation Generation

The random nature of nucleation events has been mentioned several times in the previous discussion and must be carefully considered to make the simulation results

reliable. In this section, simulation of grain selection for every case has been repeated 100 times with a random nucleation generator. The dependence of grain selector efficiency on the number (population) of the simulation will be discussed.

Taking Case 16 as an example, distributions of the required heights for SX selection in grain selector according to different simulation runs are illustrated in Figure 4.22.

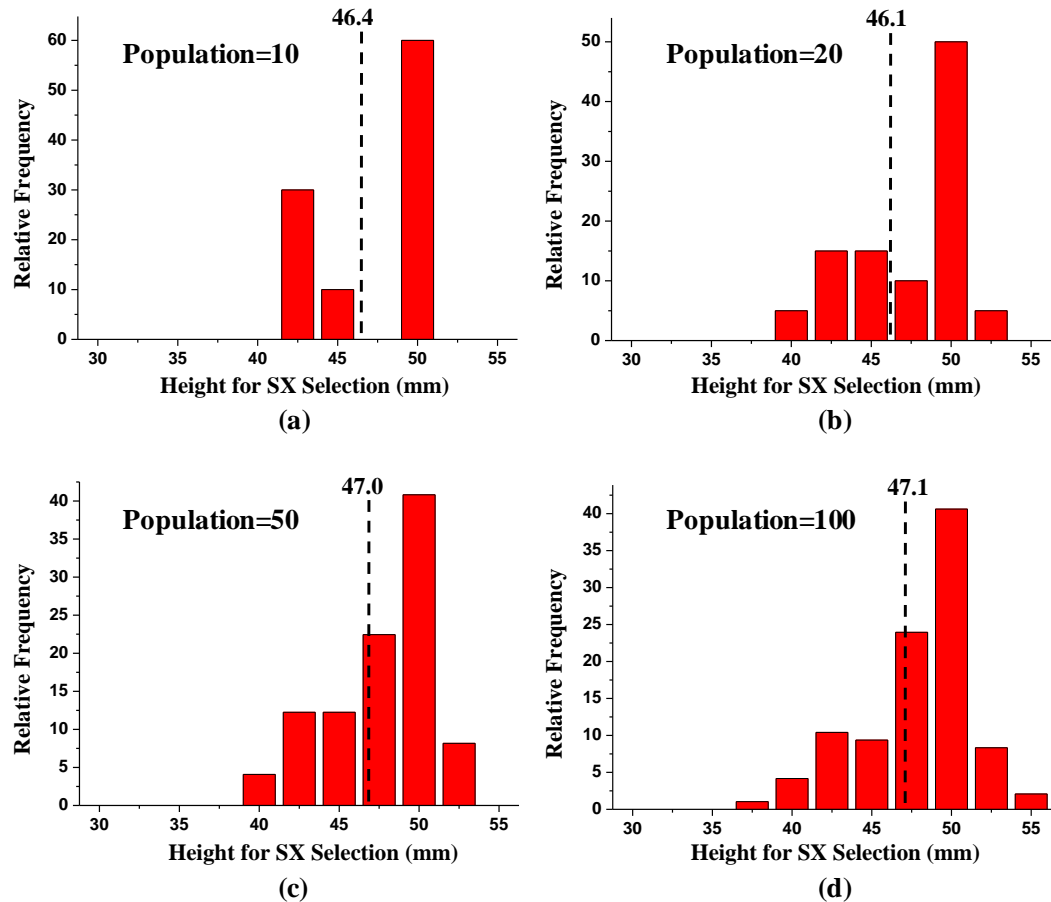


**Figure 4.22** Distribution of required heights for SX selection in grain selector (Case16) when population is: (a) 10; (b) 20; (c) 50 and (d) 100.

The average required height for SX selection is indicated by the dashed black line and the value is also marked above the line. With a larger population, more results are considered which improves the accuracy on the grain selector efficiency study. However, for the average value of the required height for SX selection, a population of

10 shows an average height of 46.4 mm (Figure 4.22 (a)) while a population of 100 shows an average height of 47.1 mm (Figure 4.22 (b)). The discrepancy between these two figures is less than 1.5%. This verifies that the study on the grain selector efficiency does not have a strong dependence on the number of repeat times. Considering both the computational efficiency and the accuracy of the simulations, a repeat number of 30 is applied for the following investigations on the grain selection efficiency for different designs of the full size grain selectors.

#### **4.2.2 The Influence of Spiral Designs on the Efficiency of Grain Selection for Full Size SX Grain Selector**

In the previous spiral study (Section 4.1.3.5), it is found that take-off angle plays a decisive role in the efficiency of grain selection in the spiral. In this study, a 30 mm starter block is added at the bottom to control the final SX grain orientation for commercial industrial applications. An example of the grain structures inside of the grain selector for different spiral take-off angles ( $\theta$ ) is shown in Figure 4.23. Every single case is repeated for 30 times based on the previous stochastic study. Case 18 ( $\theta=70^\circ$ ) is not included in this study since the spiral is too long for commercial use.

Figure 4.24 illustrates the influence of spiral take-off angle ( $\theta$ ) on the required height for SX selection in the newly designed grain selector. 30 runs are repeated for every spiral design and the results are indicated by the points in the figure. The ‘average value’ method is proved to be able to represent the required height for SX selection to investigate the grain selector efficiency based on the sensitivity study in Section 4.2.1 and the average heights according to different spiral take-off angles ( $\theta$ ) are indicated with the red line. Due to the effect of spiral take-off angle ( $\theta$ ) on the grain selection (see Section 4.1.3.5), the required height for SX selection in the newly designed grain selector is increased with the rise of spiral take-off angle ( $\theta$ ). Compared to the grain selector with a  $50^\circ$  take-off angle, the required height for SX selection of the grain selector with a  $20^\circ$  take-off angle can be reduced by 14.2%. The reduction of the required height will be beneficial for the control of both the casting time and casting

quality. Therefore, a smaller spiral take-off angle will be required in the full size grain selector design to improve the efficiency of the SX grain selection.

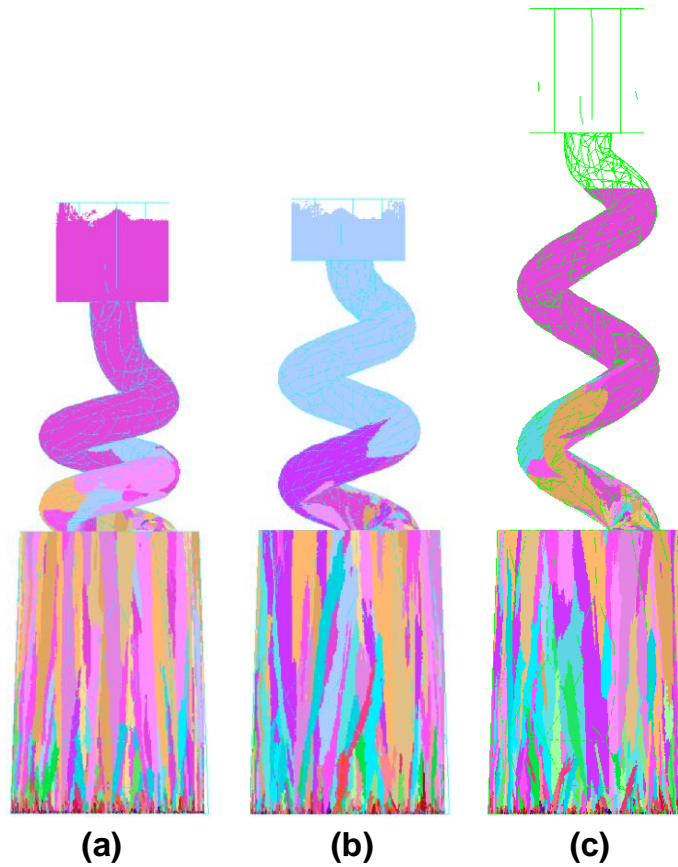


**Figure 4.23** Grain structure in designed grain selector with spiral take-off angle ( $\theta$ ) of: (a)  $20^\circ$ ; (c)  $35^\circ$ ; (d)  $50^\circ$

It is worthy of note that the results of the full size grain selector design show good agreement with those of the previous spiral study. This indicates that the spiral geometry does have an important impact on the grain selection in terms of controlling the grain number during investment casting and optimisation of the spiral geometry will improve the efficiency of the SX grain selector. Due to the limitation of computational resources, the stochastic study of influences of wax wire diameter ( $d_w$ ) and spiral diameter ( $d_s$ ) on grain selection for the full size grain selector was not carried out, and this forms part of future work.

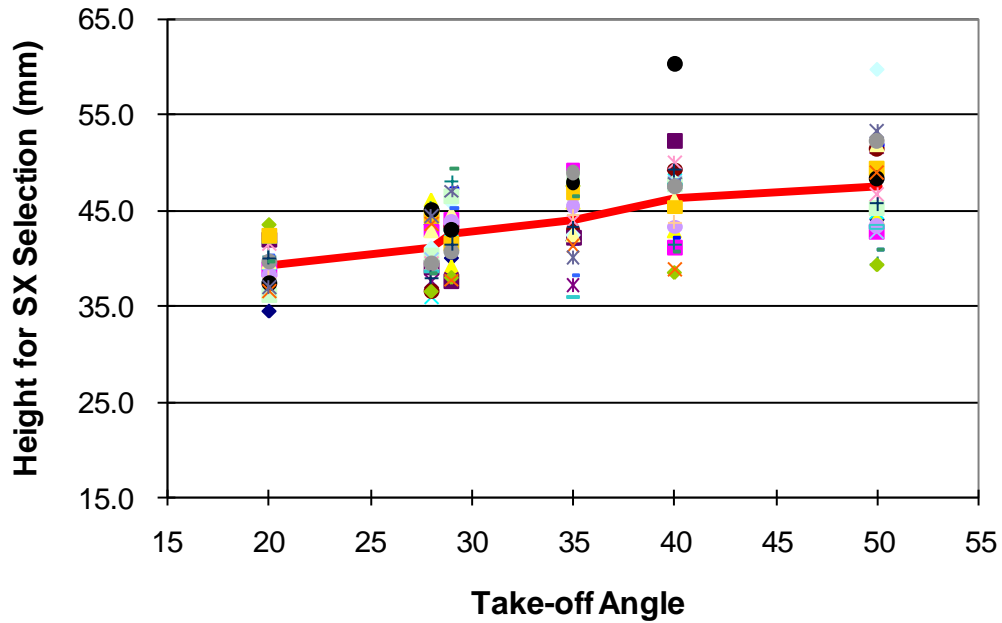


*Figure 4.24 The influence of spiral take-off angle ( $\theta$ ) on the required height for SX selection in full size grain selectors*

The final SX grain orientations corresponding to full size grain selectors with different spiral take-off angles ( $\theta$ ) are further investigated. Simulation for every design has been repeated for 100 times to take into account the effect of random nucleation. As illustrated in Figure 4.25, most of the final SX orientations can be controlled within  $18^\circ$  by the full size grain selector with a 30 mm starter block. This confirms that the starter block is effective in grain orientation selection and the height of starter block is critical for the final grain orientation. However, no obvious correlation can be found between the final SX grain orientation and spiral take-off angle ( $\theta$ ). This again proves our speculation that spiral has no role in optimisation of the grain orientation selection and the spiral will not influence the final SX orientation.

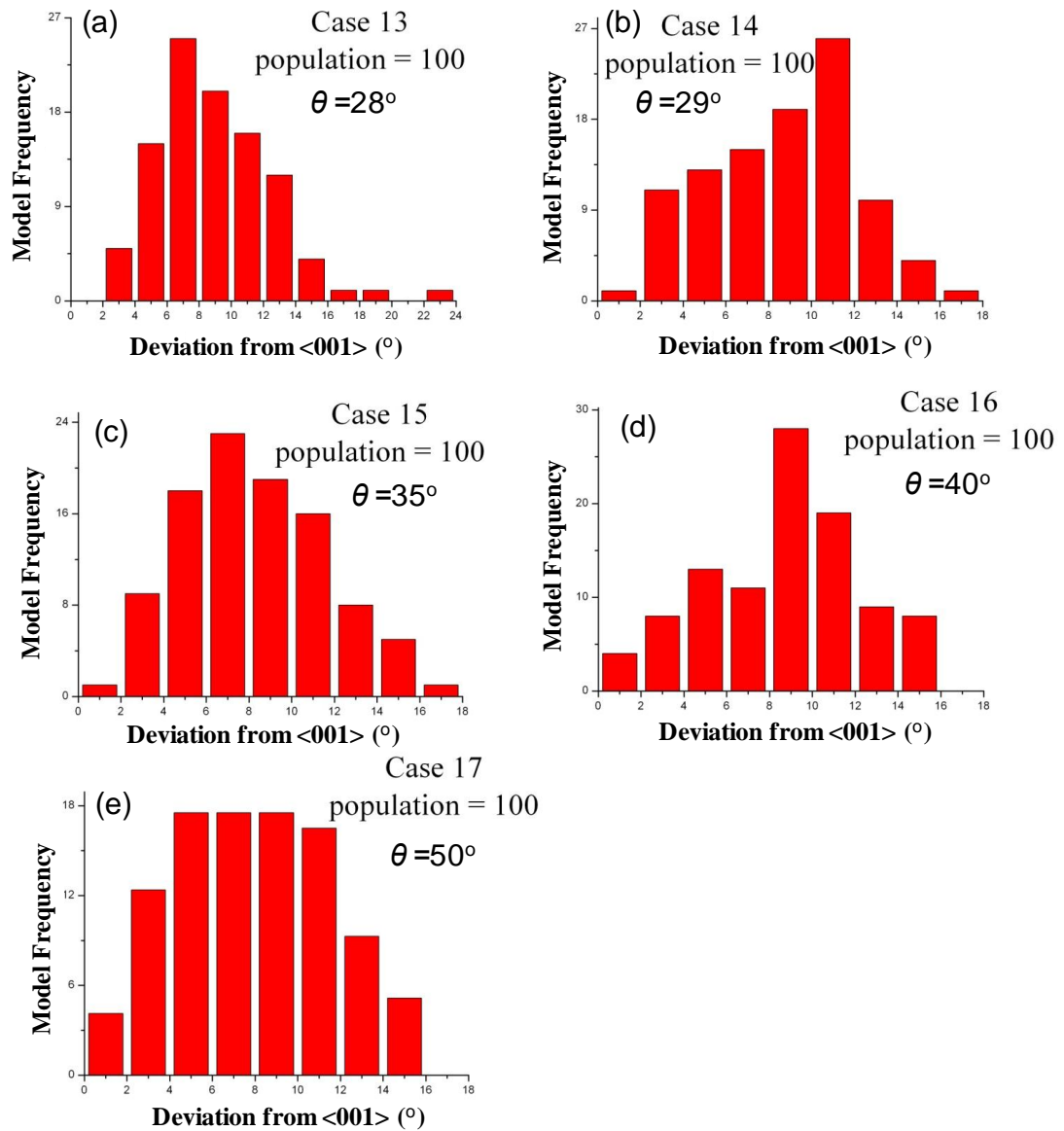


*Figure 4.25 Final SX grain orientations for full size grain selectors with spiral take-off angle ( $\theta$ ) of: (a)  $28^\circ$ ; (b)  $29^\circ$ ; (c)  $35^\circ$ ; (d)  $40^\circ$ ; (e)  $50^\circ$*

### 4.3 Experimental Validation of Grain Selection in Spiral Selector

Corresponding experiments have been carried out using a fully instrumented industrial directional casting furnace. Considering the cost and difficulty in making the spiral

moulds and in investment casting, the experiments were concentrated on the validation of the effect of spiral take-off angle ( $\theta$ ). In this section, details of the investment casting will first be introduced. Then the grain structure of the casting components will be examined using optical microscopy. Analyses of the grain structure evolution and crystallographic texture evolution in the spiral selector then follow using electron backscatter diffraction (EBSD) in a FEI Field Emission Gun Scanning Electron Microscope (FEGSEM). Finally, the mechanism of grain selection in spiral selector will be proposed.

### **4.3.1 Details of Investment Casting Procedure Employed**

The basic procedure of investment casting has been introduced in Chapter 2. As described earlier, the first step is producing the wax mould. Figure 4.26 shows two sets of the wax moulds with different spiral take-off angles ( $\theta$ ) as an example. The wax mould was assembled from different wax components which were prepared using a semi-automatic wax injection machine (Mueller-Phipps Model 54-20).

The spiral wax was made by using 5 mm wax wire rotating around different metal moulds giving various dimensions for different spiral take-off angles ( $\theta$ ) from 20° to 70° corresponding to Cases 11-18 listed in Table 4-1. For each design, four identical spirals were made for validation and assembled directly on one chill plate to enable more grains to grow into the spiral because 1 mm starter block is, in practice, difficult to produce. A long cylindrical downpour was located in the middle to increase the pressure and allow the pouring metal to flow to the bottom of the spiral. Also, a few slim cylindrical bars were used to connect the spirals with the middle cylindrical downpour and hold the spirals to maintain the original shapes during the ceramic coating. Some impurities and gas contaminants can also be pulled out through these slim bars during investment casting. When assembling these wax components, special attention is required to make sure that the joint area is smooth without any hole to prevent the ceramic powder from going inside during the following ceramic coating process and causing crack of the mould.



**Figure 4.26** Wax moulds with different spiral take-off angles ( $\theta$ ) of: (a)  $28^\circ$  and (b)  $50^\circ$

When the wax pattern assembly was ready, the second step was making the ceramic shell using the wax assemblies. Wax assemblies were dipped into ceramic slurry and drained to give a uniform wet coating. Then the surface was ‘stuccoed’ with coarse ceramic grit to adhere to the wet coating and harden it. To build up the shell thickness, six layers were repeated including the primary coating and two hours interval was applied to dry every layer.

When the ceramic shells were produced, the moulds were de-waxed in a steam autoclave, and then fired at the temperature of  $800^\circ\text{C}$  to remove all the residual wax and strengthen the ceramic shell by partial sintering.

A fully instrumented industrial directional casting furnace (based in the Interdisciplinary Research Centre (IRC), University of Birmingham, UK) was used for the investment casting in this study. The shell mould produced was mounted on a water cooled copper chill in the centre of the furnace chamber as shown in Figure 4.27. The

2<sup>nd</sup> generation single crystal superalloy CMSX4 was used for the casting, the chemical composition of which is given in Table 4-2.

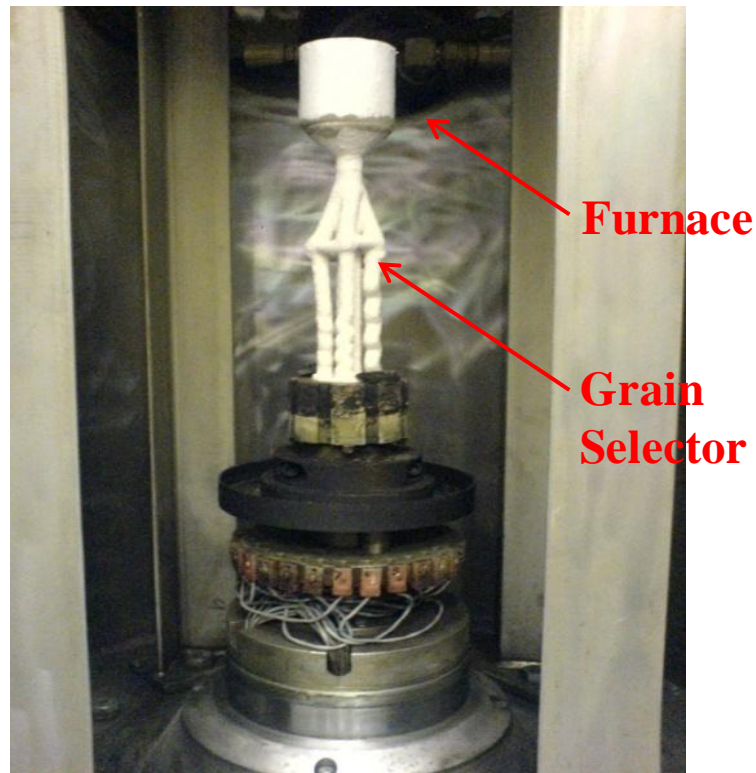


*Figure 4.27 Photograph of the directional casting furnace and instrumented mould prior to casting*

*Table 4-2 Nominal composition (wt. %) of CMSX4*

Cr	Co	Mo	W	Ta	Re	Al	Ti	Hf	Ni
6.5	9.0	0.6	6.0	6.5	3.0	5.6	1.0	0.1	Bal

As discussed earlier, to maintain the columnar dendritic structure and minimize defect formation such as stray grains during casting, a high thermal gradient and a low growth velocity are required. Efforts are made to increase the withdrawal velocity in order to shorten the casting time. As a result, the pouring temperature of the charge was selected as 1570 °C, considering both the thermal gradient requirement and the strength of the ceramic shell at high temperature. A series of water cooled baffles were used to keep heat flux perpendicular to the direction of withdraw and maintain an effectively planar

solid/liquid interface. During solidification, a withdrawal velocity of  $0.06 \text{ mm s}^{-1}$  was maintained and the whole casting process took approximately four hours.

### 4.3.2 Microstructure Analyses using Optical Microscopy

To compare with the simulation results, different spirals were further analysed after casting. Using optical microscopy, the grain structures for different spirals produced during directional solidification were viewed and the efficiency of grain selection in the spiral corresponding to spiral designs was investigated.

Figure 4.28 shows the grain structures of the casting trials with different take-off angles ( $\theta$ ). Before visual observation of the grain structures, the spirals were macro-etched using an electrolytic and chemical etch method routinely used in industrial practice in Precision Casting Facility, Rolls-Royce Plc.

As illustrated in Figure 4.28, at the bottom of the spiral, there are a large number of grains with random grain orientations and the grain size is very small. With competitive growth during solidification, the grain number quickly decreases. Finally, a single grain survives. In Figure 4.28 (a) – (c), three different spiral castings are compared in terms of different take-off angles  $\theta$ , but having the same wax wire diameter ( $d_w$ ) and spiral diameter ( $d_s$ ). A cylindrical bar with the same wax wire diameter ( $d_w$ ) was also cast and is shown in Figure 4.28 (d). As illustrated in Figure 4.28, the red lines indicate the required height for SX selection. With the increase of the spiral take-off angle ( $\theta$ ), the single grain structure occurs at a later stage, reducing the efficiency of grain selection within the spiral. Compared with the spiral selector, the cylindrical bar does not successfully select one single grain after the similar length (shown in Figure 4.28 (d)), which reveals the importance of the spiral selector in grain selection during directional solidification.

The experimentally observed heights for single crystal selection are superimposed on the simulated results. As illustrated in Figure 4.29, solid symbols stand for the experiment results and open symbols stand for the simulation predictions. The results show good qualitative agreement and reveal that spiral selector becomes more efficient

with a smaller take-off angle ( $\theta$ ), confirming the importance of the spiral designs on the efficiency of grain selection during directional solidification.

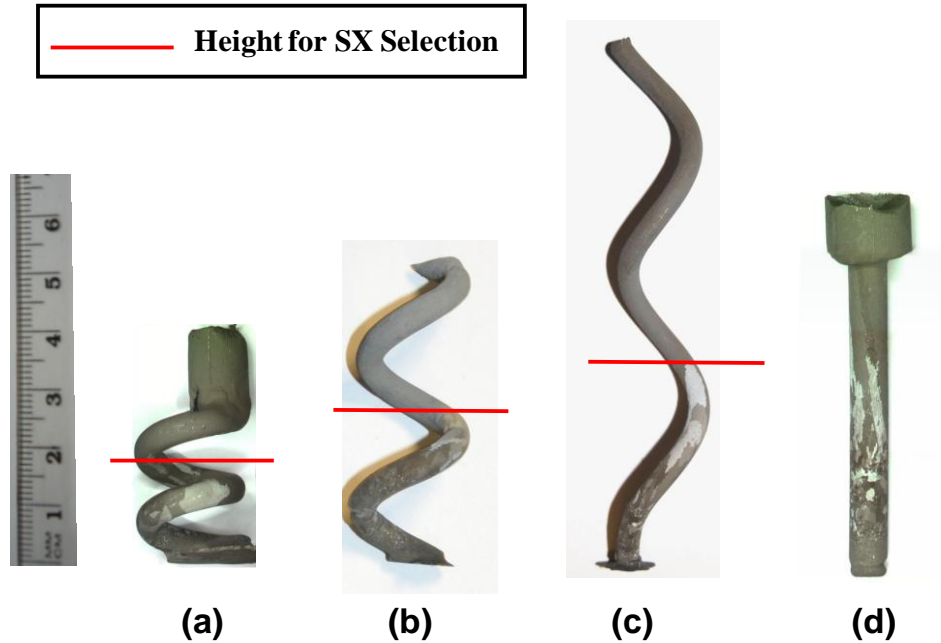


Figure 4.28 Grain structures of the casting trials with spiral take-off angle ( $\theta$ ) of: (a) 28°; (b) 50°; (c) 70° and (d) a cylindrical selector

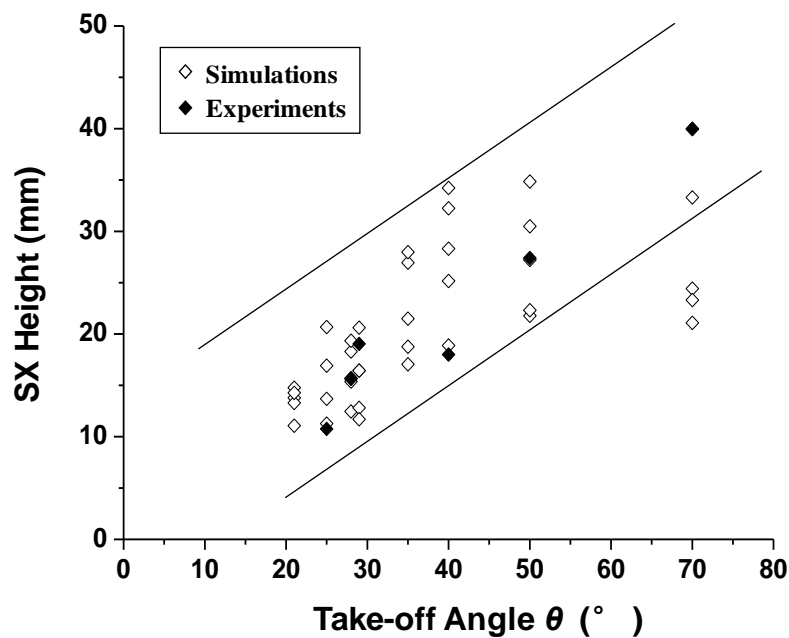


Figure 4.29 Predicted and experimentally observed results of heights for SX selection vs. take-off angle ( $\theta$ )

### 4.3.3 EBSD Analyses on Grain Selection in the Spiral Selector

In this section, electron backscatter diffraction (EBSD) analyses of grain size and texture distributions at different heights of the spiral selector are carried out to investigate the selection of grain orientations in the spiral and to compare with the simulation predictions.

Electron back scattered diffraction (EBSD) is a microstructural-crystallographic technique used to examine the crystallographic orientation of the specimen. It is conducted using a Scanning Electron Microscope (SEM) equipped with a backscatter diffraction camera. When the electron beam impinges on the specimen (usually tilted at  $70^\circ$  to the horizontal), the electrons interact with the atomic lattice planes of the crystalline structures which satisfy Bragg conditions and undergo backscatter diffraction. The diffracted electrons produce Electron Backscatter Patterns (EBSP), which consist of parallel lines, known as Kikuchi lines or bands, corresponding to a family of crystal lattice planes (Yardly *et al.* 2007; Mingard *et al.* 2009; Krishna 2008). The patterns are then imaged using a phosphor screen attached to the backscatter diffraction camera and automatically indexed by the control software to determine the crystal orientations, measure grain boundary misorientations, discriminate between different materials, and provide information about local crystalline perfection (illustrated in Figure 4.29) (Coleman 2006).

Since the diffracted electrons that produce the patterns for indexing can only escape from the top 10-20 nm of the surface, a highly polished, deformation free, flat surface is required in order to collect high quality EBSD data. In this study, the sample surface were polished to a  $1\ \mu\text{m}$  finish and then polished for a further 10 minutes with colloidal silica. EBSD data were collected using an accelerating voltage of 20 kV and spot size of 5 in a FEI Field Emission Gun Scanning Electron Microscope (FEGSEM). A magnification of  $35\times$  equipped with a step size of  $50\ \mu\text{m}$  were used considering both the accuracy and analysis time. The generated maps were scanned at high percentage (90%) of index hitting rate. EBSD data were then further analysed using software offered by

HKL technology, assuming a face centred cubic (FCC) crystal structure with a lattice parameter of 0.36 nm.

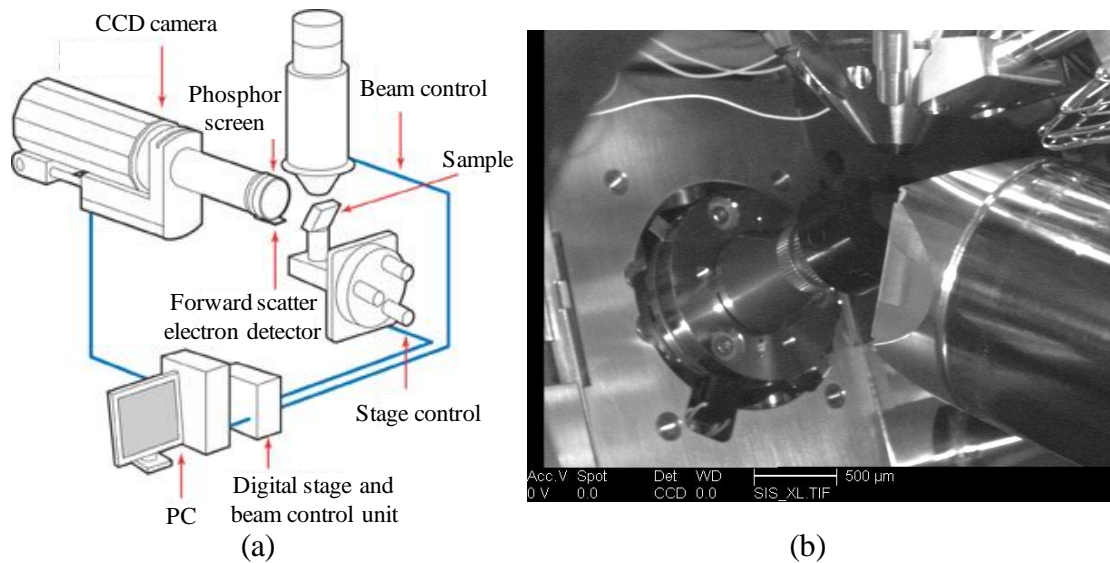


**Figure 4.30 (a) Schematic of EBSD system and (b) the experiment set up for EBSD (Coleman, 2006)**

Figure 4.30 shows the analysis results for case 17. Figure 4.30 (a) is an image taken using optical microscopy, Figure 4.30 (b1) - (d1) show the grain texture evolution of cross sections at different heights of the spiral and Figure 4.30 (b2) - (d2) show the corresponding  $\langle 001 \rangle$  inverse pole figures for grain orientations along the withdrawal direction. Inside of the spiral, grains grew along the direction indicated by the red arrows shown in the figure.

Figure 4.31 (b1) shows the grain texture at the section near the bottom of the spiral. The grain boundaries can be seen clearly in the image and different grains were plotted using different colours. There were a large number of grains nucleated at the bottom. As shown in the inverse pole figure along the heat flux direction (Figure 4.28 (b2)), grain orientations were randomly distributed. With the increase of the height, competitive growth made the grain number decrease and surviving grain sizes became larger. Corresponding grain orientations were plotted in the inverse pole figure along the direction of heat flux shown in Figure 4.31 (c2). No preferred texture was identified at

this height and the grain orientations were randomly selected during the solidification. At the height of one pitch (Figure 4.31 (d1)), the grain number was quickly minimized to less than 20. Consistent with the simulation results, this again confirms the efficiency of the spiral selector in selecting grains. At the height of one and a half pitches (position (e)), one single grain was finally selected shown in the blue colour and the grain orientation for the final single grain was  $22^\circ$ . As indicated by the red circle in the inverse pole figures, the final SX overgrew the other grains with both larger and smaller orientations. The analyses of grain structure evolution orientations in the spiral prove that the spiral selector has no role in optimisation of grain orientations and we propose the grain selection in the spiral is dominated by geometrical control which will be further discussed in the next section.

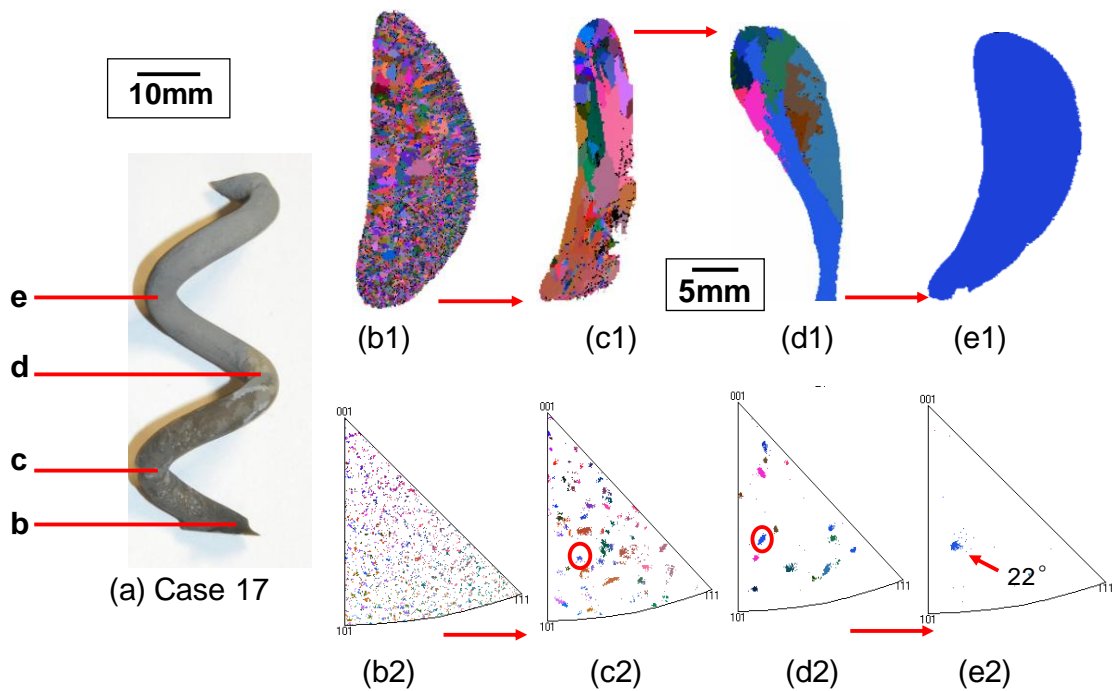


**Figure 4.31** (a) Optical photograph of the cast spiral (Case 17); EBSD analyses on the grain structure evolution ((b1)-(d1)) and the corresponding  $\langle 001 \rangle$  pole figures at different heights of: (b) 0 mm; (c) 12mm; (d) 24 mm; (e) 36 mm from the bottom of the spiral.

Experimental results of the final SX orientations according to different spiral take-off angles ( $\theta$ ) are superimposed on the simulation results for comparison in Figure 4.32.

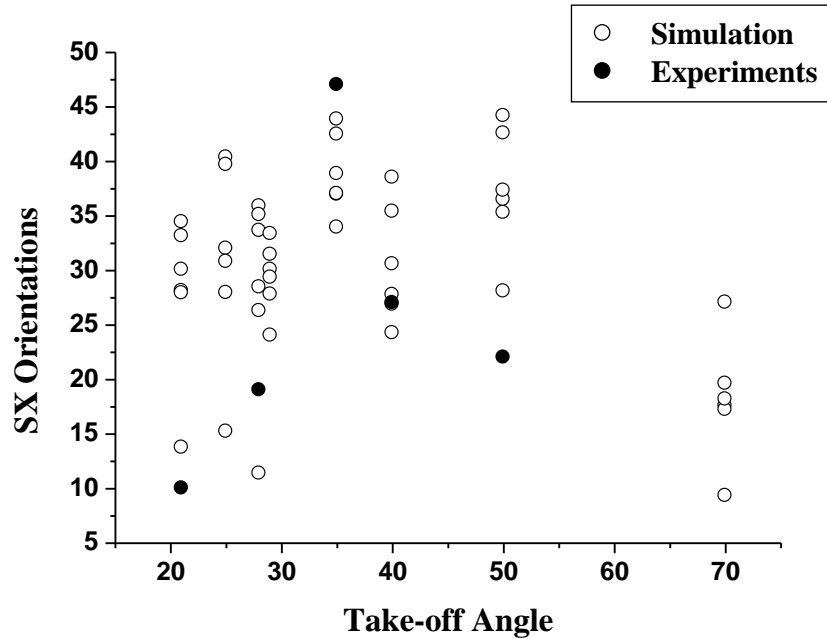


*Figure 4.32 Predicted and experimentally observed results of final SX orientation vs. take-off angle ( $\theta$ )*

With much shorter starter block (1 mm), the designed spiral selectors are not able to control the final SX orientations. Both the simulation results and experimental analyses verify that the majority of the grain orientation selection is controlled in the starter block and the spiral selector effectively selects one grain with no optimisation on grain orientation selection.

#### 4.4 Mechanism of Grain Selection in Spiral Selector

Based on both the simulation results and experimental observations, the mechanism of grain selection in spiral selector is investigated in this section.

During investment casting, the grain structure depends strongly on competitive growth. As discussed earlier in Chapter 2, thermal gradient plays a key role in this process. Figure 4.33 illustrates competitive growth during directional solidification which is dominated by the thermal gradient.

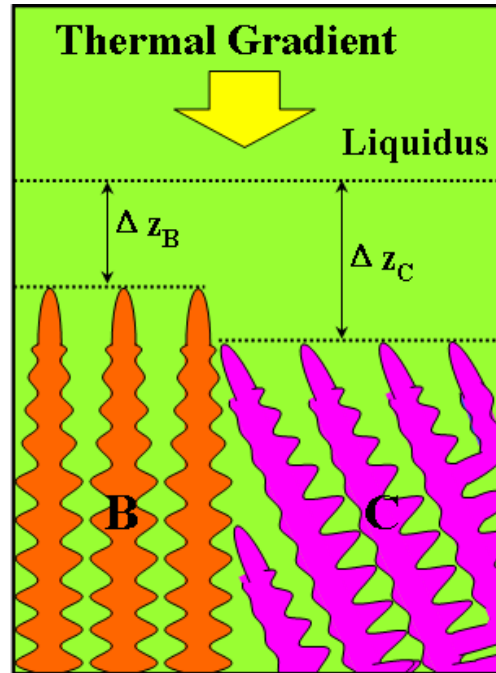


*Figure 4.33 Competitive growth controlled by the thermal gradient during investment casting*

Because of the undercooling, Grain B with a well-aligned orientation grows quicker than Grain A with mis-aligned orientation and therefore produces a preferred  $\langle 001 \rangle$  grain texture during casting. This mechanism is widely used in the directional solidification technique to produce the DS turbine blades and also contributes to the grain orientation control in the starter block of the grain selector for SX turbine blades. However, it is not capable of explaining the grain selection inside of the spiral where the large-angle grains can overgrow the small-angle grains. A geometrically controlled mechanism is proposed for the grain selection in the spiral.

To clearly illustrate the geometrical blocking mechanism, 2D schematic diagrams of the grain structure evolution in the spiral selector during solidification are shown in Figure

4.34. Three grains are prefixed at the bottom of the spiral before solidification. The orientation of Grain B is well-aligned with the vertical thermal gradient while the orientations of Grains A and C are mis-aligned. At the beginning of the solidification, three grains start to grow and Grain B grows ahead of the other two grains when there is enough space (shown in Figure 4.34 (a)). Secondary and tertiary arms develop from the primary dendrites and interact with each other. In the convergent case, Grain C is overgrown by Grain B since its primary tips hit the wall. It is worthy of note that in Figure 4.34 (b) although Grain B grows ahead, it is finally blocked by the spiral wall due to the limited space and twisted shape of the spiral. As a result, only Grain A is able to survive and grow into the next turn. If the spiral shape is changed, the surviving grains will differ and the grain structure will vary accordingly.

As shown in Figure 4.34 (c), the pitch length ( $L_P$ ) is reduced which means the spiral diameter ( $d_s$ ) is decreased for the same take-off angle. Consequently, the time for grains to reach the first turn of the spiral is shortened, which enables Grain B to pass the first turn before the spiral wall blocks it. In this case, both Grain A and Grain B survive after the first turn of the spiral and Grain B has a second chance to compete with Grain A in the next turn. This explains the reason why reducing the spiral diameter ( $d_s$ ) increases the time for SX selection. Meanwhile, if the spiral take-off angle ( $\theta$ ) is increased, the spiral will have a less sharp wall (Figure 4.34 (d)). In this circumstance, Grain B will be able to pass the first turn and compete with Grain A later on. This also explains why the SX selection time in the spiral with a larger take-off angle ( $\theta$ ) is longer. The grain structure evolution in different spirals in Figure 4.34 indicates that the competitive growth and grain selection in the spiral is dominated by the geometrical control via a blocking mechanism. Both the simulated results and experimental observations reveal that the grain selection can be controlled by altering the geometry of the spiral.

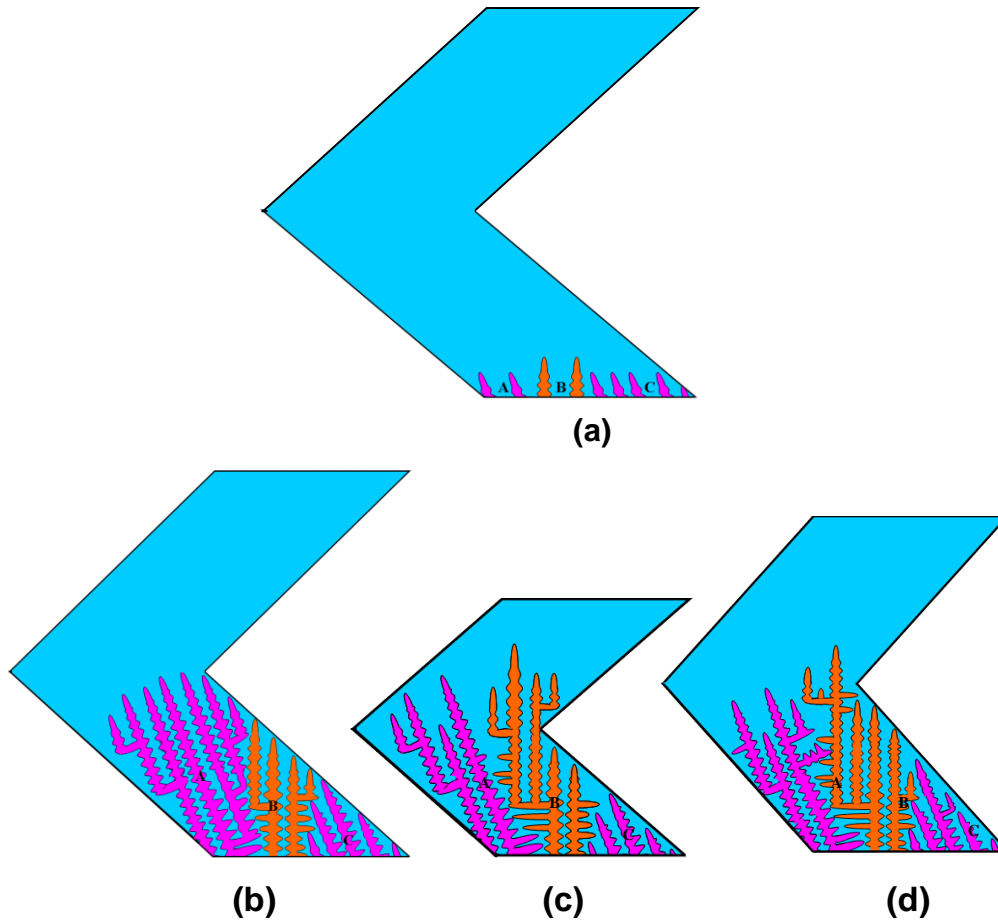


*Figure 4.34 2D schematic diagrams of a geometrical control mechanism for grain selection in the spiral: (a) grain structure at the beginning of the solidification; grain structure evolution during solidification for different spiral geometries: (b) same geometry as in (a); (c) shorten pitch length ( $L_p$ ); (d) increase spiral take-off angle ( $\theta$ )*

## 4.5 Summary

The coupled ProCAST & CAFE model for the heat transfer and microstructure evolution occurring during investment casting has been constructed and validated for the simulation of grain selection for SX turbine blades.

The roles of starter block and spiral selector in SX grain selection have been investigated individually. The starter block is normally used to ensure the grain orientations well-aligned with the thermal gradient and the height of the starter block is

critical for the grain orientation control. The spiral selector is more effective in minimising the grain number, making sure only one grain can be quickly selected for the SX turbine blade. The efficiency of the spiral selector offered by the spiral designs is found significantly dependent on its geometry and dimensions. The spiral becomes more efficient with:

- smaller wax wire diameter ( $d_w$ )
- larger spiral diameter ( $d_s$ )
- smaller take-off angle ( $\theta$ )

The effects of the spiral geometry on the grain selection are then further applied to the full size SX grain selector, which consists of a normal size starter block (30 mm) and a spiral. The results reveal that spiral geometry and dimension have an important impact on the efficiency of grain selection during investment casting. However, the control of grain orientation mainly occurs in the starter block. A sensitivity study is carried out to investigate the effect of the random nature of the nucleation on grain selection.

The mechanism of grain selection in the spiral selector has been further investigated by comparing the simulated results with experimental observations. It is proposed that the control of the grain selection inside of the spiral appears to be geometrical, via a blocking mechanism.

## **Chapter 5      Modelling the Formation of New Grains ahead of the Advancing Solidification Front**

The objective of this chapter is to quantitatively investigate the influence of casting conditions upon the formation of new grains ahead of the advancing solidification front. In this chapter, the micro-scale solidification programme,  $\mu\text{MatIC}$ , is used to simulate the dendritic structure evolution and the formation of new grains during directional solidification. Solutal interaction and undercooling ahead of the growth front will be examined using the  $\mu\text{MatIC}$  model. Then formation of stray grains in the single-crystal turbine blades will be modelled. Finally, columnar to equiaxed transition during the solidification will be investigated and conditions leading to the transition will be quantified.

### **5.1 Stray Grain Formation in Single-crystal Turbine Blades**

One of the major problems encountered during directional solidification and single crystal growth of turbine blades is the formation of new grains ahead of the advancing solidification front. In particular, as turbine blade geometries for modern engines become more complex, process requirements become more stringent and production yield emerges as a limiting factor for engine manufacturers. Many types of performance-limiting casting defects, such as freckles, stray grains, and low and high angle boundaries are related to the formation of new grains ahead of the advancing solidification front (Kurz and Fisher, 1984). The mechanisms for the formation of these defects are known in the general sense, and some progress has been made recently in quantifying them. For example, the formation of freckle channels by convective instabilities in the mushy zone has been modelled for multi-component superalloys (Tin and Pollock, 2004). In this study, a micro-scale dendrite model,  $\mu\text{MatIC}$ , is used to simulate the detailed dendritic structure evolution and to quantify the conditions leading to the formation of stray grains during directional solidification of a Ni-based superalloy IN792.

### 5.1.1 Simulation Parameters

IN792\* was chosen because casting defects, such as stray grains, often occur on directional solidification of this corrosion-resistant Ni-based superalloys (Zhang and Singer, 2004). These are schematically illustrated in Figure 5.1 (Jennings, 1996).

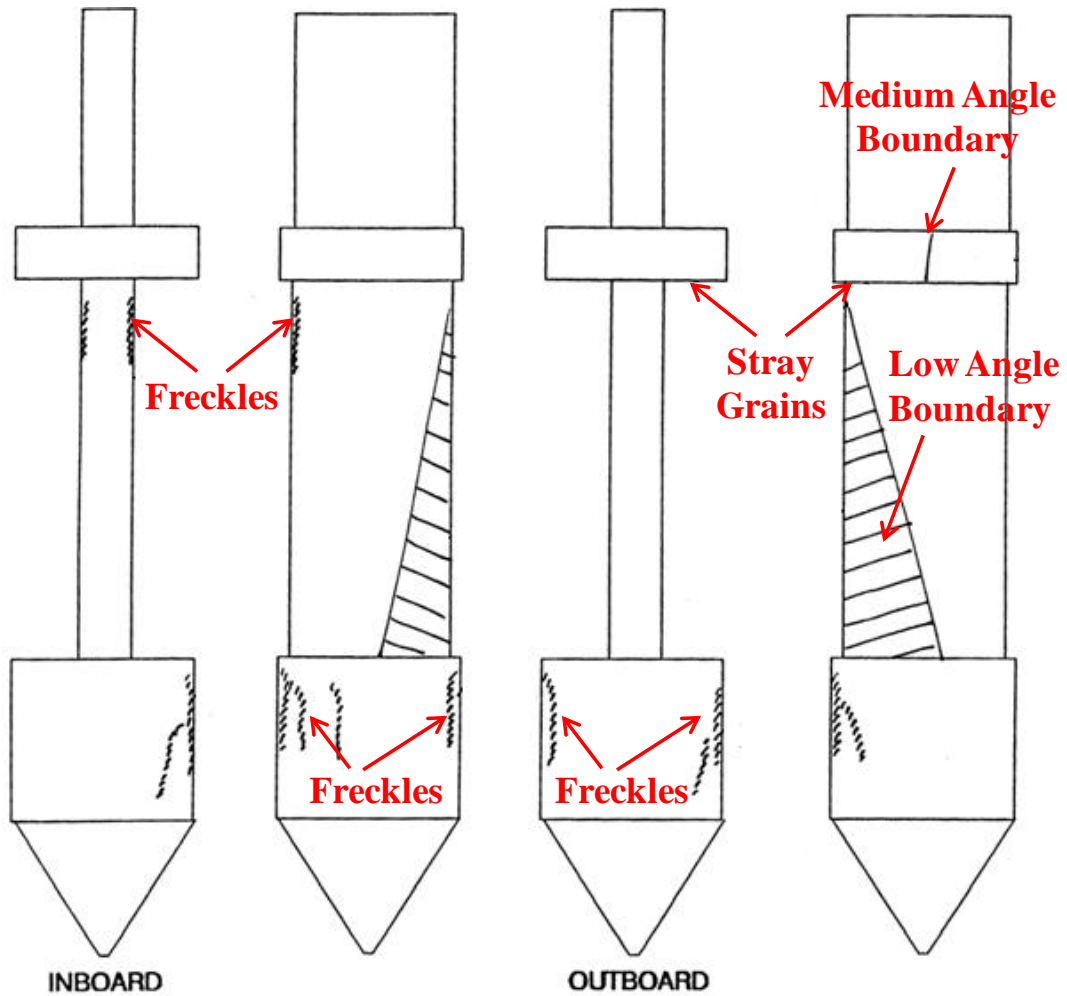


*Figure 5.1 Schematics of casting defects in Ni-based superalloy for turbine blade (Jennings, 1996) (Courtesy of Rolls-Royce Plc.)*

\* IN792 is a trademark of INCO Alloys International, Huntington Woods, WV, USA

A binary approximation of IN792 was used because the  $\mu$ MatIC model is a binary solidification programme as described in Chapter 3. Ni-Ta system was chosen for the following reasons: (1) Ta is a strongly segregating element with partition coefficient  $k$  of 0.68 at the solidification interface; (2) Ta is a slow diffusing element in IN792 and the diffusion of Ta may control the kinetics of solidification interface movement; (3) Ta has a relatively high concentration in the system. Therefore, the predicted Ta concentration can represent the solidification segregation of major alloying elements in the alloy IN792. The nominal composition of IN792 is listed in Table 5-1 and material properties and model parameters are listed in Table 5-2. Thermodynamic properties for the binary approximation were calculated using JMatPro\*. Diffusion coefficients and the Gibbs Thomson coefficient of the system were taken from Yang (2005).

**Table 5-1 Nominal composition in wt. % of alloying elements in the Ni-based superalloys, IN792 (Courtesy of Rolls-Royce Plc.)**

Ta	Al	Co	Cr	W	Ti	Mo	Hf	Ni
5.0	3.5	8.9	12.2	3.8	3.8	1.8	0.1	Bal

**Table 5-2 Material properties and model parameters used in the simulations**

Parameter	Symbol (Units)	Value
Liquidus temperature	$T_L$ (K)	1633
Liquidus slope	$m_L$ (K/wt%)	-4.74
Partition coefficient	$k$	0.68
Diffusion coefficient in liquid	$D_L$ (m <sup>2</sup> /s)	$1.0 \times 10^{-9}$
Diffusion coefficient in solid	$D_S$ (m <sup>2</sup> /s)	$5.0 \times 10^{-13}$
Gibbs Thomson Coefficient	$\Gamma$ (K·m)	$1.0 \times 10^{-7}$

---

\* JMatPro is a registered trademark of Sente Software, U.K

### 5.1.2 Dendritic Structure Evolution

The typical simulated dendritic microstructure evolution for directionally solidified Ni-5 wt. % Ta is shown in Figure 5.2. Simulations were performed on a regular square grid with a cell edge length of 5  $\mu\text{m}$  and the time step is chosen as 1 ms based on a sensitivity study of the computational parameters by Wang (2003) and Yang *et al.* (2004). The domain size was 3 mm wide by 4 mm high, giving a total number of 600 $\times$ 800 square cells. Periodical boundary condition was applied to both the left and right sides of the domain. A temperature gradient ( $G$ ) of 3.0 K/mm was imposed to move from the bottom to the top with a pulling velocity ( $V$ ) using the relation:  $V=100+20\times t$  ( $\mu\text{m/s}$ ) to investigate the effect of pulling velocity on solutal interaction and undercooling ahead of the growth front during directional solidification.

To simulate the chill effect near the mould wall, 100 seeds were prefixed at the bottom of the domain before simulation with their  $\langle 001 \rangle$  crystallographic orientation aligned with the vertical thermal gradient. As shown in Figure 5.2 (a), a thin layer of fine grains grew from prefixed seeds and grew into the columnar grains along the thermal gradient. During competitive growth of the columnar dendrites, only a few long columnar dendrites succeed in growing as stable columnar dendrites. The primary spacing between the columnar dendrites is not uniform but within a range which is determined by the solidification conditions and the properties of the system. This agrees with the prior simulations (Hunt and Lu, 1996) and experimental observations (Kurum, 2004; Huang *et al.* 1993) that a range of primary dendritic spacing can occur for any given solidification condition. During the growth of columnar dendrites, secondary branches began to develop from primary arms and some ternary arms initiated from secondary arms when the space became wider in the groove (Figure 5.2 (c) and (d)). These secondary and tertiary arms will interact with the primary dendrites by solute diffusion and in turn affect the local undercooling and dendrite growth which will be discussed in the following sections.

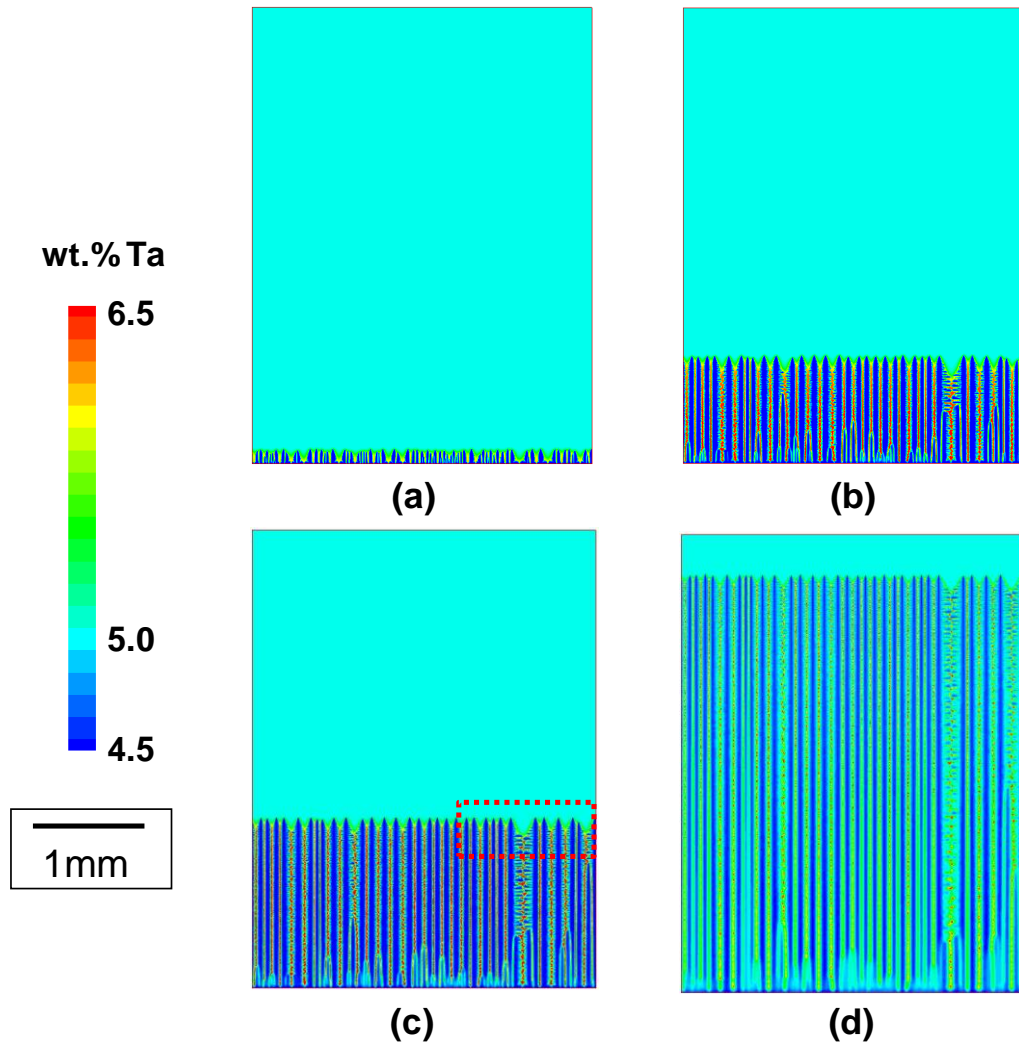


*Figure 5.2 Predicted microstructure of columnar dendrites after (a) 1; (b) 7; (c) 10; (d) 18s of growth*

### 5.1.3 Solutal Interaction within the Advancing Dendritic Network

As described in Chapter 3, the model  $\mu$ MatIC simulates solute diffusion controlled solidification. The change in the solute concentration affects the degree of undercooling and hence feeds back to the growth process during each calculating time step. In this section, the calculated solute concentration profile ahead of the growth front will be presented and the solute interaction ahead of growth front will be discussed.

Simulations in this study were performed on a  $3 \times 4 \text{ mm}^2$  domain using the same material properties and initial conditions as those discussed in Section 5.1.1. A typical detailed contour map (enlarged area in the red box in Figure 5.2 (c)) of simulated solute profile after 10 s growth is shown in Figure 5.3 (a).

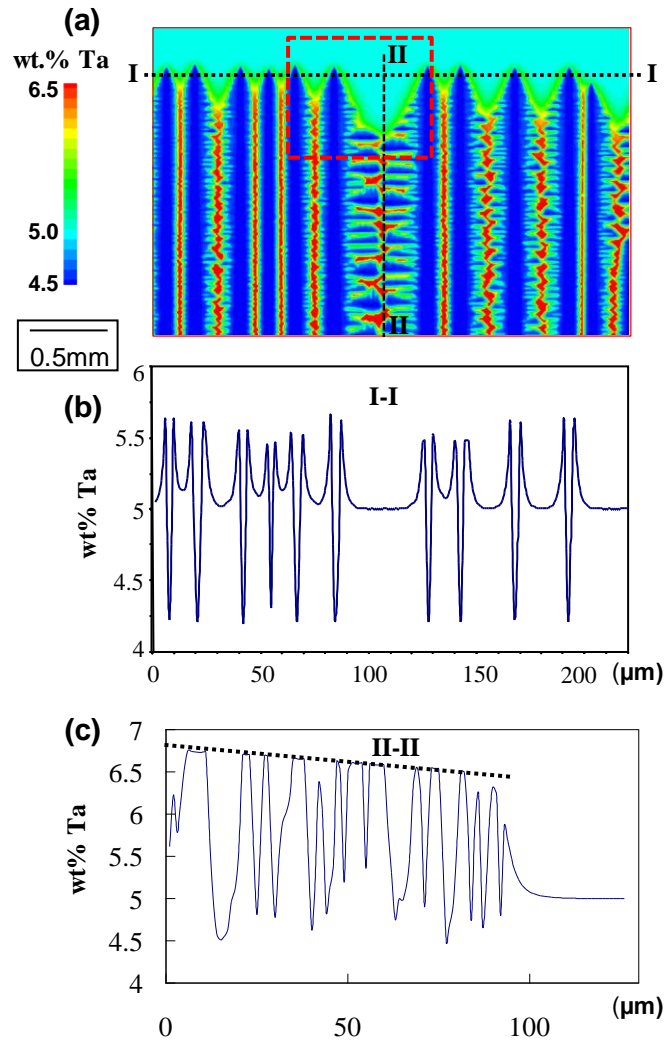


**Figure 5.3 (a) Contour map of simulated solute profiles at columnar front after 10s growth; solute concentration along line (b) I-I; and (c) II-II**

Due to the solute partitioning ( $k < 1$ ) at the solid-liquid (S/L) interface, solid has a lower concentration shown in dark blue and the S/L interfaces have a higher concentration shown in red. The solute concentration decays to the bulk liquid nominal composition

which is green. Solute variations ahead of the dendrite tips along line I-I are illustrated in Figure 5.3 (b). It can be seen that solute concentration decays exponentially from its peak value at the interface to  $C_0$  in the bulk liquid. The thickness of the diffusion layer (98% of the total solute decay) was measured for four different velocities corresponding to the dendrite structure shown in Figure 5.2 and the measured thicknesses are listed in Table 5-3. It was found that the thickness of diffusion layer decreases with the increase of growth velocity.

**Table 5-3 The thickness of the diffusion layer ahead of the advancing solidification interface**

Growth Velocity ( $\mu\text{m/s}$ )	140	220	300	460
Thickness ( $\mu\text{m}$ )	55.0	51.5	45	27.1

The solute variation in the interdendritic region between two adjacent primary dendrites along line II-II is shown in Figure 5.3 (c). The solute concentration is at a lower level when line II-II crosses the solid phase and higher when II-II crosses the liquid phase. A line was fitted to the solute concentration in the liquid regions (see dotted line in Figure 5.3 (c)), giving a slope of  $-0.67 \times 10^{-3} \text{ wt. \% } \mu\text{m}^{-1}$ . Ignoring any local curvature of the interface, Bower, Brody and Flemings (Bower, *et.al* 1966) obtained an analytical solution for the concentration gradient in liquid regions between directionally solidified dendrites:  $dC_L/dx = G/m_L$ . Substituting the value of  $G$  and  $m_L$  in this equation gives  $dC_L/dx = -0.63 \times 10^{-3} \text{ wt. \% } \mu\text{m}^{-1}$ . The difference between the prediction using  $\mu\text{MatIC}$  model and the Bower's analytical calculation is about 6%.

#### 5.1.4 Undercooling ahead of the Advancing Dendritic Network

As discussed in previous section, solute builds up ahead of the solid/liquid (S/L) interface due to the solute partitioning ( $k < 1$ ) at the interface and the limited solute diffusion in liquid ahead of the interface. An undercooled region forms ahead of the growth front. In the  $\mu\text{MatIC}$  model, the undercooling,  $\Delta T$ , in a cell is determined by the difference between the cell temperatures,  $T_{\text{Cell}}$ , and the equilibrium liquidus temperature,  $T_{\text{Liq}}(C_L)$  of the melt within the cell:

$$\Delta T = T_{\text{Liq}}(C_L) - T_{\text{Cell}} \quad (5.1)$$

The solute-adjusted undercooling corresponding to the microstructure in Figure 5.3 is plotted as undercooling iso-contours in Figure 5.4. The area of greatest undercooling is clearly shown to be the dendrite groove region rather than the region ahead of the columnar tips, as observed in prior studies (Dong and Lee, 2005). A detailed analysis of the solute adjusted undercooling along the lines A-A and B-B in Figure 5.4 (a) is shown in Figure 5.4 (b). The analysis reveals that the maximum undercooling along line A-A (in the dendrite groove) is 13.87 K, while the maximum undercooling along the line B-B (ahead of the tip) is 13.57 K. There is a 0.3 K greater undercooling in the dendrite groove region, making it the favored location for the nucleation of equiaxed grains. Once the solute fields of the secondary arms interact with each other, the composition of the liquid ( $C_L$ ) becomes similar to the local interface concentration ( $C_L^*$ ) (see line II-II) and the undercooling becomes negligible, which means that at the later stage of solidification only small constitutional undercooling exists in the remaining liquid and solid will grow at a much reduced rate in the deep grooves near the tip.

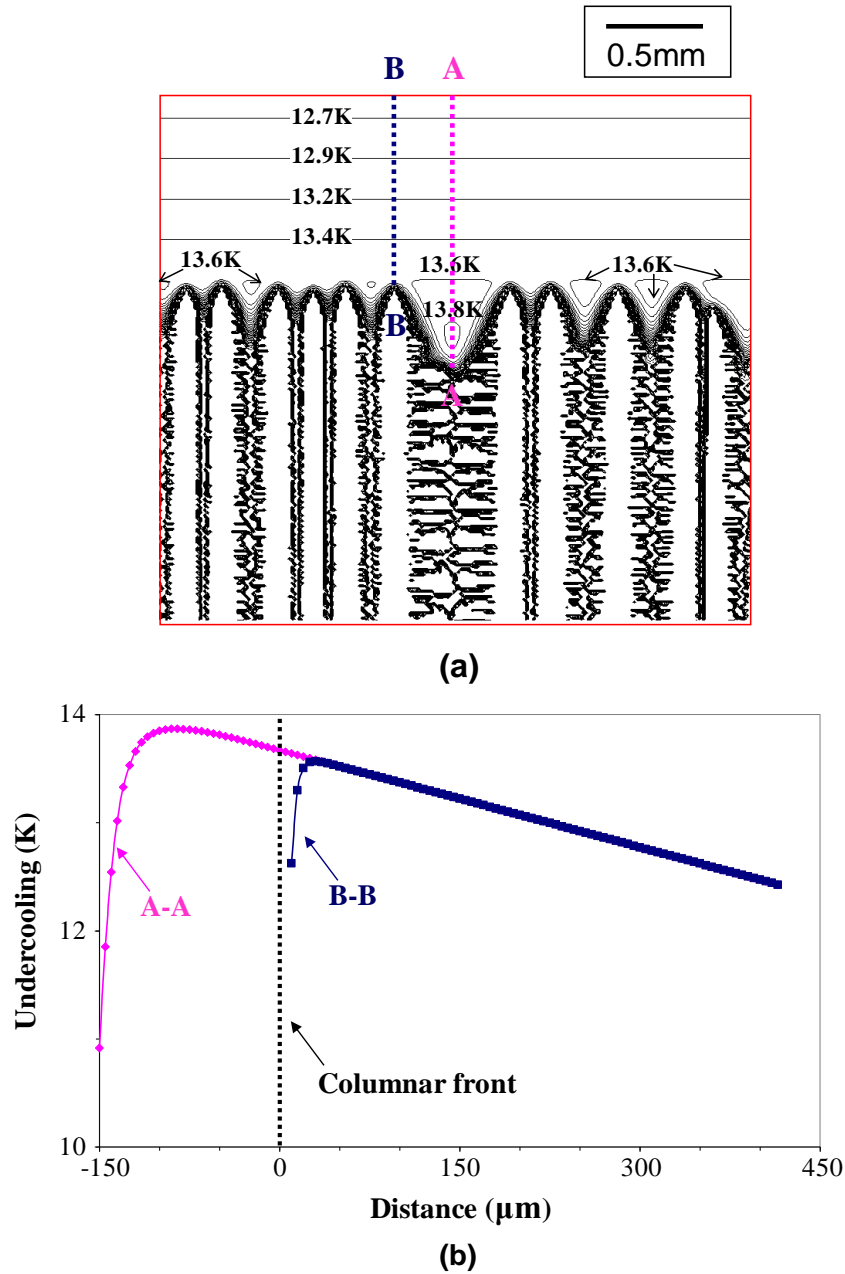


**Figure 5.4** (a) Undercooling iso-contour map of the dendrite tips after 10s growth for the structure shown in Figure 5.3(a); (b) Undercooling in liquid region along line A-A and B-B

The maximum undercooling ahead of the solidification interface for the four different pulling velocities in Figure 5.2 is plotted in Figure 5.5.

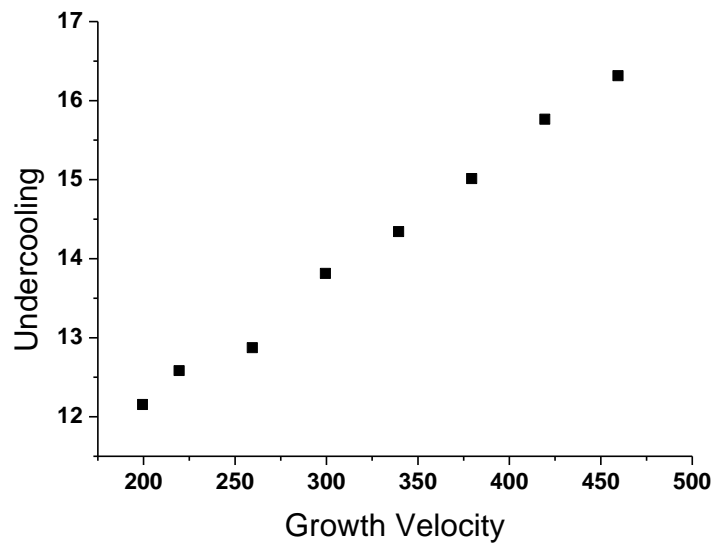


**Figure 5.5** Calculated tip undercooling as a function of growth rate using the  $\mu$ MatIC model

It shows that with the increase in growth velocity, the undercooling increases following a linearized relationship, which shows good agreement with the analytical expression predicted by Kurz and Fisher (1984),

$$v = K_{hkl} \Delta T \quad (5.1)$$

where  $K_{hkl}$  is the growth rate coefficient as a function of the dimensionless entropy and crystallographic plane for a simple-cubic, two-dimensional crystal used as a rough approximation of the behaviour of a real three-dimensional crystal.

### 5.1.5 Formation of New Grains ahead of the Advancing Dendritic Network

In order to investigate stray grain formation, nucleation and growth of new grains ahead of the solidification interface are included in this section. As discussed in Chapter 3, in  $\mu$ MatIC model the nucleation in the bulk liquid is determined stochastically to represent the essentially random process of nucleation in bulk liquid. A continuous Gaussian

nuclei distribution is used to relate the number of potential nuclei and the undercooling. In this study, mean nucleation undercooling of 13 K with a standard deviation of 1K, and the nucleus density of  $6.5 \times 10^{12}$  (nuclei/m<sup>3</sup>) were used to simulate the formation of new grains. In simulations, processing variables and material thermodynamic data were the same as the data used in previous sections.

As shown in Figure 5.6, new grains were formed firstly in the groove between the primary columnar dendrites where the undercooling was higher than the existing columnar dendrites around it and hence favours the nucleation of new grains (Figure 5.6 (a)). The newly formed grains grew at a velocity determined by their local temperature and maintained an elongated shape due to the imposed thermal gradient. Most of the news grains would be overgrown by the columnar dendrites. These kinds of grains have been observed in casting foundries and they are commonly termed “slivers” see Figure 5.7 (Jennings, 1996).

As solidification progressed, the increasing pulling velocity led to a rise of the tip undercooling ahead of the columnar dendrites and therefore offered more chance for the heterogeneous nuclei to form (Figure 5.6 (b)). The equiaxed grains formed ahead of the columnar front had greater constitutional undercooling than the existing columnar dendrites and therefore led to a quicker growth of the new grains into the equiaxed shape. Some of the equiaxed grains would overgrow the columnar dendrites and the columnar-to-equiaxed transition (CET) occurred (Figure 5.6 (c)). A parametric study on the CET will be presented in Section 5.2.

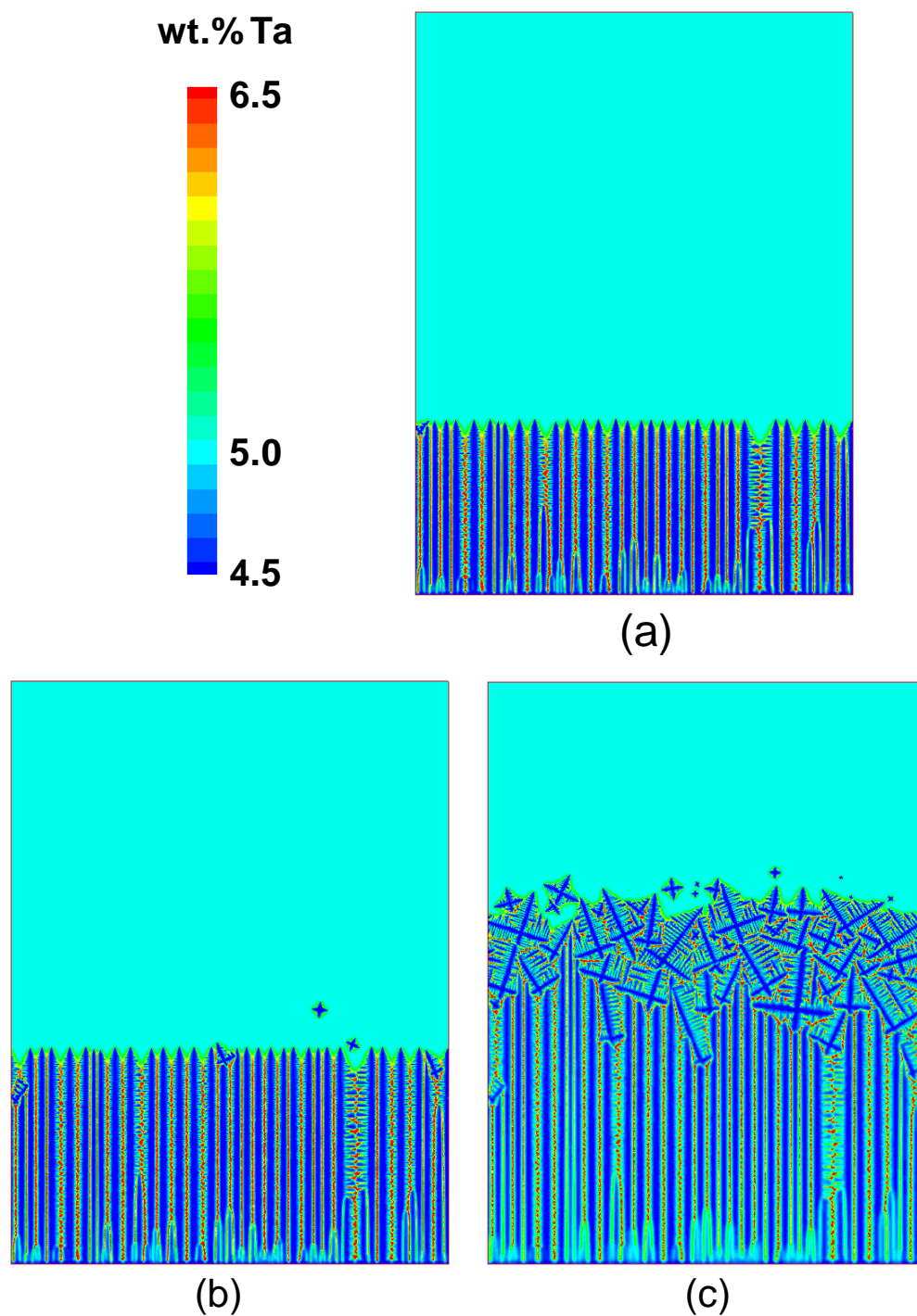


*Figure 5.6 Dendrite growth and stray grain formation during solidification after: (a) 8s; (b) 10s; (c) 14s*

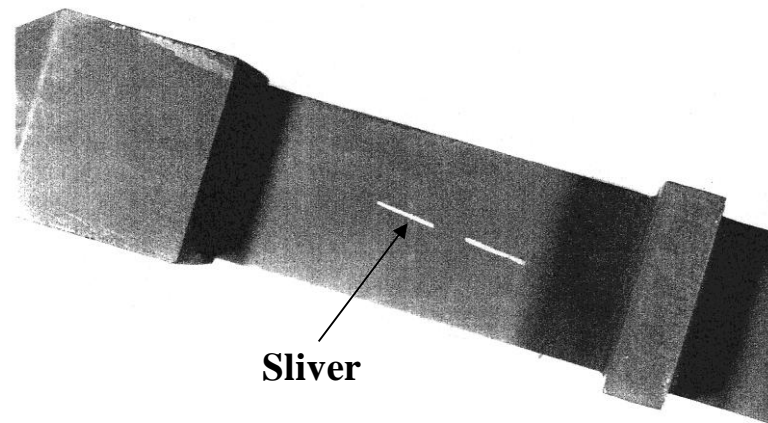


*Figure 5.7 Sliver formed in turbine blade (Jennings, 1996) (Courtesy of Rolls-Royce Plc.)*

### **5.1.6 Formation of Stray Grains in the Platform Region of Turbine Blades**

During investment casting of turbine blades, stray grains are often observed at the platform region of the turbine blades, *i.e.* at discontinuities in cross section, where cross sectional area changes lead to variations in the thermal conditions as shown in Figure 5.8.

As pointed out by Napolitano and Schaefer (2000), the general shape of the isotherm in turbine blades during investment casting is not uniform, temperature at the platform facing the downpour was observed to be higher than the temperature at the platform away from the downpour. A schematic representation of dendrite growth into the platform region at different times is shown in Figure 5.9, illustrating the high undercooling area and the dendritic patterns (Napolitano and Schaefer, 2000).



**Figure 5.8** Formation of stray grains at the platform region in IN792 turbine blades (Courtesy of Rolls-Royce Plc.)

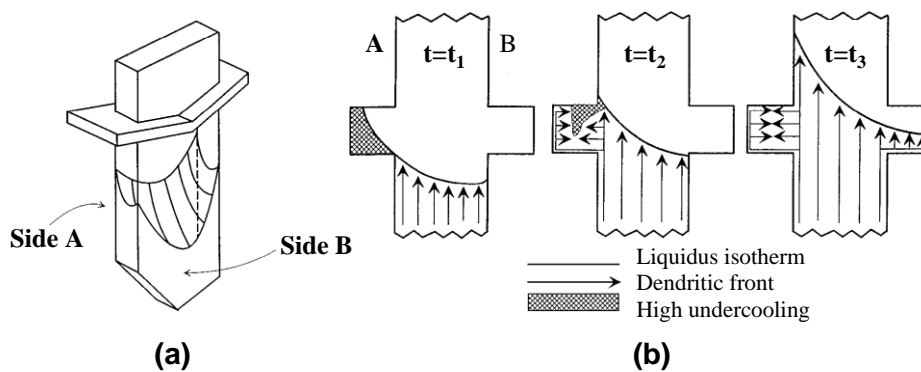


**Figure 5.9** (a) The general shape of the isotherms in turbine blades during investment casting; (b) a schematic representation of dendrite growth into the platform region at different times, illustrating the high undercooling area and the dendritic patterns due to the effect of the platform geometry and the through-thickness gradient (Napolitano and Schaefer, 2000)

New grains will form in the platform region with higher undercooling and the effect of variation in thermal gradient and pulling velocity on undercooling at the platform region has been studied by Yang (2005). It was concluded that high thermal gradient and high pulling velocity promote the formation of stray grains at the platform regions.

Recently it was observed that two alloy variants conforming to the nominal specification window of IN792 with a slight variation in C, S and N exhibit significantly different castabilities. Alloy I (C: 640 ppm, S: 8 ppm and N: 10 ppm) (referred to as BM for bad-melt in this study) showed a 10-fold greater susceptibility to the formation of stray grains in the platform than alloy II (C: 720 ppm, S: <2 ppm, N: <3 ppm) (referred to as GM for good-melt). Nominal compositions of the two alloys are listed in Table 5-4.

The calculated material properties (liquidus, solidus) using JMatPro thermodynamic phase equilibrium software are the same for the alloys BM and GM. Since processing variables are the same for the two alloys, the simulation using  $\mu$ MatIC model was not able to predict any difference between the two alloys.

**Table 5-4 Nominal composition in wt. % of alloy BM and alloy GM**

	<b>Al</b>	<b>Co</b>	<b>Cr</b>	<b>W</b>	<b>Ta</b>	<b>Ti</b>	<b>Mo</b>
BM	3.53	9.05	12.16	3.78	5.01	3.78	1.90
GM	3.50	8.89	12.16	3.78	4.95	3.78	1.84
	<b>C</b>	<b>Zr</b>	<b>Hf</b>	<b>S</b>	<b>N</b>	<b>B</b>	<b>Ni</b>
BM	0.064	0.005	<0.1	8ppm	10ppm	30ppm	BAL
GM	0.072	0.005	0.0075	2ppm	3ppm	20ppm	BAL

The question is why alloy BM showed a 10-fold greater susceptibility to the formation of stray grains than alloy GM. As described in section 5.1.4, critical nucleation undercooling may play a decisive role in the formation of stray grains during solidification. To investigate the effect of nucleation undercooling on the formation of stray grains in the two alloys, experiments were carried out to determine the critical nucleation undercoolings for these two alloys. The detailed experimental method and data analysis are given in Appendix A.

Measured liquidus temperatures ( $T_L$ ), carbide formation temperature ( $T_C$ ), solidus temperature ( $T_S$ ) and nucleation undercooling  $\Delta T_L$  are listed in Table 5-5.

**Table 5-5 Comparisons of liquidus temperature ( $T_L$ ), carbide formation temperature ( $T_C$ ), solidus temperature ( $T_S$ ) and liquidus temperature difference (nucleation undercooling  $\Delta T_L$ )**

		$T_L$	$T_C$	$T_S$	$\Delta T_L$
BM	Heating	1339.67	1302.3	1254.94	14.1
	Cooling	1325.60	1290.52	1223.41	
GM	Heating	1341.12	--	1275.06	16.4
	Cooling	1324.74	1297.45	1228.65	
JMatPro <sup>TM</sup>		1336	1327	1298	--
Ref. (Zhang and Singer, 2004)		1352	1316	1252	--
Ref. (Zhang and Singer, 2002)		1339	1315	1245	--

In the experiments, nucleation undercooling was determined by the difference between liquidus temperatures during heating and cooling. For comparison, equilibrium liquidus temperatures calculated using JMatPro are also listed in the Table 5-5, together with measured liquidus temperatures for IN792 from references (Zhang and Singer, 2004; Zhang and Singer, 2002). The liquidus temperatures deduced from the heating curves are closer in value to the temperatures calculated from JMatPro compared with the measured values from references. No difference was observed in liquidus temperatures from thermodynamic calculations for the two alloys. Experimentally determined liquidus temperatures during cooling are significantly lower than those during heating owing to nucleation undercooling. Nucleation undercooling is therefore the difference between the liquidus temperature during cooling and the liquidus temperature during heating which is listed in Table 5-5.

As shown in Table 5-5, alloy GM has a nucleation undercooling of 16.4 K, while alloy BM has a nucleation undercooling of 14.1 K. The undercooling difference between alloy GM and alloy BM is 2.3 K, thereby indicating that alloy GM needs a larger undercooling to nucleate a solid heterogeneously than alloy BM. As discussed earlier,

prior modelling results (Yang *et al.* 2004) show that this 2 K difference is all that is needed for stray grain formation in the platform region of turbine blades. Therefore for the same thermal conditions, alloy BM is more susceptible to the formation of stray grains than alloy GM, albeit the nominal compositions of the principal alloying elements are similar.

In summary, solidification structures of directionally solidified Ni-based alloys have been simulated using the  $\mu$ MatIC model. Exponential decay of solute profile ahead of the advancing front was simulated. It is found that the maximum solute-corrected undercooling exist in the grooves of the columnar dendrites and new grains will firstly form at the dendrite grooves before they appear ahead of the columnar front. The calculated results (including solute interaction and undercooling) agree well with prior analytical predictions. Formation of stray grains in the platform region of the turbine blades has also been investigated. The alloy with greater susceptibility to the formation of stray grains has lower critical nucleation undercooling, indicating that accurate materials data is in demand for accurate modelling and also the need for careful control of minor elements such as C, S and N.

## **5.2 Effects of Material Properties on Columnar-to-Equiaxed Transition**

In the previous section the formation of new grains ahead of the solidification front was examined in detail. As discussed in Chapter 2, the control of solidification structures especially the columnar-to-equiaxed transition (CET) is of great importance for the final properties of the castings. Therefore in this section a parametric study on the influence of material properties on the columnar-to-equiaxed transition (CET) will be presented.

The CET has been studied for many years via experimental and theoretical methods. The first analytical CET model was developed by Hunt and Flood (1984, 1987) using a mechanical blocking criterion. Their model was extended to rapid solidification conditions by Gaumann, Trivedi and Kurz (1986) to predict the CET during welding. Recently, microstructural models (such as cellular automaton (Gandin and Rappaz,

1984; Vandyoussefi and Greer, 2002, Dong and Lee, 2005) and phase-field (Badillo and Beckermann, 2006) have been applied to investigate the effect of solidification conditions on CET. The microstructural modelling allows individual grains to be visualized. Predicted CET for Al-Cu alloys from prior studies are summarized in Figure 5.10.

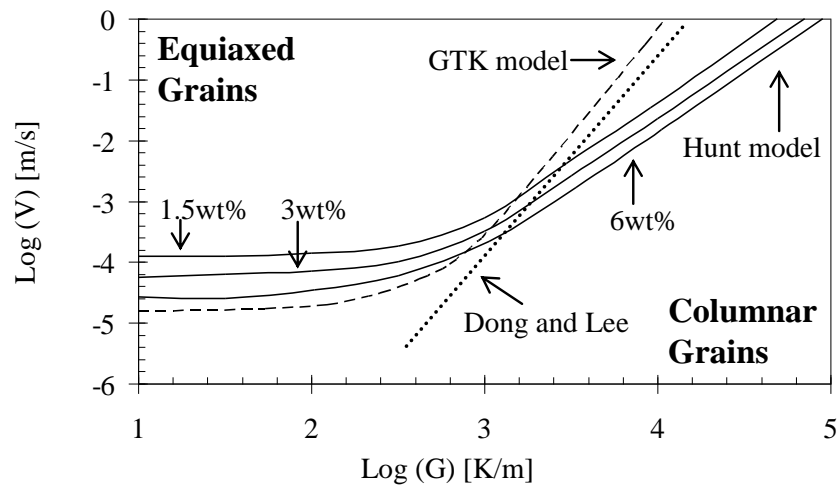


**Figure 5.10** Predicted columnar-to-equiaxed transition lines from prior models. The solid curves are the CET lines calculated using the Hunt model for Al-1.5 wt. % Cu, Al-3 wt. % Cu and Al-6 wt. % Cu alloys (Hunt, 1984). The dashed curves are the CET lines using the GTK model (Gaumann et al. 1986) and Dong and Lee's predictions (2005) for Al-3 wt. % Cu alloys.

Figure 5.10 illustrates the relationship between the processing conditions (thermal gradient and growth velocity) and solidification structure (columnar and equiaxed grains), and a reasonable agreement is obtained for the transition among different models. However, the effect of material properties on CET has not been systematically studied using microstructural modelling.

In this section the nucleation criteria including critical nucleation undercooling and the density of the nuclei in bulk liquid on the CET will be discussed first. Then the effect of alloy solidification range on the CET will be investigated and a CET map based on the

simulation results corresponding to different alloy concentrations will be finally concluded.

### 5.2.1 Simulation Parameters

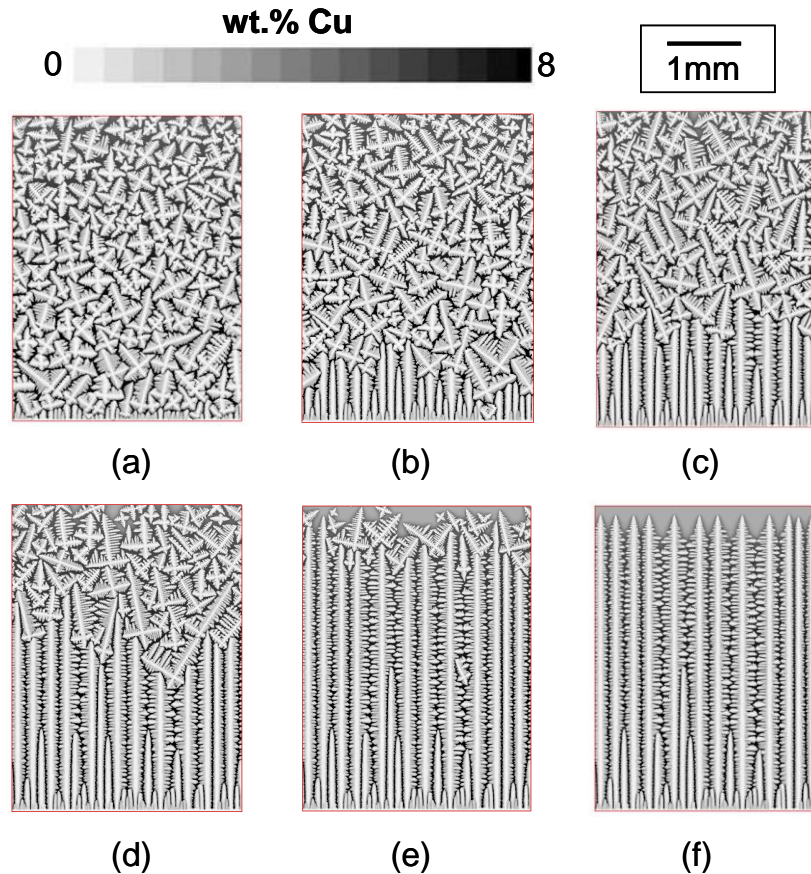
**Table 5-6 Material properties and model parameters used in the simulations**

Parameter	Symbol (Units)	Value			
		1wt%Cu	3wt%Cu	5wt%Cu	7wt%Cu
Liquidus temperature	$T_L$ (K)	930.4	925.4	920.3	915.3
Solidus temperature	$T_S$ (K)	906.5	863	829.2	812.2
Liquidus slope	$m_L$ (K/wt%)	-2.653	-2.717	-2.729	-2.742
Solidus slope	$m_S$ (K/wt%)	-27.31	-27.65	-27.45	-27.01
Partition coefficient	$k$	0.09716	0.09825	0.09942	0.10105
Diffusion coefficient in liquid	$D_L$ (m <sup>2</sup> /s)	$3.4 \times 10^{-9}$			
Diffusion coefficient in solid	$D_S$ (m <sup>2</sup> /s)	$D_S^{Cu} = 4.8 \times 10^{-5} \exp(-16069/T)$			
Gibbs Thomson Coefficient	$\Gamma$ (K·m)	$1.0 \times 10^{-7}$			

Simulations presented in this section correspond to Al-Cu alloys. This is because Al-Cu alloys are the typical model alloys which are widely used for CET modelling and model validations. The objective of this study using  $\mu$ MatIC model is to facilitate a better understanding of material properties on CET and therefore the typical Al-Cu alloys are used. The material properties and processing parameters are listed in Table 5-6 and the phase diagram data is generated from MTDATA (Davies *et al.* 1990).

### 5.2.2 Effect of Critical Nucleation Undercooling

Representative contour maps of simulated solute concentration with different critical nucleation undercoolings for an alloy Al-3 wt. % Cu after 18 s growth are shown in Figure 5.11. The domain size was 3 mm wide by 4 mm high, giving a total number of 600×800 cells. Temperature gradient ( $G$ ) of 3.0 K/mm was imposed to move from the bottom to the top with a pulling velocity ( $V$ ) using the relation:  $V=100+20 \times t$  ( $\mu$ m/s) to simulate the thermal profile in directional solidification.



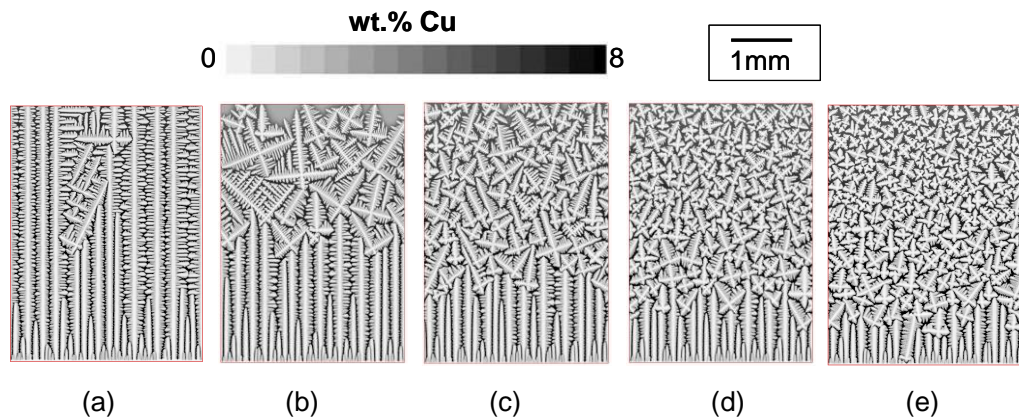
**Figure 5.11** Effect of critical nucleation undercooling on the CET, for a range of mean nucleation undercooling: (a) 3K; (b) 4K; (c) 5K; (d) 6K; (e) 7K; (f) 8K

Figure 5.11 illustrates the influence of critical mean nucleation undercooling on the CET. In Figure 5.11 (a) and (b), small mean nucleation undercoolings were used to simulate the inoculation effect in casting (by adding effective inoculant particles into melt before casting). Equiaxed grains formed immediately from a thin layer of fine columnar grains near the surface. A reduction in grain size was also observed with the decrease of critical nucleation undercooling from Figure 5.11 (d) to Figure 5.11 (a). This agrees with prior analytical predictions (Greer *et al.* 2000) that inoculant particles become active at an undercooling inversely proportional to the particle diameter. In Figure 5.11 (c) and (d), the mean nucleation undercoolings were set to 5 K and 6 K. The microstructure evolution of the CET was illustrated clearly and the CET occurred at a later stage with a higher growth velocity ( $V=100+20\times t$  ( $\mu\text{m/s}$ )) when the critical nucleation undercooling increased. The CET can be seen in Figure 5.11 (e) with a mean

undercooling of 7 K. It happened at a very late stage with a high pulling velocity until the undercooling reached the critical limitation. In Figure 5.11 (f), an arbitrary high mean nucleation undercooling of 8 K was used to simulate solidification with difficulty in heterogeneous nucleation. In this case, no equiaxed grains can be formed within the range of velocities tested.

### 5.2.3 Effect of Nuclei Density in Bulk Liquid

Different densities of nuclei in bulk liquid are used in this section to investigate the effect of nuclei density on the CET (see Figure 5.12).



**Figure 5.12** Effect of nuclei density in bulk liquid on the CET, for the maximum nuclei density of: (a)  $6.5 \times 10^{10}$ ; (b)  $6.5 \times 10^{11}$ ; (c)  $6.5 \times 10^{12}$ ; (d)  $6.5 \times 10^{13}$ ; (e)  $6.5 \times 10^{14}$  (nuclei/m<sup>3</sup>)

Density of nuclei in bulk liquid varies from  $6.5 \times 10^{10}$  (nuclei/m<sup>3</sup>) (Figure 5.12 (a)) to  $6.5 \times 10^{14}$  (nuclei/m<sup>3</sup>) (Figure 5.12 (e)). Simulations illustrate that the CET is promoted for the melt with a high density of nuclei. With the increase in maximum nuclei density in bulk liquid, more equiaxed grains are nucleated when the critical nucleation undercooling is reached and in turn leads to a finer grain size in casting. This is compatible with experimental observations that inoculation of the melt with heterogeneous nuclei promotes the CET (Greer *et al.* 2000).

### 5.2.4 Effect of Alloy Solidification Range

The effect of alloy solidification range is explored by varying alloy concentrations in a model alloy Al-Cu system (material properties shown in Table 5-6). As shown in Figure 5.13, when the concentration of Cu changes from 1 wt. % to 5 wt. %, the solidification range varies from 22 °C to 90 °C.

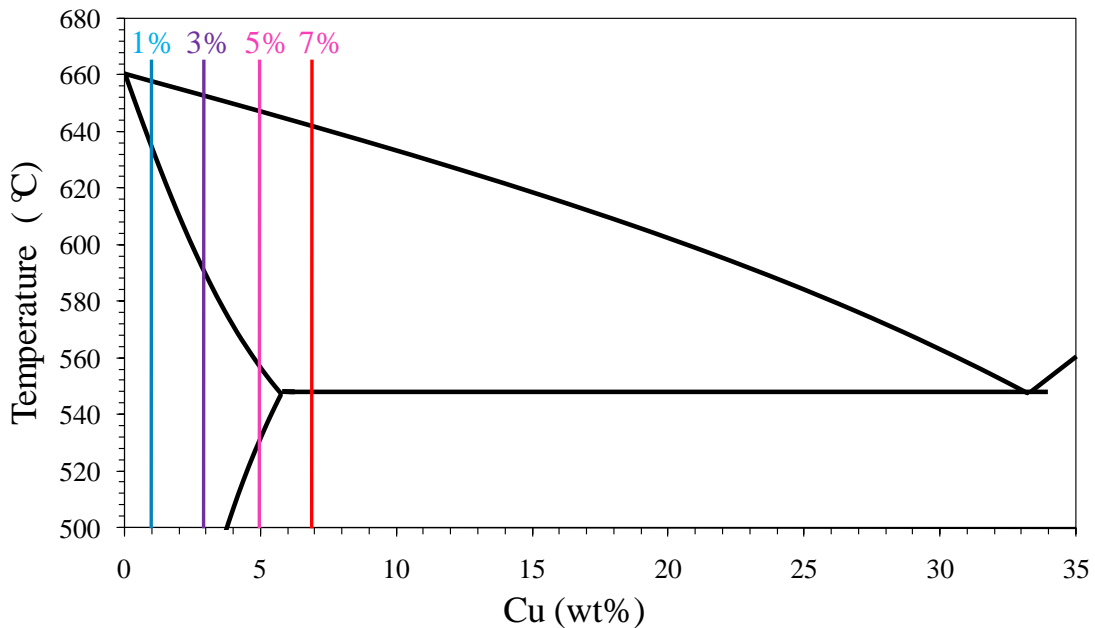


**Figure 5.13** Solidification ranges for different alloy concentrations in Al-Cu phase diagram

Figure 5.14 illustrates the CET maps based on the simulated results corresponding to different alloy concentrations. Simulated grain structures are indicated by using different symbols: The open symbols stand for the equiaxed grains and filled symbols stand for columnar grains. The approximate CET lines separating the equiaxed and columnar regions are plotted in the maps as well, illustrating the dependence of the CET on the thermal gradient ( $G$ ) and pulling velocity ( $V$ ) for different alloy concentrations. It can be found that for the same alloy, equiaxed grain structure occurs at low thermal gradient and high pulling velocity, whereas, columnar grain structure exists at high thermal gradient and low pulling velocity.

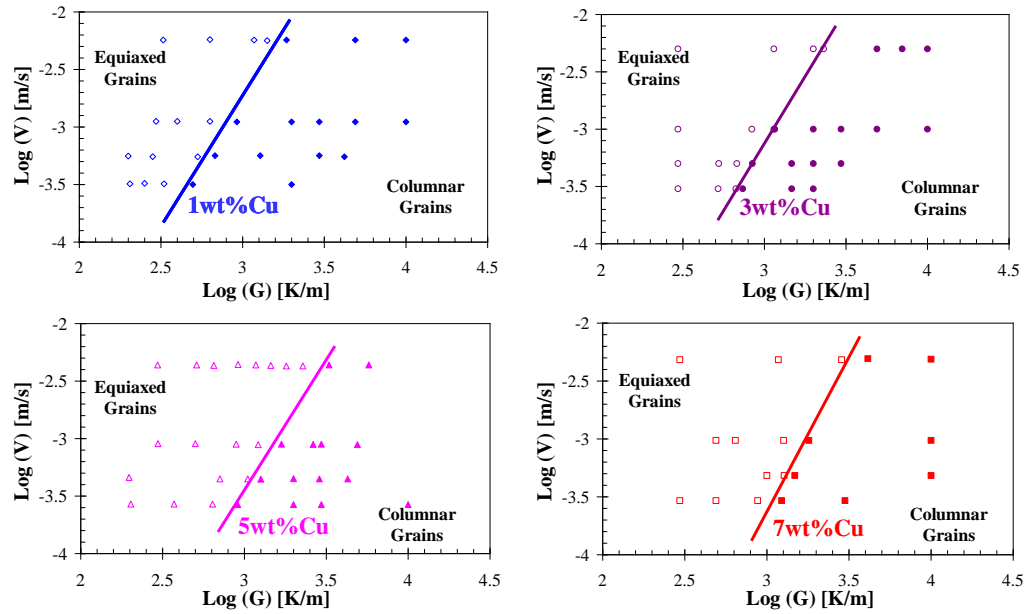


**Figure 5.14** Progress maps showing the effect of alloy solidification range on the CET: open and filled symbols indicate equiaxed and columnar grains for (a) Al-1wt%Cu; (b) Al-3wt%Cu; (c) Al-5wt%Cu; (d) Al-7wt%Cu. The solid lines are the approximate CET lines separating the equiaxed and columnar regions.

Simulated results reveal that extending the alloy solidification range leads to an increased tendency to the CET. The reason is that for alloy with higher solute concentration, more solute will be ejected and accumulated in the S/L interface (when  $k < 1$ ) and in turn increase both the magnitude and the area of the constitutional undercooling ahead of the columnar front. The simulated results match well with prior experimental observations on the CET for Al-2wt%Cu and Al-4wt%Cu (Siqueira *et al.* 2002).

In summary, the effects of material properties on columnar-to-equiaxed transition (CET) have been simulated. Simulated results reveal that the CET can be promoted by: (1) decreasing the critical nucleation undercooling; (2) increasing the nuclei density of the melt; and (3) extending the solidification range.

## **Chapter 6      The Influence of Dendrite Packing Patterns on Primary Spacing Adjustment during Solidification**

During directional solidification of single crystal turbine blades, the primary dendrite arm spacing affects both the propensity for casting defects and the final mechanical properties. Cross sectional changes lead to variations in the thermal conditions; the rate at which the primary spacing adjusts to these changes has a significant influence on the nucleation and growth of potential stray grains. In this chapter, a three-dimensional (3D) solutal dendrite  $\mu$ MatIC model will be applied to visualize the complexity of cross section views of directionally solidified structures. Then a comparison of dendrite structure and solute interaction between 2D and 3D simulations will be discussed. Using the typical Al-Cu system as an example, the influence of dendrite packing patterns (cuboidal or regular hexahedral) on primary spacing adjustment during directional solidification will be investigated. Finally, the importance of stereological effects on the modelling of the growth of solutal dendrites will be discussed.

### **6.1 3D $\mu$ MatIC Model**

As discussed in Chapter 5, the 2D  $\mu$ MatIC model was capable of visualising the detailed dendritic structures and providing a new insight into complex solute interaction during solidification. However, neither the complexity of cross section views of directionally solidified structures, nor the effect of dendrite packing (cuboidal or regular hexahedral) can be revealed using the 2D model. Therefore, the 2D model was extended to 3D to study the dendrite structure and solute concentration in 3D and to compare the predicted results with previous 2D modelling results.

Similar to the 2D model, the 3D simulation domain is discretized into a regular grid of cubic cells. Both the nucleation and solute diffusion of the model use the same cubic cell and time step. The growth algorithm is extended to a decentred octahedron algorithm in order to maintain the preferred growth crystallographic  $\langle 001 \rangle$  directions of

cubic metals during solidification. The nucleation algorithm used in the 3D  $\mu$ MatIC model is the same as that used in the 2D model which has been described in Chapter 3.

## 6.2 Comparison between 2D and 3D Simulations

In order to compare with the previous simulation results in Sections 5.1 and 5.2 for dendritic growth in single-crystal turbine blades, the same material properties and model parameters (shown in Table 5-2) are applied in the 3D model. In this section, predicted dendrite structures using the 2D and 3D models under the same casting conditions will be presented first. Then the solute distributions within the advancing dendritic network in 2D and 3D simulations will be analysed.

### 6.2.1 Simulated Structure Evolution using 2D and 3D $\mu$ MatIC Models

Typical simulated 2D and 3D dendrite structures for a directionally solidified Ni-5 Wt. %Ta alloy are shown in Figure 6.1. The 3D domain size was  $1 \times 1.5 \times 1 \text{ mm}^3$ , giving a total number of  $200 \times 300 \times 200$  cells and the 2D domain size was  $1 \times 1.5 \text{ mm}^2$  with  $200 \times 300$  cells. The same casting conditions were applied for 2D and 3D simulations: (a) an imposed thermal gradient ( $G$ ) of 3000 K/m; (b) a constant pulling velocity ( $V$ ) of 100  $\mu\text{m/s}$ ; (c) a zero flux boundary condition for all sides of the domain; (d) prefixed seeds at the bottom of the domain with one of their  $\langle 001 \rangle$  preferred growth directions aligned with the vertical thermal gradient and a uniform primary spacing of 300  $\mu\text{m}$ ; (e) heterogeneous nucleation not included to avoid the stray grain formation.

As illustrated in Figure 6.1 (a), solidification starts from the prefixed seeds at the bottom. During solidification (shown in Figure 6.1 (b)-(c)), primary columnar dendrites grow along the direction of heat flux (thermal gradient) and secondary and tertiary arms have developed. The developed secondary and tertiary arms interact with each other in terms of solute diffusion. As discussed in Section 5.1.2, the solute is partitioned between solid and liquid phases. For the element Ta ( $k < 1$ ), the solid phase, which is the dendrite region, has a lower concentration (shown in blue colour). While in the solid/liquid (S/L) interface, Ta concentration is high (shown in red colour), and decays

to the bulk liquid (shown in green colour). Compared with 2D simulations, 3D dendrite structure has less blue colour region in the dendrites which means the average solute concentration is higher than in the 2D simulation. In the simulation, the same average concentration of Ta is used in 2D and 3D and the difference in contour map is because the surface of the 3D domain does not cut through the centre of the dendrites which contains less solute. The surface we see is the interdendritic region and therefore it has a high solute concentration which is shown in red colour.

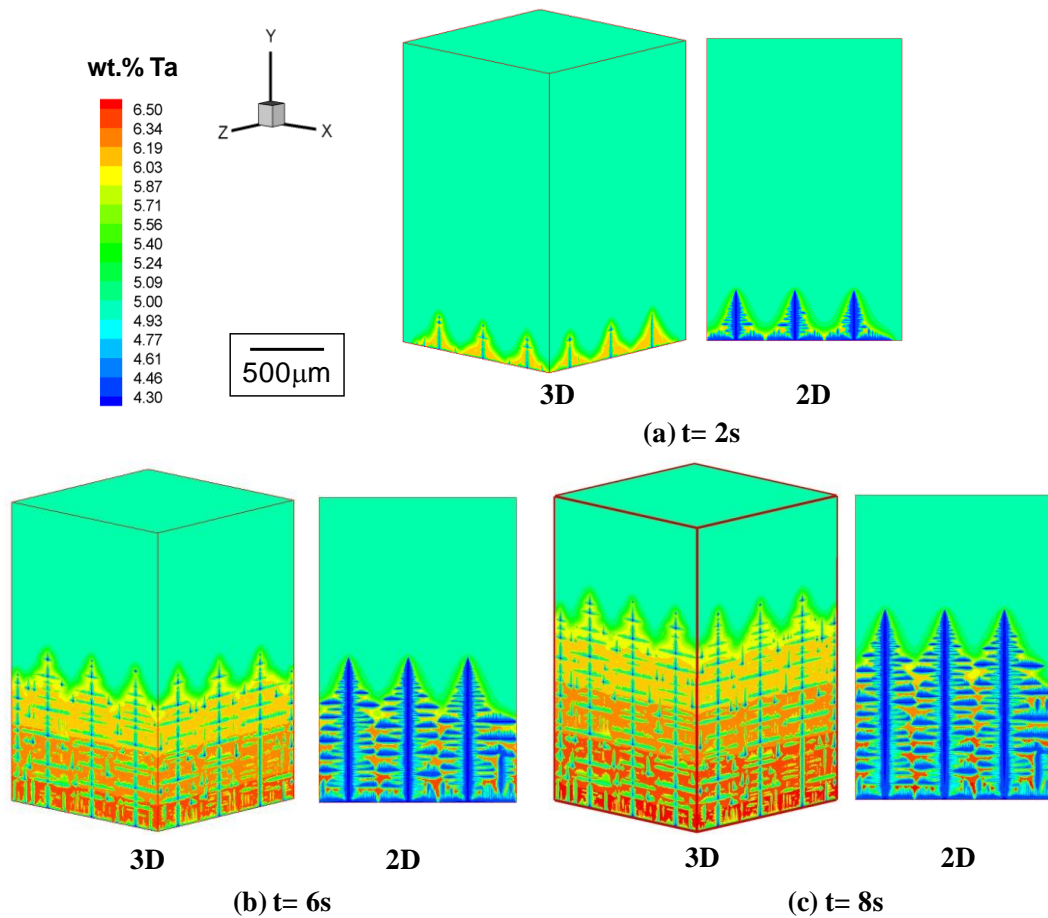


**Figure 6.1** Simulated dendrite structures in 3D and 2D at: (a)  $t=2s$ ; (b)  $t=6s$ ; (c)  $t=8s$

Considering the 3D effect, to investigate the internal structure between two dendrites, longitudinal section views (X-Y plane) of the 3D simulation at different positions from the core of one columnar dendrite to the core of its next neighbour are shown in Figure

6.2. For comparison, the 2D simulation with the same casting conditions is also illustrated (Figure 6.2 (m)).

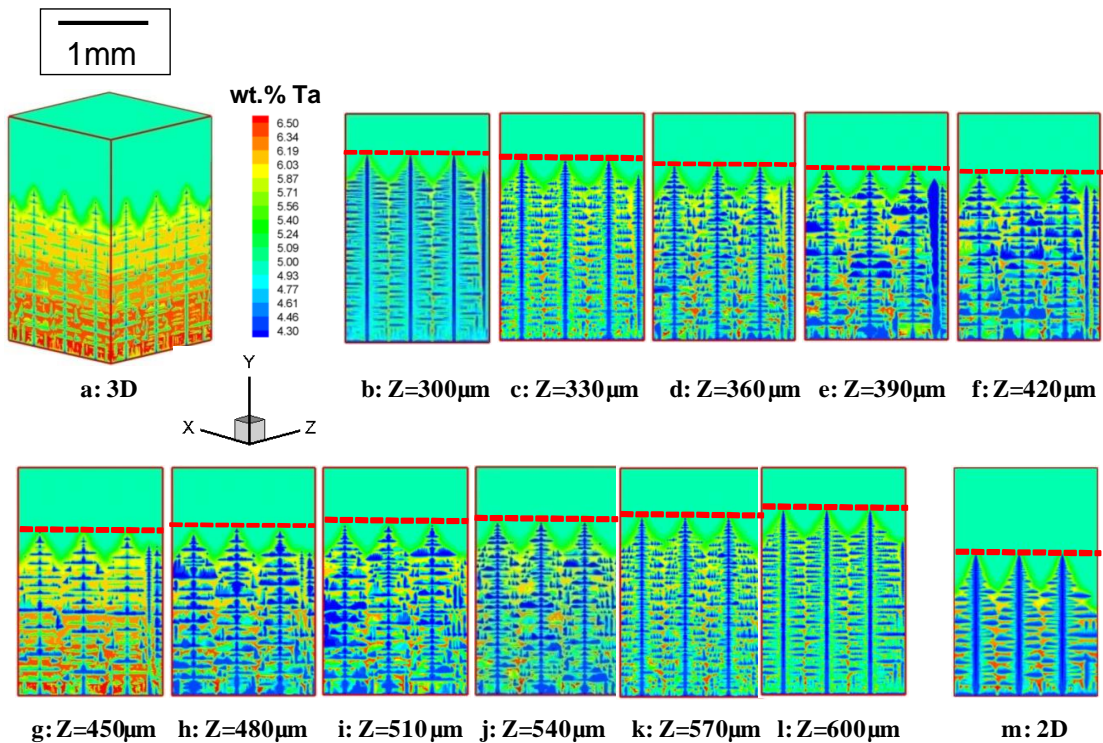


**Figure 6.2** Solute contour maps of: (a) 3D dendrite structure after 8s; (b-l): longitudinal sections (parallel to X-Y plane) between two adjacent dendrite cores in 3D simulation; (m) 2D dendrite structure

In Figure 6.2 (b) and Figure 6.2 (l), the longitudinal sections are cut through the 3D dendrite cores, and Figure 6.2 (g) shows the structures at the midway between the two cores. The distance of the cutting sections along Z axis is indicated in the figure. It can be seen that the parabolic shape of the dendritic tip is developed and the initiation, growth and selection of secondary and tertiary dendrite arms are simulated. It is noteworthy that the heights of primary dendritic tips are different, *e.g.* the height is 1100 μm in the dendrite core (Figure 6.2(b)) and 980 μm in the middle of the interdendritic region (Figure 6.2(g)). The parabolic dendrite shape in each longitudinal section and the difference between the dendritic tip heights represent a paraboloid shape of dendrite morphology in 3D. Some ‘broken’ pieces exist between dendrites in some sections

(shown in Figure 6.2(b)-(k)). These are not 'isolated' grains but are secondary and tertiary branches originating from the primary dendrites. Compared with 3D simulation, the dendrite structure in 2D (shown in Figure 6.2(m)) has a similar morphology to the dendrite core in 3D but with a much lower height of the columnar front (760  $\mu\text{m}$ ). According to the imposed thermal profile ( $G=3000$  K/m), this difference in height provides a temperature difference of 1 K ( $3000$  K/m  $\times 0.00034$  m) in the columnar dendrite front. Since the simulation was performed with a constant pulling velocity, the steady state was maintained in both 2D and 3D. Therefore, larger undercooling is required to grow dendrite in 2D simulation compared with 3D simulation.

The longitudinal section views of the 3D simulation also illustrate the complex solute concentration within the advancing dendritic network. The dendrite core shows a dark blue colour with low concentration of Ta (Figure 6.2(a) and (l)) while the groove between two dendrites shows a gradual colour change from red to green (Figure 6.2(b) and (k)), illustrating the solute diffusion layer within the dendritic network. The solutal interactions in 2D and 3D simulations will be compared in the next section and the mechanism for the difference in solute diffusion will be further analysed.

### **6.2.2 Solutal Interactions within the Advancing Dendritic Network in 2D and 3D Simulations**

Figure 6.3 shows solute concentration ahead of the columnar dendrite fronts along the isothermal line perpendicular to the withdrawal direction. The results are extracted in the longitudinal section at the dendrite core of the 3D simulation (shown in the red curve) and 2D analysis (shown in black curve) is shown in this figure for comparison. Since the solute partitioning of Ta ( $k=0.68$ ) is less than 1, solute is pushed away from the solid to the S/L interface and enriched in the liquid ahead of the interface. An exponential profile from the interface to the bulk liquid is revealed, which agrees with Burden and Hunt's analytical model (1974). It is worthy of note that the solute concentration between two dendrites has decayed to the bulk liquid level. This means the distance between two adjacent columnar dendrite tips is wide enough for the rejected solute to diffuse to the bulk liquid. Therefore there is no interaction between the

primary dendrite tips and the growth of primary dendrites at the tip in this simulation can be treated as isolated from each other. Compared with 2D simulation, the results show that the 3D model predicted a lower solute concentration at the interface. As discussed earlier, smaller undercooling is required in 3D simulations compared with that in 2D due to the lower solute concentration profile in the liquid interface in 3D. Also, the solute diffusion layer at the dendrite tip in 3D is found to be thinner than in 2D. The possible explanation is as follows: (a) the solute concentration in liquid interface in 3D is lower which provides a smaller solutal gradient in the liquid region; (b) the rejected solute has more directions to diffuse at S/L interface in 3D than in 2D and thus requires a smaller distance and a shorter time.

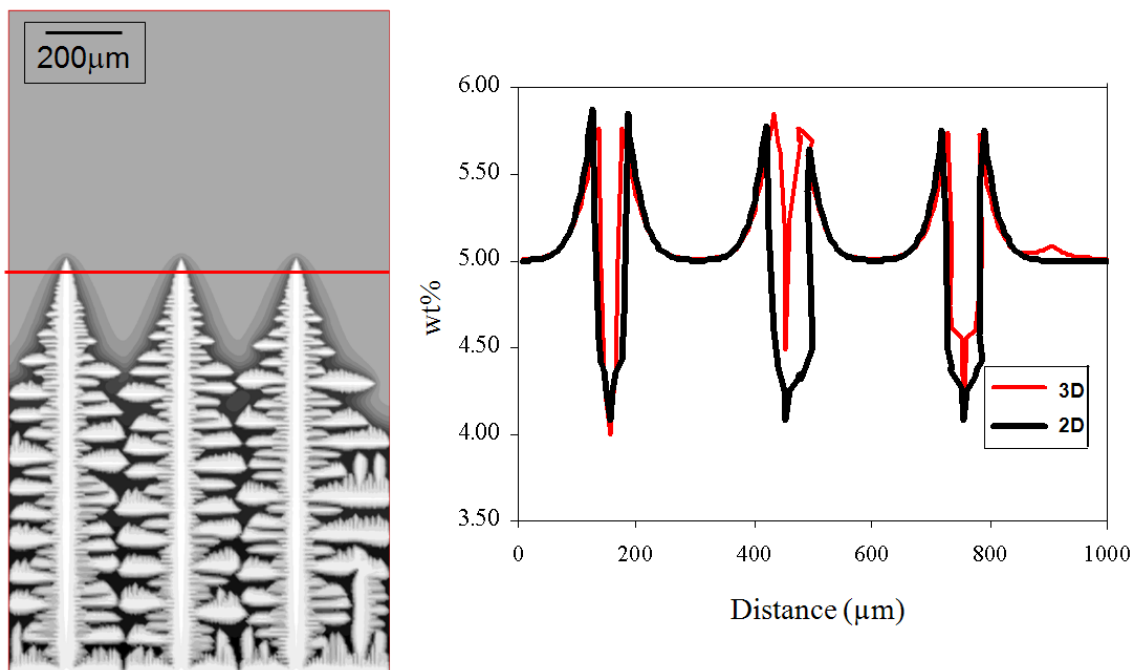


**Figure 6.3** A comparison of solute concentration ( $C_E$ ) at dendrite tips along isothermal line in 3D through dendrite centre and 2D

Solute profiles within the interdendritic region along the dendrite growth direction are shown in Figure 6.4. To examine the complex solutal interaction in the dendrite groove in 3D, solute profiles at different longitudinal sections from the dendrite core ( $Z=300$  μm) to the midway between dendrites ( $Z=450$  μm) are illustrated in Figure 6.4(b) and the 2D simulation is shown for comparison in Figure 6.4(c).

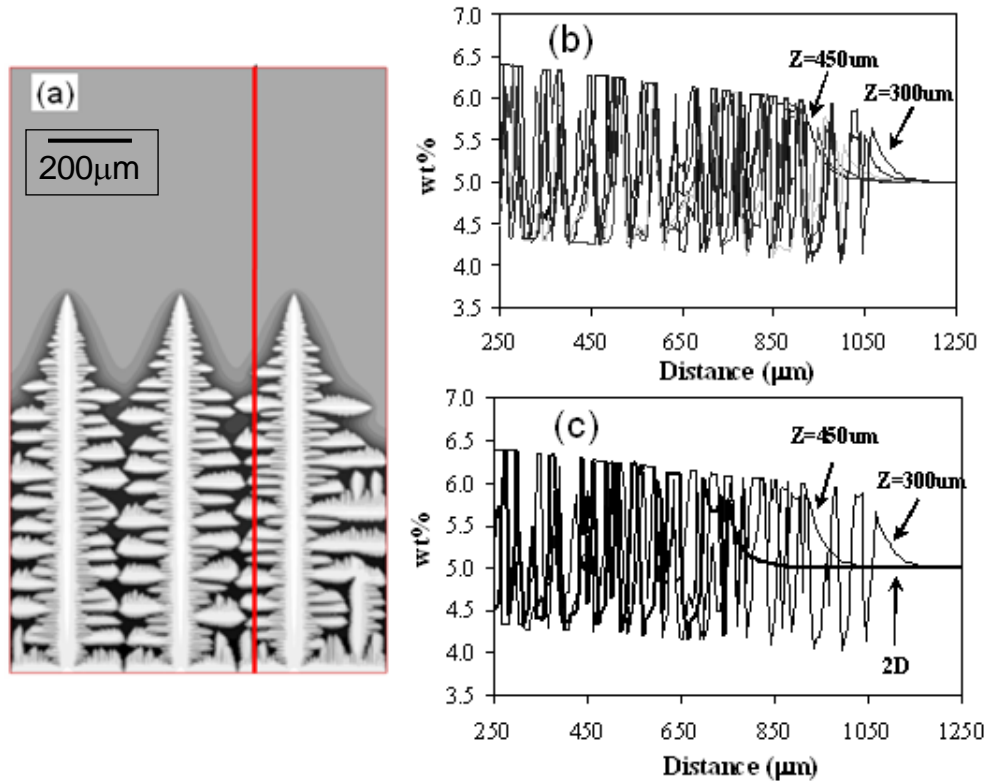


**Figure 6.4** Solute concentration along dendrite growth direction in the interdendritic region for 3D ( $Z=300 \mu\text{m}$  to  $Z=450 \mu\text{m}$ ) and 2D simulations (2D simulations are superimposed in (c))

As illustrated in Figure 6.4, solute concentration is at a low level ( $C_S$ ) when the line crosses solid phases and at a high level ( $C_L$ ) when it crosses the liquid groove between the dendrites. It is found in the 3D simulation that the solute concentration maintains the same level at the same height for all the sections at different positions. This indicates that strong solutal interaction exists among diffusion fields of secondary arms and possibly tertiary arms and they cannot be treated as isolated from each other. However, the lengths of diffusion layers at the columnar front in 3D highly depend on the distance from the dendrite cores. In the dendrite centre ( $Z=300 \mu\text{m}$ ), the growth front is  $1120 \mu\text{m}$  and the diffusion layer length is about  $70 \mu\text{m}$ . While between the two dendrite tips ( $Z=450 \mu\text{m}$ ), the diffusion layer length is  $105 \mu\text{m}$ . The solutal interaction in the interdendritic region is much stronger than that at the dendrite core. Compared with 3D results, the predicted S/L interface in 2D is behind that in 3D. In the liquid region, a

similar solute gradient (shown with the dashed red line) is observed and is consistent between the 2D and the 3D simulations.

Figure 6.5 shows a quantitative comparison of the calculated solute profile at a dendritic tip between the 2D and 3D  $\mu$ MatIC models. The figure reveals that the solute gradient is a strong function of direction. Compared with 2D simulations (shown with the red line), solute concentration at the S/L interface in the 3D simulation (shown with the pink line) is lower. Meanwhile, the diffusion distance in the 3D simulation is smaller since the solute has more directions to diffuse in the 3D simulation during solidification.

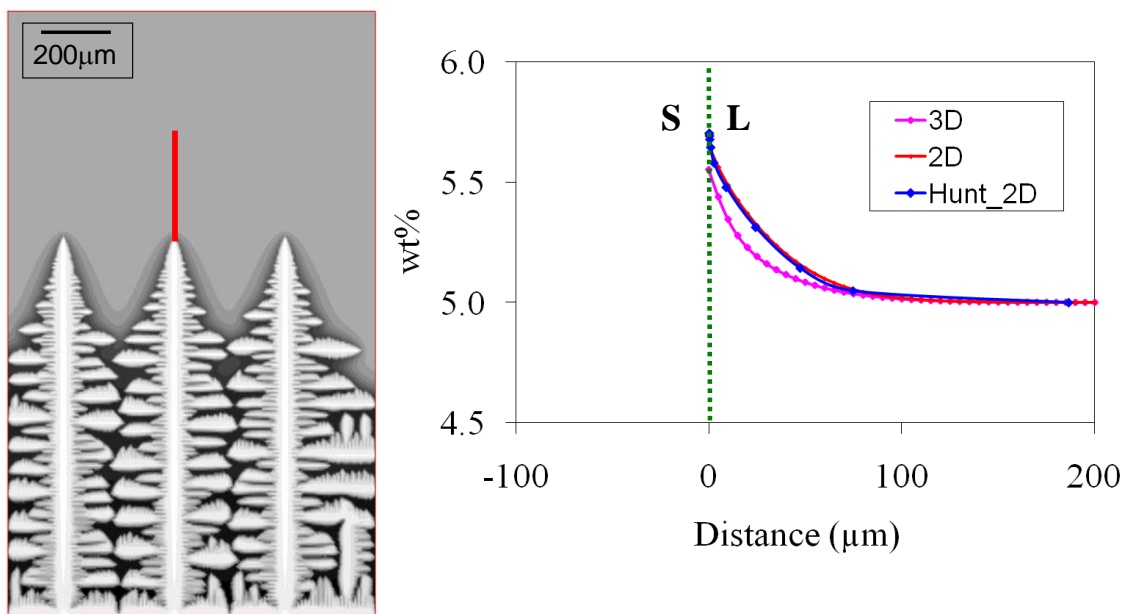


**Figure 6.5** *Quantitative comparison of calculated solute profile ahead of dendrite tip using 2D and 3D  $\mu$ MatIC models and Hunt's 2D model*

The calculated concentration profiles using the Hunt 2D model (Hunt and Lu, 1996) are plotted (shown with the blue curve) to compare with that obtained using the 2D  $\mu$ MatIC model. The same conditions were used in both models with a primary spacing of 300  $\mu$ m. As shown in Figure 6.5, the calculated solute concentration profiles from the 2D  $\mu$ MatIC model agree well with those obtained from the Hunt 2D model, with the largest discrepancy occurring near the S/L interface. At the interface, the Hunt and Lu model predicted a solute concentration of 5.71 wt%, while the  $\mu$ MatIC model gave 5.65 wt%, giving an error of 1.1%. This variance is due to the cell size difference at the S/L

interface between the two models. In the Hunt 2D model an adaptive cell size was used, with a size of  $0.1346 \mu\text{m}$  for the cells along the S/L interface while in the  $\mu\text{MatIC}$  model the cell size of  $5 \mu\text{m}$  was applied. The  $\mu\text{MatIC}$  model uses a weighted average:  $C_L = C_L^*(1-f_s) + C_s f_s$  to calculate the solute concentration in the growing cell and the calculated concentration is averaged over a large volume as illustrated in Figure 6.6, resulting in a lower peak value. It should be noted that the difference is due to the liquid concentration adopted in the diffusion solver.

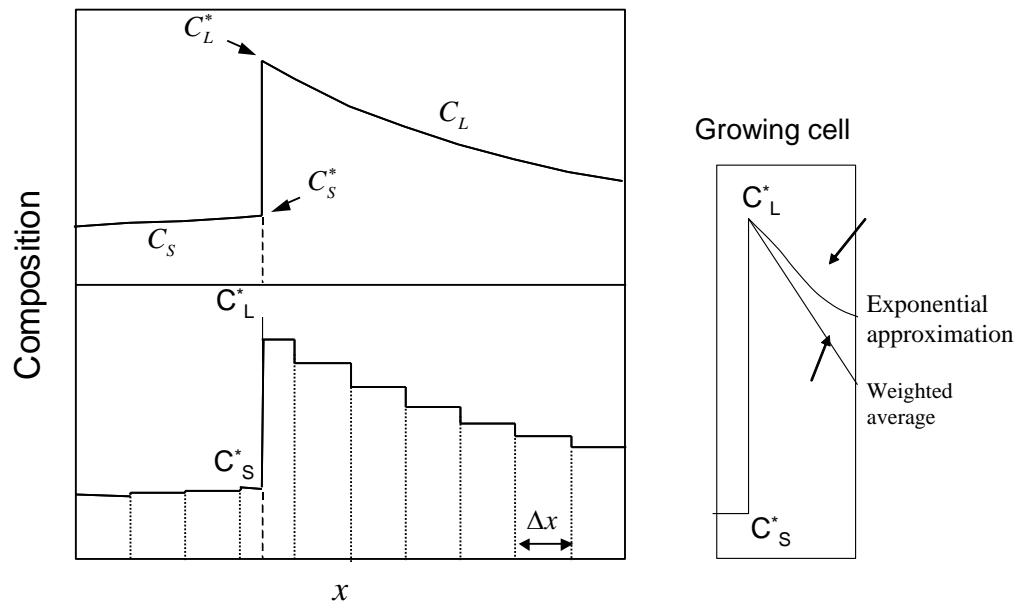


**Figure 6.6** A schematic illustration of the solute distribution profile ahead of advancing solidification interface and the solute concentration at the wall of a growing cell.

Recently Yi, Dong and *et al.* (2008) have investigated the solute concentration approximation in the growing cell in solidification modelling. In their study, an exponential approximation was used to calculate the solute concentration cell by assuming an exponential composition profile ahead of the solid/liquid interface in the growing cell as shown in Figure 6.6. The exponential profile is determined using following equation:

$$C_L = \frac{C_L^* - C_L^{i-1} \exp(-P)}{1 - \exp(-P)} \quad (6.1)$$

where  $C_L^{i-1}$  is the solute concentration in the adjacent cell. For a given component, the *Peclet* number in the growing cell is given by:

$$P = V \times \Delta x / D_i \quad (6.2)$$

where  $V$  is the growth velocity in previous time step,  $\Delta x$  is the cell size and  $D_i$  is the diffusion coefficient for the given component at the current temperature.

Their results reveal that the weighted average approximation has lower solute concentration at the wall (this is equivalent to the liquid concentration used in  $\mu$ MatIC model) than that using exponential approximations. Further improvement in solute diffusion can possibly be achieved by either applying this exponential approximation or reducing the cell size, but more computing resources and computational time will be needed for simulation.

Although there may be inaccuracies in the solute diffusion calculation due to the large cell size, the solute profile ahead of the S/L interface is quantitatively correct with an error less than 1.1%. Furthermore, this quantitative error has previously been shown to be consistent, correctly predicting primary spacing over a wide range of growth rates and thermal gradients (Wang *et al.* 2003) and the relative diffusion profile ahead of the solid/liquid interface is correct.

The above solute analyses conclude that a complex diffusion profile exists at different stages of solidification. In 3D simulations, the length of diffusion layers around the tip is shorter than that behind the tip, and strong solute interactions occur among the diffusion fields of secondary arms and tertiary arms. Compared with 3D simulation, the length of diffusion layers at the tip in 2D simulation is longer and therefore leads to a slower dendrite growth rate and a larger constitutional undercoolings ahead of growth front.

### 6.3 Effect of Packing Patterns on Primary Spacing Adjustment during Solidification

In 2D simulations, every columnar dendrite has two nearest neighbouring dendrites, while in 3D simulations it can have more than two nearest neighbours depending on the packing pattern in the cross section. As shown in Figure 6.7, if the columnar dendrites have a cuboidal packing pattern, every dendrite will have 4 nearest neighbours; if the columnar dendrites have a more closely packed hexahedral pattern, every dendrite will have 6 nearest neighbours. Therefore the interaction between the dendrites will be much more complex in 3D simulations.

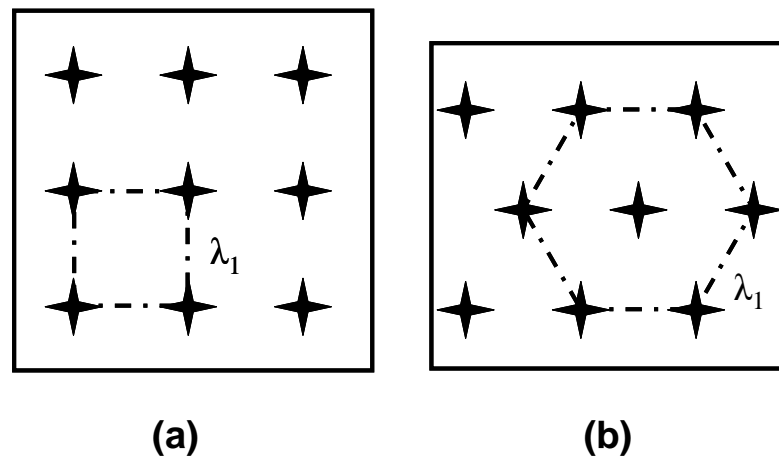


*Figure 6.7 Prefixed seeds with the primary spacing of  $\lambda_1$  at the bottom of the simulation domain: (a) square and (b) hexagonal configuration*

In this section, the model alloy Al-3 wt. % Cu (material properties see Table 5.2) will be used to investigate the influence of packing patterns on primary spacing adjustment during directional solidification. Predicted dendrite structures and the branching of secondary and tertiary dendrite arms will be presented first using the 3D model. Then the rate at which the primary dendrite spacing adjusts via branching in response to the growth velocity changes will be studied for cuboidal and hexahedral packed crystals. Finally, the effect of packing patterns on the castability and solution heat treatment from a commercial view will be further discussed.

### 6.3.1 Branching

Typical contour maps of alloy concentration for a directionally solidified Al-3wt% Cu alloy are shown in Figure 6.8. The size of the 3D domain was chosen as 1.5 mm wide, 2 mm high by 1.5 mm thick, giving a total number of  $300 \times 400 \times 300$  cells. Nine seeds with a primary spacing ( $\lambda_1$ ) of  $500 \mu\text{m}$  were prefixed at the bottom of the domain as an initial condition (see Figure 6.8 (a)), and their  $\langle 001 \rangle$  crystallographic orientation was aligned with the vertical thermal gradient ( $G$ ). The thermal gradient used in the simulation was  $3.0 \text{ K/mm}$ , and the pulling velocity ( $V$ ) varied as a function of simulation time ( $t$ ) following the relation:  $V = 150 + 20 \times t \mu\text{m/s}$ . To avoid the formation of new grains during simulation, the mean nucleation undercooling was arbitrarily set to a high value of  $50 \text{ K}$  with a standard deviation of  $0.5 \text{ K}$ .

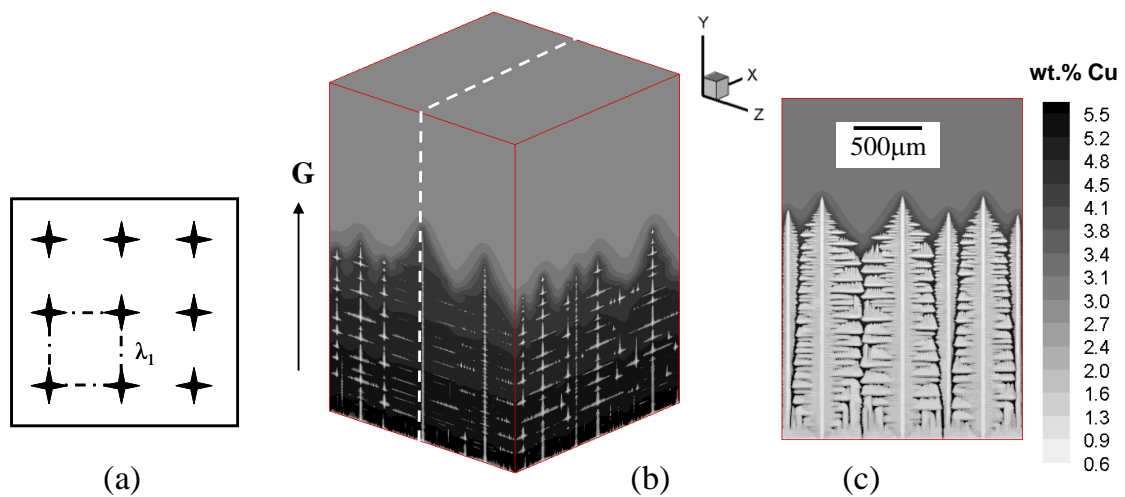


**Figure 6.8** (a) Prefixed seeds at the bottom of the simulation domain; (b) simulated 3D dendritic structure after 6 seconds of growth; (c) a longitudinal section view along the  $x$ - $y$  plane as indicated in (b)

Figure 6.8 (b) shows a simulated contour map of alloy concentration at the external surface of the computational domain. Figure 6.8 (c) is a longitudinal sectional view which is cut through the centre of dendrite along the  $x$ - $y$  plane as indicated in Figure 6.8 (b), showing the internal dendrite structures. Due to the solute partitioning at the S/L interface ( $k < 1$ ), the solid phase has a lower solute concentration and therefore it is

shown as lighter regions in the contour plot; while the liquid ahead of the S/L interface has a higher solute concentration and therefore appears as darker regions in the counter plot. As illustrated in Figure 6.8 (b) and (c), the dendrite structure and branching can be clearly seen during directional solidification. The primary dendrites grow from the prefixed seeds at the bottom and secondary arms developed between the primary dendrites. Since the spacing between primary dendrites is wide enough, tertiary arms start to initiate from some of the secondary arms and grow in the same direction of the primary dendrites. The competition of growth between the secondary and tertiary arms is determined by the local undercooling. Tertiary arms can eventually survive and catch up with the primary dendrites if their growth rates are higher than those of their neighbouring secondary arms, which enable the tertiary arms to escape the growing secondary arms and continue to grow as primary dendrites.

### 6.3.2 Effect of Packing Patterns on Primary Spacing

As discussed above, the primary dendrite arm spacing ( $\lambda_1$ ) adjusts via branching in response to changes in processing conditions. In this section, the influence of dendrite packing patterns (cuboidal or hexahedral) on primary spacing adjustment will be studied.

Figure 6.9 illustrates isotropic 3D contour maps of simulated dendrite structures for square-packed and hexagonal-packed seeds, as well as the cross section views intersecting the columnar dendrites along the solidification length: A<sub>1</sub>-A<sub>1</sub>, B<sub>1</sub>-B<sub>2</sub> at Y = 1300  $\mu\text{m}$  (top section) and down to A<sub>4</sub>-A<sub>4</sub>, B<sub>4</sub>-B<sub>4</sub> at Y = 50  $\mu\text{m}$  (bottom section).

At Y=1300  $\mu\text{m}$ , the tips of primary dendrite stems and secondary arms can be seen. In cross section A<sub>1</sub>-A<sub>1</sub>, there are 18 primary dendrite tips, of which 9 are grown from the pre-fixed seeds and 9 are tertiary arms originated from secondary dendrites, giving an average final dendrite spacing of 364  $\mu\text{m}$ . In cross section B<sub>1</sub>-B<sub>1</sub>, there are 29 primary dendrite tips, of which 9 are grown from the pre-fixed seeds and 20 are tertiary arms originated from secondary dendrites, giving an average final dendrite spacing of 264  $\mu\text{m}$ . Compared with the square packing, there are 11 more dendrite tips in the hexagonal packing and in turn leads to much finer average dendrite arm spacing during

solidification. The reason can be explained as follows: as illustrated in Figure 6.10, the red crosses stand for the possible tertiary branches. These tertiary branches are originated from the second arms so their locations must align with the direction of secondary arms. The dendrites packed in the hexahedral packing pattern have more open space for secondary arms to grow and therefore give more opportunities for the tertiary arms to subsequently develop as primary arms, resulting in a finer primary spacing during solidification.

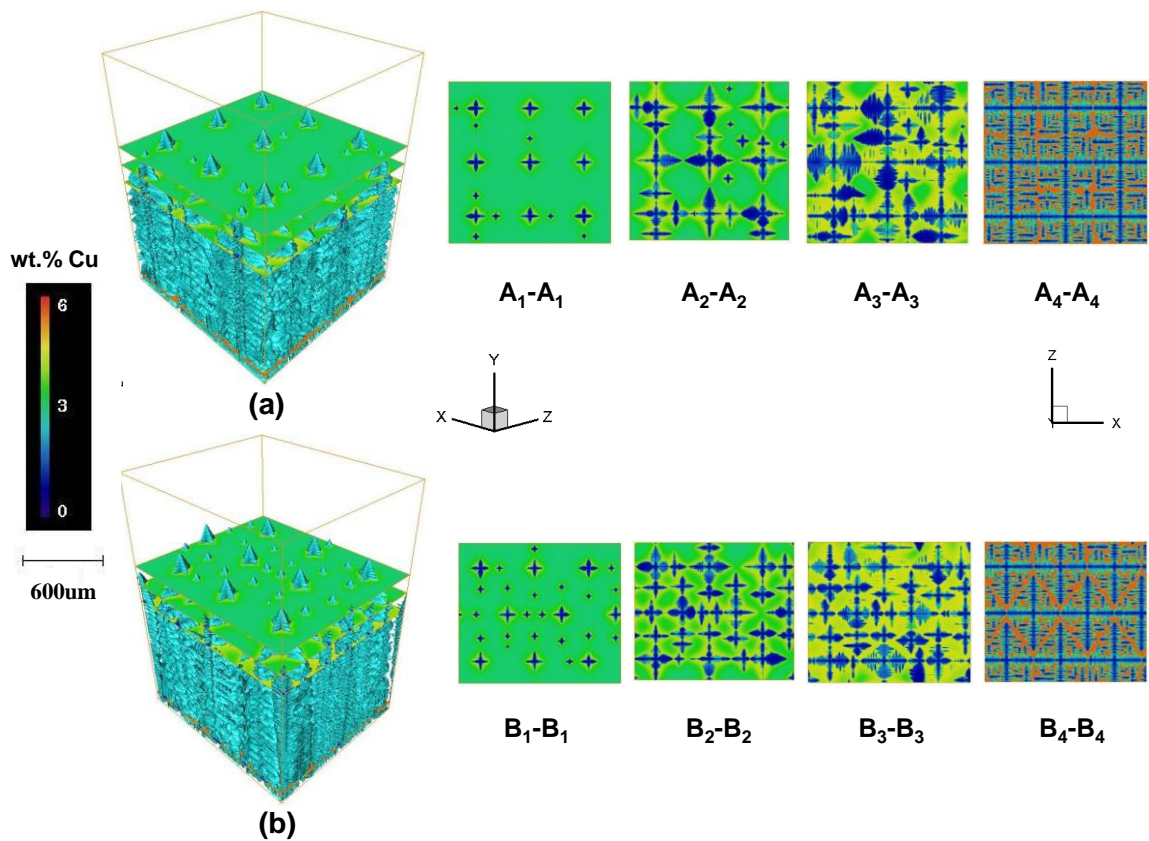


**Figure 6.9** Simulated 3D dendritic structures grown from seeds with (a) square configuration and (b) hexagonal configuration after 6 s of growth; cross section views at different heights for dendrites packed in a square pattern – A1-A1, B1-B1 ( $Y=1300 \mu\text{m}$ ), A2-A2, B2-B2 ( $Y =1150 \mu\text{m}$ ), A3-A3, B3-B3 ( $Y =1000 \mu\text{m}$ ) and A4-A4, B4-B4 ( $Y=50 \mu\text{m}$ ).

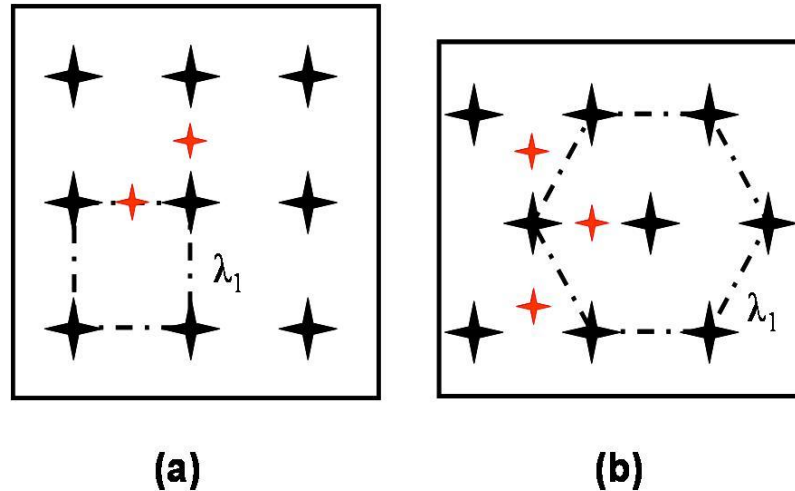


**Figure 6.10** Schematics of tertiary branches developed from secondary arms during solidification in (a) square and (b) hexagonal packing configuration

Simulation results reveal that it is easier for dendrites packed in a hexahedral pattern to adjust their primary arm spacing during solidification than dendrites packed in a cuboidal pattern. For directional solidification components, the primary spacing ( $\lambda_1$ ) characterizes the maximum length scale for the segregation of alloying elements. Therefore, a fine spacing is sought to reduce the time for solution heat treatment and to improve mechanical properties.

At  $Y=1150 \mu\text{m}$  (shown in  $A_2-A_2, B_2-B_2$  in Figure 6.9), primary and secondary arms grew into the liquid and solute interaction occurred between primary arms. The solute interaction in dendrites packed in the hexahedral pattern was stronger than that in the square pattern and in turn presents a thicker diffusion layer in the liquid region. At  $y=1000 \mu\text{m}$  (shown in  $A_3-A_3, B_3-B_3$ ), some tertiary arms were fully developed as primary dendrites. At the bottom cross section of  $y=50 \mu\text{m}$ , 9 dendrites growing from prefixed seeds were shown in both cases.

To illustrate the solute interaction between the dendrites during solidification, enlarged views of solute contour maps at the cross section of  $Y=1000 \mu\text{m}$  for both cuboidal and hexahedral packing patterns are shown in Figure 6.11.



smaller than that in cuboidal packing, and thereby can reduce the propensity for the formation of new grains during solidification.

**Table 6-1 Comparison of solute concentration, grain density, average primary spacing and solidification range between cuboidal and hexahedral packing patterns**

	Grain Density ( $\text{m}^{-3}$ )	Average Spacing ( $\mu\text{m}$ )	Solute Concentration		Solidification Range
			$C_{Max}$	$C_{Min}$	
Cuboidal	10.2E6	364	6.67	0.39	90.5
Hexahedral	15.9E6	264	5.77	0.39	78.5

Different packing patterns result in different solute segregations which can in turn lead to different solidification ranges. In casting, solidification range is a decisive criterion and it is related to the difference between the initial temperature ( $T_{Ini}$ ) and end temperature ( $T_{End}$ ) as illustrated in Figure 6.12. Small solidification range can reduce the potential for forming casting defects, such as hot tearing (Chojecki *et al.* 1997). As listed in Table 6-1, the solidification range for hexahedral packing is 78.5 K, 12 K smaller than that for cuboidal packing, leading to a less propensity for defect formation during casting.

## 6.4 Summary

A 3D  $\mu\text{MatIC}$  model is used to study the dendrite structure evolution and solutal interaction during directional solidification in 3D. Compared with 2D simulations, dendrites in 3D have similar morphology but grow at higher rate. Solute diffusion layer at the dendrite tip in 3D is found to be thinner than in 2D and therefore leads to a smaller constitutional undercooling ahead of growth front and a higher dendrite growth rate. Simulation results also reveal that solute interactions among the diffusion fields of secondary arms and tertiary arms in 3D is stronger than that in 2D.

Using the 3D  $\mu\text{MatIC}$  model, the influence of dendrite packing patterns (square and hexagonal) on primary spacing adjustment during directional solidification was investigated. It is found that dendrites packed in hexahedral pattern can adjust their

primary spacing more easily than dendrites packed in square pattern. An important implication of this finding is that during directional solidification and single crystal growth, if crystals grow from seeds with hexagonal packing pattern, then finer primary spacing can be achieved in the crystals, resulting in a reduced propensity for the formation of defect grains and a shortened time for solutioning heat treatment.

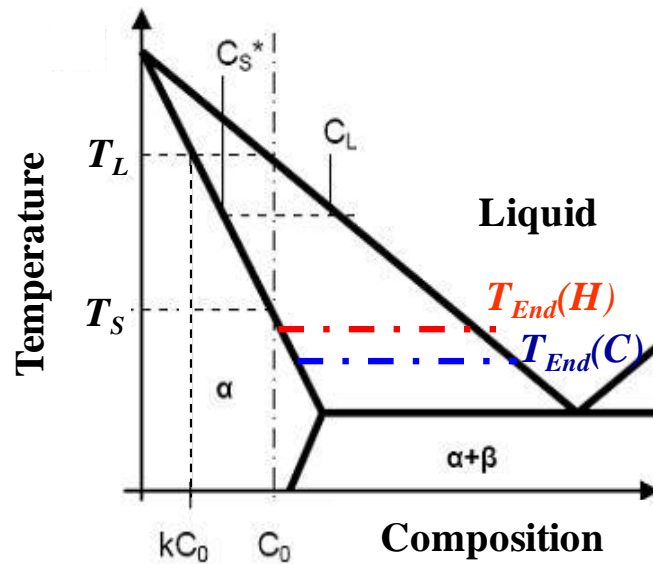


*Figure 6.12 (a) Solute concentration at the S/L interface and the corresponding undercooling for square and hexagonal packing configuration; (b) effect of dendrite packing pattern on the solidus temperature in the schematic linearized binary phase diagram*

## **Chapter 7      Conclusions and Future Work**

Multi-scale modelling method of solidification was applied during the course of this work to study the solidification structure across different orders of magnitude of scales. On the macroscopic scale, a Finite Element casting model, ProCAST is implemented to obtain thermal and flow profiles. The predicted thermal and flow data are then used as inputs in a grain structure model (CAFE) on the meso-scale to investigate grain selection in single crystal grain selector. On the micro-scale, detailed dendrite structures and complex solutal interaction during solidification are predicted using a dendritic model ( $\mu$ MatIC).

The conclusions drawn from this study are presented in this chapter, together with recommendations for future work.

### **7.1 Conclusions**

#### **7.1.1 Grain Selection during Investment Casting of Single Crystal Turbine Blades**

This work was the first attempt to systematically study the effect of spiral design on the grain selection in single crystal (SX) grain selector. Simulation and experimental results reveal that the spiral is used to quickly but randomly select one grain for single crystal blades and its efficiency can be improved by choosing a smaller wax wire diameter, a larger spiral diameter and a smaller take-off angle.

By comparing the simulated results with experimental observations, we propose that grain inside of the spiral is selected by geometrical control mechanism. Therefore, the design (geometry and dimension) of the grain selector could make a significant contribution to the improvement of the productivity for single crystal casting.

This study reveals that we can move away from a purely empirical choice of grain selector to the one which is designed and optimised. The results of this study on the

spiral design will result in reduced rejection rates, increased performance through a better control of crystal orientation and significantly reduced component costs.

### **7.1.2 The Formation of New Grains ahead of the Advancing Solidification Front**

Formation of new grains ahead of the advancing solidification front was investigated by analysing the solute distribution and associated undercooling using the micro-scale  $\mu$ MatIC model. It was found that the maximum solute-corrected undercoolings exist in the grooves of the columnar dendrites, which will be the most favourite region for new grains to form. Simulation results also reveal the importance of the alloy critical nucleation undercooling on the susceptibility to the formation of new grains. A 2.3 K reduction in critical nucleation undercooling was found to be able to lead to a 10-fold greater susceptibility to the new grain formation for Ni-based superalloy IN792.

The effects of material properties on the formation of new grains, such as columnar-to-equiaxed transition (CET), were quantified using a model alloy Al-Cu. It was found that the CET can be retarded by: (1) increasing alloy critical nucleation undercooling; (2) decreasing the density of nuclei in the melt; (3) shortening the alloy solidification range. These conclusions can be used as guidelines in casting foundries for developing and selecting alloys to minimise stray grain formation in turbine blades.

### **7.1.3 The Influence of Dendrite Packing Patterns on Primary Spacing Adjustment during Solidification**

A 3D  $\mu$ MatIC model was applied to further investigate the complexity of solute interaction at the cross sections of the directionally solidified structures. Compared with 2D simulations, solute diffusion layer at the dendrite tip predicted in 3D was found to be thinner than that in 2D, therefore leading to a smaller constitutional tip undercooling and a higher dendrite growth rate. Simulation results also revealed that solute interaction among the diffusion fields of secondary arms and tertiary arms in 3D is

stronger than that in 2D because solute has more dimensions to diffuse during solidification.

Two different packing patterns (cuboidal and hexahedral) were used in the study. The influence of dendrite packing patterns on primary spacing adjustment during directional solidification was investigated. It was found that branching in the hexahedral packing pattern is easier than that in the cuboidal packing, leading to faster adjustment to the change in thermal conditions and a concomitant smaller average spacing. An important implication of this finding is that during directional solidification and single crystal growth, if crystals grow from seeds with hexagonal packing pattern, then a finer primary spacing can be achieved in the crystals, resulting in a reduced propensity for the formation of defect grains and a shortened time for solutioning heat treatment.

## **7.2 Future Work**

Based on the results of the study and conclusions drawn from them, the following recommendations are made for the future work.

The systematic study of the grain selection in the spiral selector not only made a comprehensive investigation on the spiral design and optimisation for the improvement of the single crystal casting process, but also pointed out the importance of the new design of the grain selector. The proposed geometrical control mechanism facilitates a better understanding of the grain selection in the spiral. In the spiral, the grain selection is through competitive growth (overgrowth and branching) between dendrites. By simulating the overgrowth and branching using the detailed micro-scale dendritic model  $\mu$ MatIC, the competition among primary, secondary and tertiary dendrites were discussed. This provides a deep inside into the solute interaction and growth competition and indicates that the growth of the secondary arms could have a valuable impact on the grain selection during solidification. New designs of the SX grain selector such as a fine cone selector would be worth studying to improve the efficiency and accuracy of the grain selection. Also, a grain selector which is capable to select

secondary arm orientations will be desirable to further improve the quality of the SX turbine blades.

A patent has been applied for a crystal pattern selector based on packing pattern study. In this study, it was indicated that dendrite packing pattern has a remarkable influence on the final primary spacing, defect formation during casting and the following heat treatment time. If crystals grow from a hexahedral pattern selector, then the crystals can have finer solidification structures with improved mechanical properties. Laboratory-scale trials are needed to validate the predicted results and to provide guidelines for industry to explore this new technique.

## **Appendix A: Measurement of Nucleation Undercooling during Solidification of the Ni-based Superalloy, IN792**

To identify the effect of minor alloying elements on the formation of HABs in the Ni-based superalloy IN792 (see Section 5.1.6), the detailed work on determine the liquidus temperatures and the associated nucleation undercoolings for alloy BM and alloy GM (chemical composition shown in Table 5-1) during solidification is described in this section. The experimental method will be introduced first. Then results on measured enthalpy change, heat capacity and solidification sequences of the two alloys will be reported.

### **A.1 Experimental Method**

A high temperature Stanton Redcroft 1640 Differential Scanning Calorimeter (DSC) was used to measure enthalpy change and transition temperatures of IN792 samples. The DSC unit was calibrated using pure metals with melting points of Au (1064 °C) and Ni (1453 °C). Test coupons of IN792 alloys were wire-eroded from cast rods, and the size of the coupons was 4 mm in diameter and 3 mm in height with a typical weight of about 300 mg. The samples were subjected to heating / cooling cycles as shown in Figure A.1. The cooling rate chosen ( $5 \text{ Kmin}^{-1} = 0.08 \text{ Ks}^{-1}$ ) was typical of conditions encountered during industrial casting. Heating and cooling curves were recorded over a series of DSC runs for both alloys. The *raw* DSC data was subsequently manipulated using a numerical programme CALCOR (Dong and Hunt, 2001) to calculate the enthalpy change from the DSC measurements. The programme treats the complete process of heat flow within the DSC apparatus. This allows the thermal resistances between different parts of the instrument to be calibrated by fitting experimental results for Au and Ni with transition temperature and latent heat. With the calibrated data for the DSC, the programme is able to de-convolute the measured signals and extract the transition temperature and enthalpy change from measurements. Using this programme

it is possible to separate real kinetic effects occurring in the sample from artefacts resulting from an over simplified analysis of a DSC curve. Details of this method of calibration are available elsewhere (Dong and Hunt, 2001; Dong and Brooks, 2005).

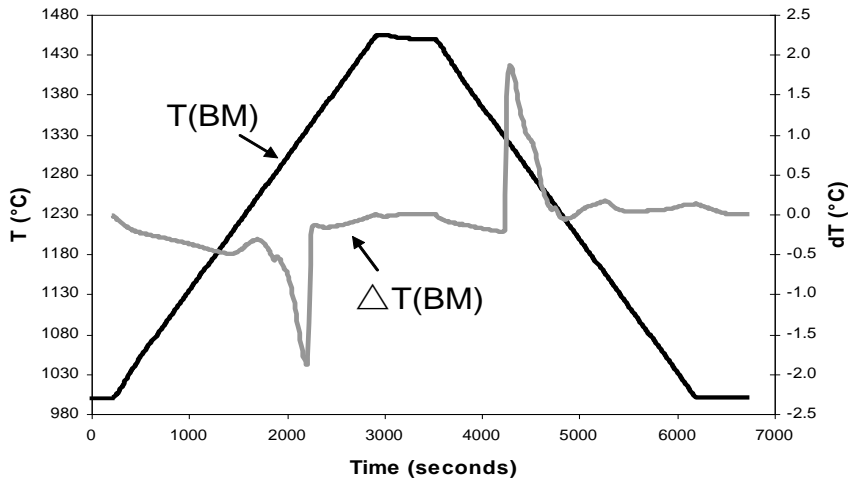
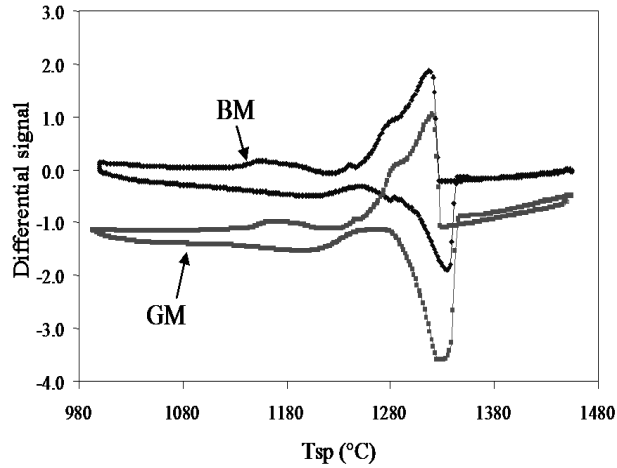


**Figure A.1** An example of heating and cooling cycle used for alloy BM in DSC experiments

## A.2 Results and Analyses

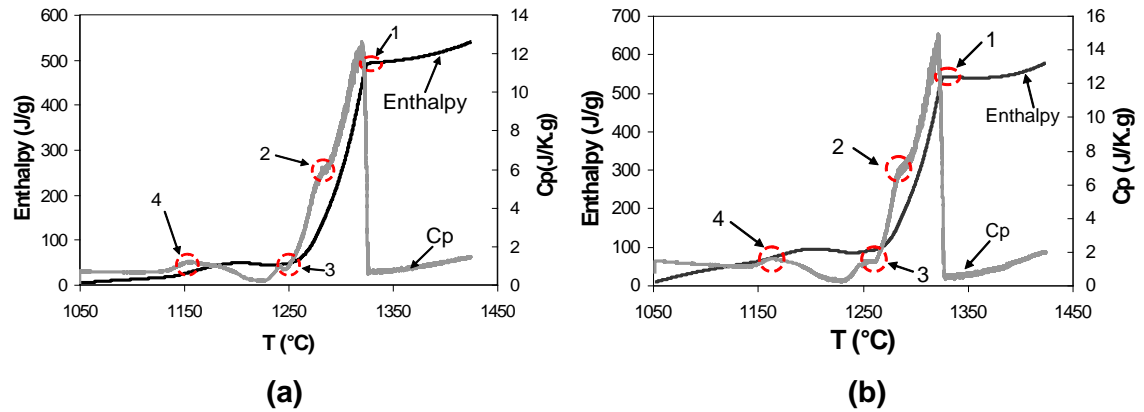
### A.2.1 Enthalpy Change, Heat Capacity and Solidification Sequences

Figure A.2 shows the measured raw DSC curves, i.e. measured differential signal versus the temperature of sample pan ( $T_{SP}$ ) during heating and cooling for alloy BM and alloy GM. The endothermic peak during heating and exothermic peak during cooling correspond to melting and solidification respectively. In conventional DSC analyses, the measured differential signal is assumed to be proportional to the specific heat capacity difference between the sample and reference. Dong *et al.* (2001) and Boettinger *et al.* (1979) pointed out that this is only true when no latent heat evolves in the sample, and during melting and solidification of an alloy the measured signal is smeared over a range of temperatures. Therefore, in this study the measured raw data was de-smeared using the numerical programme CALCOR to obtain the sample enthalpy change ( $H_S$ ) with sample temperature ( $T_S$ ).



**Figure A.2 Measured differential signal versus the temperature of sample pan (TSP) during heating and cooling for alloy BM and alloy GM**

Figure A.3 (a) (b) show the calculated  $H_S$  versus  $T_S$  during the cooling cycle corresponding to alloy BM and alloy GM respectively. The corresponding *effective* heat capacities ( $C_{EP} = \frac{dH}{dT}$ ) are superimposed on the enthalpy plots.



**Figure A.3 Enthalpy change and effectivity heat capacity during the cooling cycle for alloys (a) BM and (b) GM**

The evolution of *weight* fraction solid ( $f_S$ ) or *weight* fraction liquid ( $f_L = 1 - f_S$ ) has been calculated from the measured enthalpy. We express the enthalpy in the form:

$$H = (C_P T + L f_L), \text{ where } C_P \text{ and } L \text{ are the specific heat capacity and latent heat}$$

respectively. Assuming that a constant latent heat and solid and liquid phases having similar specific heat capacities, the fraction liquid can be determined using the following equation:

$$f_L = \left[ \frac{(H - H_{solidus}) - C_p(T - T_{solidus})}{(H_{liquidus} - H_{solidus}) - C_p(T_{liquidus} - T_{solidus})} \right] \quad (A.1)$$

There may be an inaccuracy in the fraction solid calculation. As it has been demonstrated by Dong *et al.* (2003) in Al - 4.45 wt % Cu alloys, micro-segregation should be considered in determining the fraction liquid change. However, in our calculations, as a first approximation we neglect micro-segregation. The reason is the absence of a comprehensive database capable of treating the enthalpy change as a function of temperature and composition for IN792. Calculated fraction liquid evolution during solidification of alloy BM and alloy GM are shown in Figure A.4.

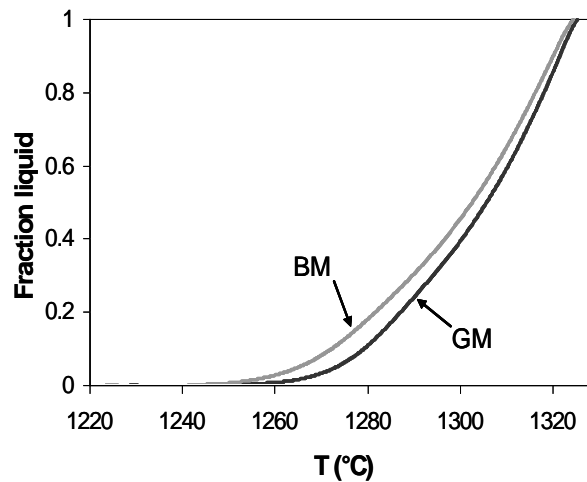


**Figure A.4 Fraction liqQuid change for alloy BM and alloy GM during solidification**

As shown in Figure A.3 and Figure A.4, three major phase transformations as well as the solid precipitation during solidification are revealed for both alloys:

1. The solidification of  $\gamma$  phase (commencing at the liquidus)
2. The formation of carbide at liquid fraction of 0.308 for alloy BM and 0.349 for alloy GM

3. The final formation of  $\gamma/\gamma'$  eutectic at liquid fraction of 0.002 for alloy BM and 0.005 for alloy GM (ending at the solidus)
4. Solid precipitation of  $\gamma'$  phase from  $\gamma$  dendrites

### A.2.2 Liquidus Temperature and Nucleation Undercooling

It is difficult to determine the accurate liquidus temperature from the recorded temperature-time curve (Figure A.1) and the raw DSC signal (Figure A.2). In this study the liquidus temperature is determined by inspecting the intersection of the base line and the extrapolated tangent line of the calculated enthalpy- temperature curve. The tangent approximation method assumes that enthalpy change varies linearly with temperature near the liquidus. This assumption is probably valid due to the less extent of microsegregation at the early stage of solidification (Dong *et al.* 2003). Figure A.5 shows enlarged views of the enthalpy curve near the liquidus temperature and illustrates the tangent method used in this study.

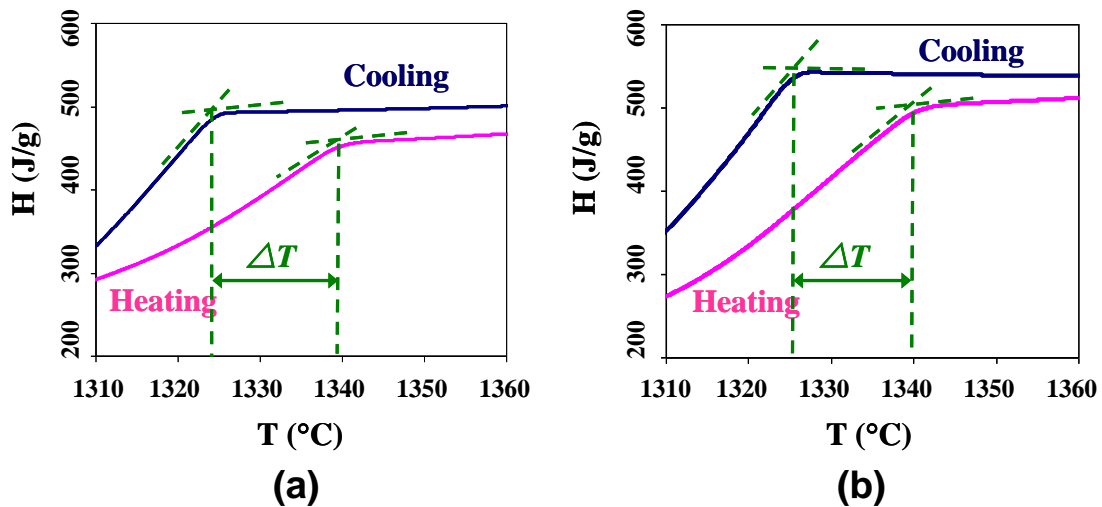


Figure A.5 Enlarged views of enthalpy curve near liquidus temperatures for alloy (a) BM and (b) GM during cooling

The calculated liquidus temperatures and corresponding nucleation undercoolings for alloy BM and alloy GM are listed in Table 5-5 and more discussion about the effect of minor elements on nucleation undercooling can be found in Chapter 5 (Section 5.1.6).

## References

- Al-Jarba, K. A. and Fuchs, G. E. (2004). "Effect of Carbon Additions on the as-Cast Microstructure and Defect Formation of a Single Crystal Ni-Based Superalloy." Materials Science and Engineering A **373**(1-2): 255.
- Badillo, A. and Beckermann, C. (2006). "Phase-Field Simulation of the Columnar-to-Equiaxed Transition in Alloy Solidification." Acta Materialia **54**(8): 2015.
- Bhadeshia, H. K. D. H., Nickel Based Superalloys, <http://www.msm.cam.ac.uk/phase-trans/2003/Superalloys/superalloys.html>, Cambridge, University of Cambridge
- Boettinger, W. J., Coriell, S. R., Greer, A. L., Karma, A., Kurz, W., Rappaz, M. and Trivedi, R. (2000). "Solidification Microstructures: Recent Developments, Future Directions." Acta Materialia **48**(1): 43.
- Boettinger, W. J. and Kattner, U. R. (2002). "On Differential Thermal Analyzer Curves for the Melting and Freezing of Alloys." Metallurgical and Materials Transactions a-Physical Metallurgy and Materials Science **33**(6): 1779.
- Boettinger, W. J., Warren, J. A., Beckermann, C. and Karma, A. (2002). "Phase-Field Simulation of Solidification." Annual review of materials research **32**(1): 163.
- Bradley, E. F., Ed. (1988). Superalloys: A Technical Guide, ASM international.
- Burden, M. H. and Hunt, J. D. (1974). "Cellular and Dendritic Growth .1." Journal of Crystal Growth **22**(2): 99.
- Burden, M. H. and Hunt, J. D. (1974). "Cellular and Dendritic Growth .2." Journal of Crystal Growth **22**(2): 109.
- Campbell, J. (2003). Casting. Oxford, Butterworth-Heinemann.

Caron, P. and Khan, T. (1999). "Evolution of Ni-Based Superalloys for Single Crystal Gas Turbine Blade Applications." Aerospace Science and Technology **3**(8): 513.

Carter, P., Cox, D. C., Gandin, C. A. and Reed, R. C. (2000). "Process Modelling of Grain Selection During the Solidification of Single Crystal Superalloy Castings." Materials Science and Engineering A **280**(2): 233.

Chilton, R. A. (2002). Experimental Study and Modelling of the Cell-Dendrite Transition. Ph. D., Oxford, University of Oxford.

Chojecki, A., Telejko, I., et al. (1997). "Influence of Chemical Composition on the Hot Tearing Formation of Cast Steel." Theoretical and Applied Fracture Mechanics **27**(2): 99.

Coleman, I. (2006). Examination of Texture within Cast and Forged Magnesium Racing Wheels. MEng. Report. Leicester, University of Leicester.

Dai, H. J., Gebelin, J.-C., D'Souza, N., Brown, P. D. and Dong, H. B. (2008). "The Effect of Spiral Shape on Grain Selection During Casting of Single Crystal Turbine Blades." International Journal of Cast Metals Research. (In Print)

Davies, G. J. (1973). Solidification and Casting. New York, Wiley

Dogan, O. N. (1996). "Columnar to Equiaxed Transition in High Cr White Iron Castings." Scripta Materialia **35**(2): 163.

Dong, H. B. (2000). Development of a Novel Scanning Calorimeter and Its Application in Solidification Study. Ph. D., Oxford, University of Oxford.

Dong, H. B. and Brooks, R. (2005). "Determination of Liquidus Temperature in Al-Si and Al-Si-Mg Alloys Using a Single-Pan Scanning Calorimeter." Materials Science and Engineering: A **413-414**: 480.

Dong, H. B. and Hunt, J. D. (2001). "A Numerical Model of a Two-Pan Heat Flux Disc." Journal of Thermal Analysis and Calorimetry **64**(1): 167.

- Dong, H. B. and Lee, P. D. (2005). "Simulation of the Columnar-to-Equiaxed Transition in Directionally Solidified Al-Cu Alloys." Acta Materialia **53**(3): 659.
- Dong, H. B., Shin, M. R. M., Kurum, E. C., Cama, H. and Hunt, J. D. (2003). "Determination of Liquid Fraction During Solidification of Aluminium Alloys Using a Single-Pan Scanning Calorimeter." Fluid Phase Equilibria **212**(1-2): 199.
- Erickson, G.L. (1995). "A new, third-generation single-crystal, casting superalloy." Journal of Materials **47**(4): 36.
- Eskin, D. G., Suyitno and Katgerman, L. (2004). "Mechanical Properties in the Semi-Solid State and Hot Tearing of Aluminium Alloys." Progress in Materials Science **49**(5): 629.
- Flemings, M. C. (1974). Solidification Processing. New York, McGraw-Hill.
- Flood, S. C. and Hunt, J. D. (1987). "Columnar and Equiaxed Growth .1. A Model of a Columnar Front with a Temperature-Dependent Velocity." Journal of Crystal Growth **82**(3): 543.
- Flood, S. C. and Hunt, J. D. (1987). "Columnar and Equiaxed Growth .2. Equiaxed Growth Ahead of a Columnar Front." Journal of Crystal Growth **82**(3): 552.
- Gandin, C. A., Desbiolles, J. L., Rappaz, M. and Thevoz, P. (1999). "A Three-Dimensional Cellular Automaton-Finite Element Model for the Prediction of Solidification Grain Structures." Metallurgical and Materials Transactions A **30**(12): 3153.
- Gandin, C. A. and Rappaz, M. (1994). "A Coupled Finite-Element Cellular-Automaton Model for the Prediction of Dendritic Grain Structures in Solidification Processes." Acta Metallurgica Et Materialia **42**(7): 2233.
- Gandin, C. A. and Rappaz, M. (1997). "A 3d Cellular Automaton Algorithm for the Prediction of Dendritic Grain Growth." Acta Materialia **45**(5): 2187.

## *References*

---

- Gandin, C. A., Rappaz, M. and Tintillier, R. (1994). "3-Dimensional Simulation of the Grain Formation in Investment Castings." Metallurgical and Materials Transactions A **25**(3): 629.
- Gaumann, M., Trivedi, R. and Kurz, W. (1997). "Nucleation Ahead of the Advancing Interface in Directional Solidification." Materials Science and Engineering A **226-228**: 763.
- Goulette, M. J., Spilling, P. D. and Arthey, R. P. (1984). Cost Effective Single Crystals. Superalloys, Warrendale, PA, AIME.
- Greer, A. L., Bunn, A. M., Tronche, A., Evans, P. V. and Bristow, D. J. (2000). "Modelling of Inoculation of Metallic Melts: Application to Grain Refinement of Aluminium by Al-Ti-B." Acta Materialia **48**(11): 2823.
- Hillier, G. S., Rae, C. M. F., Bhadeshia, H. K. D. H. (1988). "Extrinsic and Intrinsic Nodes in the Gamma Prime Phase of a Single-Crystal Superalloy" Acta Materialia, **36**: 95.
- Hobbs, R. A., Karunaratne, M. S. A., Tin, S., Reed, R. C. and Rae, C. M. F. (2007). "Uphill Diffusion in Ternary Ni-Re-Ru Alloys at 1000 and 1100 Degrees C." Materials Science and Engineering A **460**: 587.
- Hua, F. and Grugel, R. N. (1996). "Direct Observation of the Columnar to Equiaxed Zone Transition in an Undercooled Melt." Scripta Materialia **34**(4): 573.
- Huang, W., X., G. and Zhou, Y. (1993). "Primary Spacing Selection of Constrained Dendritic Growth." Crystal growth & design **134**: 105.
- Hunt, J. D. (1984). "Steady State Columnar and Equiaxed Growth of Dendrites and Eutectic." Materials Science and Engineering **65**(1): 75.

## *References*

---

- Hunt, J. D. and Lu, S. Z. (1996). "Numerical Modeling of Cellular Dendritic Array Growth: Spacing and Structure Predictions." Metallurgical and Materials Transactions a-Physical Metallurgy and Materials Science **27**(3): 611.
- Ice, G. E., Pang, J. W. L., Barabash, R. I. and Puzyrev, Y. (2006). "Characterization of Three-Dimensional Crystallographic Distributions Using Polychromatic X-Ray Microdiffraction." Scripta Materialia **55**(1): 57.
- Ihm, B.-C. and Park, D.-J. (1999). "Blind Separation of Sources Using Higher-Order Cumulants." Signal Processing **73**(3): 267.
- Isheim, D., Kolli, R. P., Fine, M. E. and Seidman, D. N. (2006). "An Atom-Probe Tomographic Study of the Temporal Evolution of the Nanostructure of Fe-Cu Based High-Strength Low-Carbon Steels." Scripta Materialia **55**(1): 35.
- Jackson, M. P., Starink, M. J. and Reed, R. C. (1999). "Determination of the Precipitation Kinetics of Ni<sub>3</sub>Al in the Ni-Al System Using Differential Scanning Calorimetry." Materials Science and Engineering A **264**(1-2): 26.
- Jennings, P. A. (1996). Foundries Satellite Vericast. Phase I Simple Blade Casting Trials and Thermal History Generation-Final Report, Rolls-Royce Plc.
- Karma, A. and Rappel, W. J. (1996). "Numerical Simulation of Three-Dimensional Dendritic Growth." Physical Review Letters **77**(19): 4050.
- Kearsey, R. M., Beddoes, J. C., Jones, P. and Au, P. (2004). "Compositional Design Considerations for Microsegregation in Single Crystal Superalloy Systems." Intermetallics **12**(7-9): 903.
- Krishna, R. (2008), Microstructural Investigation of Alloys Used for Power Generation Industries. APG Report. Leicester, University of Leicester.
- Kurum, E. C., Dong, H. B. and Hunt, J. D. (2005). "Microsegregation in Al-Cu Alloys." Metallurgical and Materials Transactions A **36A**(11): 3103.

- Kurz, W., Bezencon, C. and Gaumann, M. (2001). "Columnar to Equiaxed Transition in Solidification Processing." Science and Technology of Advanced Materials **2**(1): 185.
- Kurz, W. and Fisher, D. J. (1981). "Dendrite Growth at the Limit of Stability - Tip Radius and Spacing." Acta Metallurgica **29**(1): 11.
- Kurz, W. and Fisher, D. J. (1984). Fundamentals of Solidification. Rockport, Switzerland, Trans Tech Publications.
- Kurz, W., Giovanola, B. and Trivedi, R. (1986). "Theory of Microstructural Development During Rapid Solidification." Acta Metallurgica **34**(5): 823.
- Langer, J. S. and Mullerkrumbhaar, H. (1978). "Theory of Dendritic Growth .1. Elements of a Stability Analysis." Acta Metallurgica **26**(11): 1681.
- Langer, J. S. and Mullerkrumbhaar, H. (1978). "Theory of Dendritic Growth .2. Instabilities in Limit of Vanishing Surface-Tension." Acta Metallurgica **26**(11): 1689.
- Lee, P. D. (1994). The Formation of Hydrogen Porosity During the Solidification of Aluminium Alloys. Ph.D., Oxford, University of Oxford.
- Lu, S. Z. and Hunt, J. D. (1992). "A Numerical-Analysis of Dendritic and Cellular Array Growth - the Spacing Adjustment Mechanisms." Journal of Crystal Growth **123**(1-2): 17.
- Lu, S. Z., Hunt, J. D., Gilgien, P. and Kurz, W. (1994). "Cellular and Dendritic Growth in Rapidly Solidified Al-Fe and Al-Cu Alloys." Acta Metallurgica Et Materialia **42**(5): 1653.
- Makkonen, L. (2000). "Spacing in Solidification of Dendritic Arrays." Journal of Crystal Growth **208**(1-4): 772.
- McLean, M. (1983). Directionally Solidified Materials for High Temperature Service. London, The Metals Society.

- Meetham, G. W. (1981). The Development of Gas Turbine Materials. Barking, Applied Science.
- Mingard, K. P., Roebuck, B., Bennett, E. G., Gee, M. G., Nordenstrom, H., Sweetman, G. and Chan, P. (2009). "Comparison of Ebsd and Conventional Methods of Grain Size Measurement of Hardmetals." International Journal of Refractory Metals and Hard Materials **27**(2): 213.
- Nakagawa, Y. (2004). Aero-Engine Business and Material Technologies in Japan. Superalloys, Champion, PA, TMS.
- Napolitano, R. E. and Schaefer, R. J. (2000). "The Convergence-Fault Mechanism for Low-Angle Boundary Formation in Single-Crystal Castings." Journal of Materials Science **35**(7): 1641.
- Poirier, D. R. and Speiser, R. (1987). "Surface-Tension of Aluminum-Rich Al-Cu Liquid Alloys." Metallurgical Transactions a-Physical Metallurgy and Materials Science **18**(6): 1156.
- Pollock, T. M., Murphy, W. H., Goldman, E. H., Uram, D. L. and Tu, J. S. (1992). Grain Defect Formation During Directional Solidification of Nickel Base Single Crystals. Superalloys Champion, PA, TMS.
- Pollock, T. M. and Tin, S. (2006). "Nickel-Based Superalloys for Advanced Turbine Engines: Chemistry, Microstructure, and Properties." Journal of Propulsion and Power **22**(2): 361.
- Quested, T. E. and Greer, A. L. (2005). "Grain Refinement of Al Alloys: Mechanisms Determining as-Cast Grain Size in Directional Solidification." Acta Materialia **53**(17): 4643.
- Rae, C. M. F. and Reed, R. C. (2001). "The Precipitation of Topologically Close-Packed Phases in Rhenium-Containing Superalloys." Acta Materialia **49**(19): 4113.

- Rafii-Tabar, H. and Chirazi, A. (2002). "Multi-Scale Computational Modelling of Solidification Phenomena." Physics Reports **365**(3): 145.
- Ramirez, J. C. and Beckermann, C. (2005). "Examination of Binary Alloy Free Dendritic Growth Theories with a Phase-Field Model." Acta Materialia **53**(6): 1721.
- Rappaz, M., Bellet, M. and Deville, M. (2003). Numerical Modelling in Materials Science and Engineering. Berlin, Springer Verlag.
- Rappaz, M. and Gandin, C. A. (1993). "Probabilistic Modeling of Microstructure Formation in Solidification Processes." Acta Metallurgica Et Materialia **41**(2): 345.
- Rappaz, M. and Gandin, C. A. (1994). "Stochastic Modeling of Grain-Structure Formation in Solidification Processes." Mrs Bulletin **19**(1): 20.
- Rappaz, M., Gandin, C. A., Desbiolles, J. L. and Thevoz, P. (1996). "Prediction of Grain Structures in Various Solidification Processes." Metallurgical and Materials Transactions A **27**(3): 695.
- Reed, R. C. (2006). The Superalloys : Fundamentals and Applications, Cambridge University Press.
- Reed, R. C., Cox, D. C. and Rae, C. M. F. (2007). "Kinetics of Rafting in a Single Crystal Superalloy: Effects of Residual Microsegregation." Materials Science and Technology **23**(8): 893.
- Reed, R. C., Yeh, A. C., Tin, S., Babu, S. S. and Miller, M. K. (2004). "Identification of the Partitioning Characteristics of Ruthenium in Single Crystal Superalloys Using Atom Probe Tomography." Scripta Materialia **51**(4): 327.
- Siqueira, C. A., Cheung, N. and Garcia, A. (2002). "Solidification Thermal Parameters Affecting the Columnar-to-Equiaxed Transition." Metallurgical and Materials Transactions A **33**(7): 2107.

## *References*

---

- Stanford, N., Djakovic, A., Shollock, B. A., McLean, M., D'Souza, N. and Jennings, P. A. (2004). "Seeding of Single Crystal Superalloys--Role of Seed Melt-Back on Casting Defects." Scripta Materialia **50**(1): 159.
- Thevoz, P., Desbiolles, J. L. and Rappaz, M. (1989). "Modeling of Equiaxed Microstructure Formation in Casting." Metallurgical Transactions A **20**(2): 311.
- Tin, S. and Pollock, T. M. (2004). "Predicting Freckle Formation in Single Crystal Ni-Base Superalloys." Journal of Materials science **39**(24): 7199.
- Trivedi, R., Liu, S., Mazumder, P. and Simsek, E. (2001). "Microstructure Development in the Directionally Solidified Al-4.0 Wt% Cu Alloy System." Science and Technology of Advanced Materials **2**(1): 309.
- Vandyoussefi, M. and Greer, A. L. (2002). "Application of Cellular Automaton-Finite Element Model to the Grain Refinement of Directionally Solidified Al-4.15 Wt% Mg Alloys." Acta Materialia **50**(7): 1693.
- Walston, W. S., O'Hara, K. S., Ross, E. W., Pollock, T. M. and Murphy, W. H. (1996). Rene N6: Third Generation Single Crystal Superalloy. Superalloys, Champion, PA, TMS.
- Wang, C. Y. and Beckermann, C. (1994). "Prediction of Columnar to Equiaxed Transition During Diffusion-Controlled Dendritic Alloy Solidification." Metallurgical and Materials Transactions a-Physical Metallurgy and Materials Science **25**(5): 1081.
- Wang, W. (2003). A Mathematical Model of Dendritic Microstructures in Nickel-Based Superalloys. Ph. D., London, Imperial College London.
- Wang, W., Lee, P. D. and McLean, M. (2003). "A Model of Solidification Microstructures in Nickel-Based Superalloys: Predicting Primary Dendrite Spacing Selection." Acta Materialia **51**(10): 2971.

- Warren, J. A. and Boettinger, W. J. (1995). "Prediction of Dendritic Growth and Microsegregation Patterns in a Binary Alloy Using the Phase-Field Method." Acta Metallurgica Et Materialia **43**(2): 689.
- Warren, J. A. and Langer, J. S. (1990). "Stability of Dendritic Arrays." Physical Review A **42**(6): 3518.
- Wong, M. H. "MSE 407 Case study – Single Crystalline Turbine Blades (Deborah Schorr)", Nov 12th 2003
- Yan, X. Y., Xie, F. Y., Chu, M. and Chang, Y. A. (2001). "Microsegregation in Al-4.5Cu Wt.% Alloy: Experimental Investigation and Numerical Modeling." Materials Science and Engineering A **302**(2): 268.
- Yang, X. L. (2005). Simulation of Stray Grain Formation in Single Crystal Ni-Based Superalloy Turbine Blades. Ph. D., London, Imperial College London.
- Yang, X. L., Dong, H. B., Wang, W. and Lee, P. D. (2004). "Microscale Simulation of Stray Grain Formation in Investment Cast Turbine Blades." Materials Science and Engineering A **386**(1-2): 129.
- Yardley, V. A., Sugiura, R., Matsuzaki, T., Tsurekawa, S., Yokobori, J. A. T. and Hasegawa, Y. (2007). "Quantitative Study of W-Alloyed 9-12 Cr Steel Microstructures Using Ebsd." Strength, Fracture and Complexity **5**(1): 39.
- Yeh, A. C. and Tin, S. (2006). "Effects of Ru on the High-Temperature Phase Stability of Ni-Base Single-Crystal Superalloys." Metallurgical and Materials Transactions a-Physical Metallurgy and Materials Science **37A**(9): 2621.
- Yi, G. Y. (2008). Simulation of Microstructure Evolution during Solidification. 2<sup>nd</sup> Year Report. Leicester, University of Leicester.
- Zhang, J. (2003). "Effect of Ti and Ta on Hot Cracking Susceptibility of Directionally Solidified Ni-Based Superalloy In792." Scripta Materialia **48**(6): 677.

Zhang, J. and Singer, R. F. (2002). "Hot Tearing of Nickel-Based Superalloys During Directional Solidification." Acta Materialia **50**(7): 1869.

Zhang, J. and Singer, R. F. (2004). "Effect of Grain-Boundary Characteristics on Castability of Nickel-Base Superalloys." Metallurgical and Materials Transactions a-Physical Metallurgy and Materials Science **35A**(3): 939.

Zhang, J. X., Murakumo, T., Koizumi, Y., Kobayashi, T., Harada, H. and Masaki, S. (2002). "Interfacial Dislocation Networks Strengthening a Fourth-Generation Single-Crystal Tms-138 Superalloy." Metallurgical and Materials Transactions A **33**(12): 3741.

Zhou, Y. Z., Volek, A. and Green, N. R. (2008). "Mechanism of Competitive Grain Growth in Directional Solidification of a Nickel-Base Superalloy." Acta Materialia **56**(11): 2631.

Zhou, Y. Z., Volek, A. and Singer, R. F. (2005). "Influence of Solidification Conditions on the Castability of Nickel-Base Superalloy In792." Metallurgical and Materials Transactions A **36A**(3): 651.